Study of the Venus surface and lower atmosphere using VMC images

Von der Fakultät für Elektrotechnik, Informationstechnik, Physik
der Technischen Universität Carolo-Wilhelmina
zu Braunschweig
zur Erlangung des Grades eines
Doktors der Naturwissenschaften
(Dr.rer.nat.)
genehmigte
Dissertation

von Eugene Shalygin
aus Kharkiv, Ukraine

Bibliografische Information der Deutschen Nationalbibliothek

Die Deutsche Nationalbibliothek verzeichnet diese Publikation in der Deutschen Nationalbibliografie; detaillierte bibliografische Daten sind im Internet über `http://dnb.d-nb.de` abrufbar.

1. Referent: Prof. Dr. Jürgen Blum
2. Referent: Prof. Dr. Andreas Hördt
eingereicht am: 19. Februar 2013
mündliche Prüfung (Disputation) am: 23. April 2013

ISBN 978-3-942171-71-7

uni-edition GmbH 2013
http://www.uni-edition.de

Cover images:
Background — Fotla corona (Magellan radar, credit: NASA)
Venus globe consists of VMC UV image (upper), and global topography map (Magellan radar, credit: NASA)

Printed in Germany

Vorveröffentlichungen der Dissertation

Teilergebnisse aus dieser Arbeit wurden mit Genehmigung der Fakultät für Elektrotechnik, Informationstechnik, Physik, vertreten durch den Mentor, in folgenden Beiträgen vorab veröffentlicht:

Publikationen

Basilevsky, A. T., E. V. Shalygin, D. V. Titov, W. J. Markiewicz, F. Scholten, T. Roatsch, M. A. Kreslavsky, et al. (2012). "Geologic interpretation of the near-infrared images of the surface taken by the Venus Monitoring Camera, Venus Express". In: *Icarus* 217.2, pp. 434–450. DOI: 10.1016/j.icarus.2011.11.003.

Shalygin, E. V., A. T. Basilevsky, W. J. Markiewicz, D. V. Titov, M. A. Kreslavsky, and T. Roatsch (2012). "Search for ongoing volcanic activity on Venus: Case study of Maat Mons, Sapas Mons and Ozza Mons volcanoes". In: *Planetary and Space Science* 73.1, pp. 294–301. DOI: 10.1016/j.pss.2012.08.018.

Tagungsbeiträge

Basilevsky, A. T., E. V. Shalygin, W. J. Markiewicz, D. V. Titov, T. Roatsch, and M. A. Kreslavsky (2012). "Search for ongoing volcanic activity on Venus: Case study of Maat Mons, Sapas Mons and Ozza Mons". In: *EGU General Assembly Conference*. (Vienna, Austria, May 2–7, 2012). Vol. 14. #6328.

Basilevsky, A. T., E. V. Shalygin, D. V. Titov, W. J. Markiewicz, F. Schollten, et al. (2012). "Possible Felsic Summit of Tuulikki Mons, Venus: Evidence from 1-Micron Surface Emissivity and Magellan-Viewed Morphology". In: *Lunar and Planetary Science Conference*. (The Woodlands, USA, Mar. 19–23, 2012). Vol. 43. #1092.

Shalygin, E. V., A. T. Basilevsky, W. J. Markiewicz, D. V. Titov, F. Scholten, et al. (2012). "Analysis of the images of the Venus surface taken by the Venus Monitoring Camera, Venus Express". In: *The Third Moscow Solar System Symposium*. (Moscow, Russia, Oct. 8–12, 2012). #VN-14.

Shalygin, E. V., A. T. Basilevsky, D. V. Titov, W. J. Markiewicz, et al. (2012). "Geologic interpretation of the near-infrared images of area SW of Beta Regio taken by the Venus Monitoring Camera". In: *EGU General Assembly Conference*. (Vienna, Austria, May 2–7, 2012). Vol. 14. #6314.

Basilevsky, A. T., E. V. Shalygin, D. V. Titov, W. J. Markiewicz, et al. (2011). "Analysis of the Venus Surface Thermal Emission Images Taken by the VMC Camera, Venus Express". In: *Lunar and Planetary Science Conference*. (The Woodlands, USA, Mar. 7–11, 2011). Vol. 42. #1280.

Shalygin, E. V., A. T. Basilevsky, D. V. Titov, and W. J. Markiewicz (2011). "Synthetic images of Venus surface based on VMC images". In: *EGU General Assembly Conference*. (Vienna, Austria, May 2–7, 2011). Vol. 13. #554.

Basilevsky, A. T., E. V. Shalygin, D. V. Titov, W. J. Markiewicz, et al. (2010). “Geologic Analysis of the Surface Thermal Emission Images Taken by the VMC Camera, Venus Express”. In: *Lunar and Planetary Science Conference*. (The Woodlands, USA, Mar. 1–5, 2010). Vol. 41. #1133.

Shalygin, E. V., D. V. Titov, A. T. Basilevsky, and W. J. Markiewicz (2010). “Venus surface from the VMC night side imaging ”. In: *International Venus Conference*. (Aussois, France, June 20–26, 2010).

Shalygin, E. V., D. V. Titov, A. T. Basilevsky, and VMC team (2010). “Synthetic images of Venus surface based on VMC images”. In: *European Planetary Science Congress*. (Potsdam, Germany, Sept. 13–18, 2009). Vol. 4. #622.

Basilevsky, A. T., E. V. Shalygin, D. V. Titov, W. J. Markiewicz, F. Scholten, and M. A. Kreslavsky (2008). “Geologic analysis of the surface thermal emission images taken by the Venus Monitoring Camera, Venus Express: The approach and initial results”. In: *Lunar and Planetary Science Conference*. (Legue City, USA, Mar. 10–14, 2008). Vol. 39. #1526.

Roatsch, T., A. T. Basilevsky, E. V. Shalygin, D. Titov, et al. (2008). “Geologic interpretation of the NIR images taken by the Venus Monitoring Camera”. In: *COSPAR Scientific Assembly*. (Montreal, Canada, July 13–20, 2008). Vol. 37. #2623.

Contents

Preface

Venus has long and successful history of exploration. It has been studied via ground-based observations and by spacecraft. More than 20 missions, including fly-byes, orbiters, descent probes, atmospheric balloons, and landers have studied Venus. Yet many questions about Venus surface and geology remain open. This thesis contributes to the following: we search for differences in mineralogical composition of the surface, and search for ongoing volcanic activity.

Obviously, remote sensing is the only possibility to study Venus surface globally in foreseeable future. Remote sensing of the Venus surface is complicated task due to Venus thick atmosphere and clouds. Together they block radiation from surface almost in whole electromagnetic spectrum except radio- and microwaves (where the atmosphere is completely transparent), and a few narrow transparency "windows" in near infra-red. These transparency "windows" give a unique opportunity to sense Venus' surface: the surface is hot enough (≈ 470 °C) to produce significant thermal flux in near infra-red, and this flux can escape to the space and then can be detected at the night side of the planet. Two instruments on-board Venus Express are able to perform sounding in the near infra-red transparency "windows": Visible and Infrared Thermal Imaging Spectrometer and Venus Monitoring Camera. Together they provided the first systematic thermal mapping of the Venus surface from orbit.

Near infra-red emissivity (or reflectivity) is sensitive (as opposed to microwave one) to mineralogical composition of the surface layer. At the temperature of the surface, near infra-red is located at the short-wavelength shoulder of the Planck curve, while microwaves are on the long-wavelength one. Hence near infra-red flux is much more sensitive to the temperature of the surface, that gives possibility to detect a hot lava on the surface.

We used images, obtained by the Venus Monitoring Camera (on-board Venus Express) in 1-μm transparency "window", to retrieve emissivity of the surface. Atmosphere in this "window" is not completely transparent, in particular, there is gaseous absorption and scattering in clouds. Therefore for analysis we need radiative transfer modelling, results of which we compare with the observational data.

In the thesis we have obtained probabilities of difference in mineralogical compositions of several surface units, and determined gaseous absorption value in very low atmosphere.

Since Venus Monitoring Camera has observed significant part of the Northern hemisphere of Venus, we used these data to search for hot spots at the surface, which might mean presence of a hot (fresh) lava and ongoing volcanic activity. Therefore we have estimated the possibility of detecting the lava fields of various sizes and shapes by Venus Monitoring Camera observations.

Eugene Shalygin
Katlenburg-Lindau, February 2013

Glossary

Terms

blink comparator	A method, which was used by astronomers for finding differences between two similar images by rapidly switching them in the view. During this process any differences between images were clearly visible to the observer. The method can be also applied to co-align two similar images, by shifting one of them until visible difference becomes minimal. Used to be implemented as a special device, but in the modern time, when images are stored in computers, was replaced by a special software. 61, 111
point spread function	Response of an imaging system to a point source. In application to an atmosphere (as the imaging system) — image of a point source as visible through the atmosphere. 45, 49, 50, 67, 68
transparency “window”	A region of (electromagnetic) spectra, where absorption in the atmosphere is significantly weaker than in surroundings. 7, 15, 18, 20, 22, 25, 30, 34, 41, 48, 79, 93, 94

Acronyms

CDSD	carbon dioxide spectroscopic database.
HITRAN	high-resolution transmission molecular absorption database.
MGN	Magellan Venus Radar Mapping Mission.
NIR	near infra-red.
RT	radiative transfer.
SAR	synthetic aperture radar.
SNR	signal-to-noise ratio.

UV	ultra-violet.
VEX	Venus Express.
VIRA	Venus International Reference Atmosphere.
VIRTIS	Visible and Infra-red Thermal Imaging Spectrometer.
VMC	Venus Monitoring Camera.

1 Introduction

1.1 Planet Venus

The very bright "morning" and "evening" stars were known since prehistoric times. Much later it became clear that these two objects are in fact morning and evening appearances of the same planet, which has been named after goddess of love in the ancient time. The only planet named after a female may have been named for the most beautiful deity of her pantheon because it is the brightest of the five planets known to ancient astronomers (apparent magnitude of Venus reaches -4.6^m). It can be visible by naked eye during a day and even can cast a shadow. This is the third brightest celestial object (regular) after the Sun and the Moon. Venus is an interior planet and thus its maximum elongation from the Sun for the Earth's observer is 47.8°.

Being such a bright and easy to see, Venus was playing notable role in culture. Venus was a goddess of Love and Beauty for Babylonians, Greeks and Romans, goddess of fertility, healing and wisdom for Old Persians, and was significant in many others cultures. Religious calendar developed by Maya culture (called *Noh Ek'*, and which was used by other Mesoamerican cultures) was based on 584-day cycles, that is approximately equal to synodic period of Venus. This planet has attracted and attracts the attention of people, but not only by its beauty. Under the cloak of shimmering beauty Venus hides interesting puzzles that scientists want to solve.

1.2 Highlights of Venus observations and exploration

Discoveries in celestial mechanics and determination of gravity constant made possible to determine the mass of Venus, that is close to the Earth one (0.815 of Earth's). Invention of a telescope made possible to resolve planet's disk and to determine its size. The bulk density of Venus proved that the planet has a solid core and a surface. Further observations discovered the presence of an atmosphere around Venus (by Michail Lomonosov during the Venus transit in 1761). This atmosphere appeared to be so optically thick that one can not see the surface through it. In visible light Venusian disk appears featureless due to the clouds, which cover the entire planet. Thus, investigation of the Venus surface were started only after inventing the radar techniques in 20th century.

1.2.1 Ground-based studies

With invention of spectroscopy it became possible to determine the principal chemical composition of the atmosphere (first detection of CO_2 by Adams and Dunham Jr (1932)): it appeared to be composed from CO_2 and N_2. However, until Venera-4 descent probe made direct measurements in the atmosphere, the amount of CO_2 was significantly underestimated. The pressure in the atmosphere on the cloud level can be determined from spectroscopic observations as well. Determined values were 0.1 – 0.2 bar. However, there was an ambiguity: it was reported about pressure of several bars also (Kuz'min and Marov, 1974).

Measuring integral spherical albedo of Venus and its absolute brightness, one can derive the effective temperature. According to albedo measurements by Irvine (1968), $A = 0.77 \pm 0.07$ that gives $T_e = 228\,\mathrm{K}$. Colour temperatures for 3 – 14 μm gave almost the same values (Kuz'min and Marov, 1974).

From ground-based spectrometric and polarimetric observations it was detected that upper clouds consist of ∼ 1 μm droplets of 75 % sulfuric acid (Hansen and Hovenier, 1974; Kawabata and Hansen, 1975). Before polarimetric data were involved in the analysis, the remote sensing of Venusian clouds was not able to constrain the properties of the scatterers with precision, that is needed to determine the clouds composition. Analysis of photometric data gave constrains for refractive index from 1.3 to 1.7 (water to metal) and sizes of particles from 1 μm and large. On the other hand, polarization is very sensitive to variations of refractive index and particle's size.

Studies of the surface began from determination of the bulk density of Venus. The value of 5.243 g/cm^3 suggests that the planet has solid core and, thus, a surface. The next step was done with radio observations of Venus, performed in the middle of the 20th century. In 1956 Mayer et al. performed observations on 3.15 cm wavelength (Mayer et al., 1958). These observations showed the temperature of the Venus to be about 600 K. Later observations (Kuz'min and Salomonovich, 1961) showed that in centimeter-band wavelengths the temperature is 600 K and 300 K in the millimeters band. Two possible explanations of that difference were proposed: 1) hot surface, and cold atmosphere which absorbs at some wavelength, and 2) cold surface, and hot atmosphere that emits at some wavelengths. To produce such absorption a very dense atmosphere (with pressure near surface ∼ 20 – 100 bar) is needed, but that seemed to be unlikely at that time. However, observations of star osculations showed that the atmosphere pressure indeed is very high (*e.g.* Sagan, 1962–1963), and observations at 3.02 cm with high resolution showed that the emission from the edge of a planet is partially polarized (Clark and Kuz'min, 1965), that is not possible if radiation comes from an atmosphere. The same observations also gave an estimation of the radius of the solid body: (6057±55) km. Later, after Venera-4 flight, Kuz'min recalculated the estimations of the temperature basing on the knowledge of the atmospheric composition. Corrected value of the surface temperature is (700±100) K appeared to be very close to the result of the later direct measurement by landers: 735 K. These findings drastically changed our ideas about Venus from Earth twin planet into the hell-like word with extremely hot surface, heated by greenhouse effect, which is so strong at Venus because of the very dense atmosphere (65 kg/m^3 near the surface) consisting almost completely from CO_2.

In the same time there were first attempts to perform active radar sounding. The first observations have been performed during an inferior conjunction of Venus in 1961. Several teams have performed observations in UK, the USA, and the USSR (*e.g.* Kotel'nikov et al., 1966; Goldstein et al., 1965). Such observations can give: i) a rotation period of the planet from Doppler widening of the original frequency, and ii) a map of albedo in "Doppler shift"-"echo delay" frame. Rotation period of 200 – 400 days was detected in 1961, then it was corrected to be (250±40) days after observations in 1962, and to (230±25) days (observations at Evpatoria), (249±6) days (Goldstone), and (247±5) days (Arecibo) in 1964. The maps of albedo, obtained from these observations, showed the first features on the Venus surface: Alpha Regio and Beta

Regio (for example, fig. 1.1). Later, the big circular features were identified as volcanic coronas, the objects specific to Venus (section 1.4). Unfortunately, during inferior conjunctions we see almost the same part of the Venus, thus, complete mapping of the Venus surface is possible only from a spacecraft orbiting around Venus.

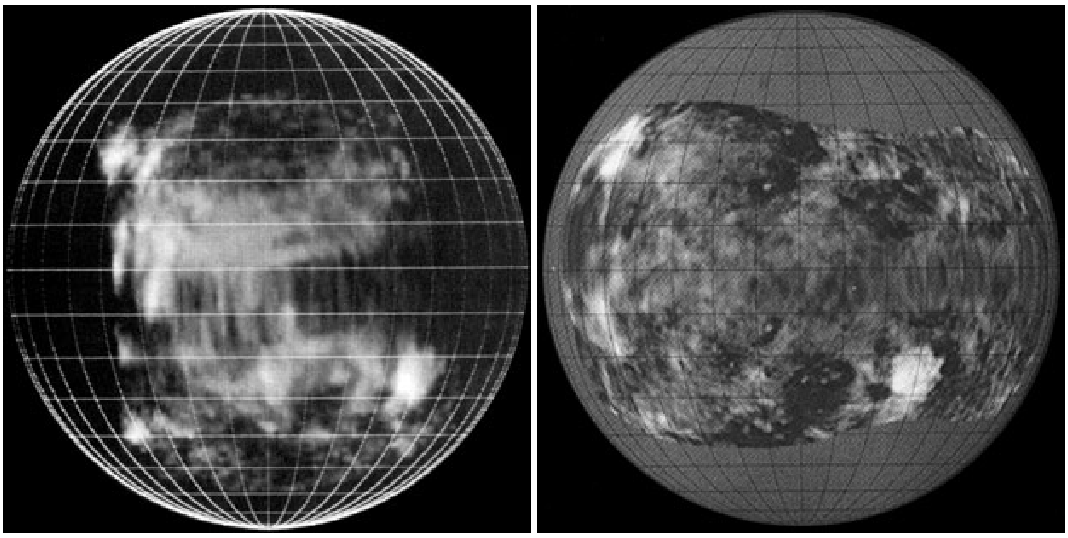

(a) Hayford Antenna (MIT), 1967.

(b) Goldstone Antennas (JPL), 1972.

Figure 1.1: Maps of radar albedo.

Discovery of the near infra-red (NIR) transparency "windows" (Allen and Crawford, 1984) gave a new way to sound the atmosphere below the clouds and even the surface. In these "windows" absorption of the emission of hot lower layers of the atmosphere is weak. Different "windows" are most sensitive to different altitudes. In "window" around 1 μm radiation originates from the hot surface and this "windows" can be used for mapping of the surface temperature and emissivity. In such way images of the surface could be obtained from the ground (Meadows and Crisp, 1996) and from spacecraft.

1.2.2 Exploration by spacecraft

With the start of exploration of Venus by orbiters and descent probes, our knowledge about the planet expanded drastically. Up to now, more than 20 successful missions were performed, either dedicated to Venus studies completely, or having Venus as an additional target. It was started with Mariner-2 fly-by (the first one from the NASA' Mariner series, launched to Venus) in 1962, followed by very successful series of Venera spacecraft (USSR), Pioneer-Venus missions (NASA/USA), Magellan mission (NASA/USA) and others. Venus was studied from orbiters, by descent probes and landers. The recent one, the Venus Express (VEX) spacecraft of the European Space Agency, launched in 2005, is still working on the polar orbit around the planet.

The Mariner-2 fly-by gave suggestions about slow Venus rotation, showed limb-darkening in microwave and infra-red bands (that could be indication of a hot surface and thick clouds). Mariner-2 discovered that magnetic field around Venus is at least 10 times weaker than the Earth's one.

On October 18, 1967, Venera-4 entered Venus atmosphere. During its descent from altitude 52 km to 26 km the probe performed first *in situ* measurements of the atmosphere composition: 90 – 93 % CO_2, 7 % N_2, 0.4 – 0.8 % O_2, and 0.1 – 1.6 % water vapour.

The next mission, Mariner-5, flew by Venus a day later, on October 19, 1967. Radio occultation experiment, performed by the spacecraft, gave new results about density and temperature of the atmosphere. In particular, the atmosphere turned out to be much denser and the surface — hotter.

Using this information, the next missions, Venera-5 and Venera-6, were ready for the dense atmosphere. Both probes had new chemical compositions analysers, tuned basing on Venera-4 results. The Venera-5 was launched on January 5, 1969, and Venera-6 — on January 10. They arrived at Venus on May 16 and 17 respectively. Both probes survived for a little over 50 minutes, reaching levels where the temperature was about 600 K and pressure about 27 bar, where they were destroyed by the pressure. The atmosphere composition, deduced from Venera-4 to Venera-6 was: CO_2 — (97±4) %, N_2 — less than 2 %, O_2 — less than 0.1 %, H_2O — 6 to 11 mg/L.

The next goal was to perform a landing and transmit information from the surface. The goal was reached by Venera-7, launched on August 17, 1970 and entered the atmosphere of Venus on December 15, 1970. The descent capsule was designed to survive under much higher pressure (150 bar and temperature 540 °C), than it was done for Venera-5 and Venera-6. Unfortunately, landing was not as smooth as expected, and only temperature measurement from the surface has been retrieved: 750 K. It was the first man-made spacecraft, that has landed on another planet and transmitted data from there.

Venera-8 was launched on March 27, 1972 and entered the atmosphere on July 22. After 55 minutes long descent, Venera-8 landed and continued to transmit scientific data for an additional 50 minutes. Beside other instruments, it had a photometer, that measured an illumination at different altitude levels, and on the surface. It was found that there are no clouds below 35 km altitude and that illumination on the surface is suitable for photography.

Mariner-10 was launched to perform fly by Venus and Mercury on November 3, 1973. The spacecraft passed Venus on February 5, 1974, the closest approach being 5768 km. Its images of the Venus clouds in ultra-violet (UV) surprisingly revealed a lot of features. The spacecraft sent back to the Earth the images of the haze above the clouds.

Venera-9, the next mission to Venus (launched on June 8, 1975), included orbiter and lander. It total mass was 4936 kg that became possible with usage of Proton launch vehicle that made possible to transport more then 4000 kg to the Venus. Venera-9 was carrying much more instruments than previous missions. The lander had imaging cameras and it has obtained first ever images from the surface of another planet. Venera-10 followed in the same launch window on June 14, 1975. Both landers performed studies of the clouds during descent.

In December, 1978, two large missions arrived to Venus: on 4th — Pioneer Venus Orbiter (launched on March 20, 1978) and on 9th — Pioneer Venus Multiprobe (launched on August 8, 1978). The Orbiter was mainly targeted at the radar mapping of the surface, and the spacecraft was doing that for more than 10 years. Multiprobe mission was consisting of a bus with 3 small and 1 large probes for analysis of the atmosphere.

The exploration was continued by Venera-11 and Venera-12, launched on Septermber 9 and 14, 1978 and arrived to Venus in the end of December. As a new payload their landers had experiments for soil analysis, colour cameras, and lightning detectors. Evidence for lightnings were detected, but colourful cameras and soil analyser failed to work.

Venera-13 and Venera-14 were launched in 1981 (October 30 and November 4, respectively). They were identical and, in general, improved version of Venera-11. This time both cameras and soil analyser worked well, and we got excellent colour images of the Venus surface and sky.

The next mission to Venus was mainly targeted on studies of its surface. Two identical spacecraft were designed to orbit Venus and map the northern part of the planet using synthetic aperture radar (SAR). These missions were the first to use SAR to map another planet. Venera-15 was launched on June 2, 1983 and arrived on October 10. Venera-16 was launched on June 7 and arrived on October 11. Venera-15 and Venera-16 were inserted in orbit around Venuns and were operational until January 5 and June 13, 1985 respectively. They mapped northern hemisphere (from 30° latitude) with spatial resolution of 1 – 2 km and 30 m by altitude. After this survey new types of surface structures were discovered at the Venus, in particular, coronae and tesserae (see section 1.4).

Two Vega missions were launched (in cooperative effort among USSR and many European countries) to Venus and Halley's Comet on December 15, 1984 and December 20, 1984. Both identical crafts consisted of lander, balloon, and a spacecraft which served as re-translator for the lander and then flew for a rendezvous with the nucleus of the Halley's Comet. During Venus flybys, descent probes were released. Balloons were deployed at altitude 53 – 55 km where each of them have travelled more the 11 000 km in 46 h of operations. Landers were continuation of the design used since Venera-9. Since the landing sites were on the night-side of the planet, cameras were not included. Instead of that, they did a few experiments to investigate the nature of the clouds.

After been delayed and redesigned, on May 4, 1989 the Magellan spacecraft was launched and arrived at Venus 10th of August 1990. This mission was aimed to obtain near-global coverage of Venus surface by topography, radar images (using SAR, altimetry, and radiometry modes), and gravity field measurements. The spacecraft was the first interplanetary one to be using aero-braking to lower apoapsis, that has allowed to decrease the eccentricity of the orbit and perform more precise measurements. From 1990 to 1994, it mapped 98 % of the surface of Venus at resolution 0.1 – 0.25 km (depending on the distance from the planet), and for the altimetery 30 m by altitude and spatial resolution of several km.

After that, a number of spacecraft have been performed Venus fly byes, in particular Galileo (NASA), Cassini–Huygens (NASA/ESA/ASI), MESSENGER (NASA).

On November 9, 2005 the Venus Express spacecraft was launched to the planet. The spacecraft was designed mainly to perform long term observations of the atmosphere and environment. It has arrived to Venus on April, 11 2006 and operating since that time. Venus Express performs longest continuous observations of Venus were ever done. More detailed description of the mission is given in section 2.1, because this work is based on the data obtained by Venus Monitoring Camera which is placed on-board of Venus Express.

Knowledge about Venus evolution accumulated so far suggests that Venus and the Earth were quite similar when they formed, but then the different evolution processes lead to extreme difference between conditions on these sister planets. Why and how drastic differences between the Earth and Venus developed? These questions drive significant part of Venus researches from the time of determination of its basic characteristics until present days.

1.3 Atmosphere of Venus

Venus has the most massive atmosphere from terrestrial planets. If the mass ratio of atmosphere and planet for the Earth is 0.86×10^{-6}, for Venus is in 110 times larger (table 1.1). The troposphere, where the temperature linearly decreases with altitude, has a considerable extent. There is a deep "ocean" of dense and hot gas below the level of normal conditions (with pressure of 1 bar), which extends for more than 50 km and near the surface reaches density, comparable to that of water. Its mass (4.7×10^{20} kg) is only three times less than that of the Earth' oceans. Even without clouds this atmosphere would be opaque because of the strong absorption and scattering almost at all wavelengths, except radio band. The only few exceptions are several transparency "windows" near 1 µm.

Table 1.1: Bulk properties of the atmosphere from Taylor (2006).

Total mass	4.8×10^{20} kg ($0.96\times10^{-4} \times M_{♀}$)
Surface pressure	92 bar
Surface density	65 kg/m^3
Surface temperature	737 K (464 °C)
Scale height[1]	15.9 km

[1] for the lower atmosphere

Main compounds of the atmosphere are CO_2 and N_2, with small additions of other gases (table 1.2). Such huge amount of CO_2 (mainly) results in very strong greenhouse effect. Because of that the surface of Venus, which receives from Sun even less amount of energy, than the Earth (Venus has higher albedo), is heated to such a high temperature (table 1.1).

Table 1.2: Chemical composition.

Component	Volume percentage, %
CO_2	96.5
N_2	3.5
SO_2	0.015
Ar	0.007
H_2O	0.002
CO	0.0017
He	0.0012
Ne	0.0007

Overall structure of atmosphere is shown in fig. 1.2. There is a layer of a fog between the altitudes 45 – 70 km. Most dense part of this fog is called "Venusian clouds". They differ from the tropospheric clouds at the Earth not only by low density and very small size of particles, but also by different composition: they consist of H_2SO_4 droplets. There are extended hazes below and, especially, above the clouds, consisting of even smaller particles.

Size and refractive index of Venusian cloud droplets were determined from polarimetric observations by Hansen and Hovenier (1974) resulting in important conclusion about sulphuric acid composition of clouds. Observations in visual band region (0.55 µm) were used.

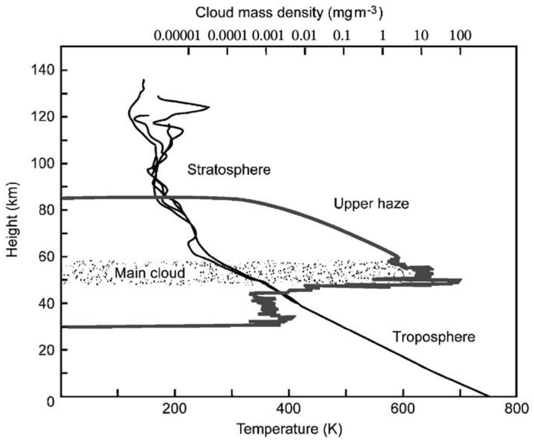

Figure 1.2: Temperature (bottom scale) and cloud density (top scale) profiles for Venus, based on measurements from several different instruments on the Pioneer Venus orbiter and entry probes. The figure is taken from Taylor (2006).

Figure 1.3 indicates that, for the refractive index ≈ 1.44, effective radius $(1.05 \pm 0.10)\,\mu\mathrm{m}$, and the effective variance 0.07 ± 0.20, the polarization is consistent with the observations. Results at other wavelengths confirm these values. Experiments with descent probes, in which *in situ* measurements of the atmosphere properties were performed, gave information about the at-

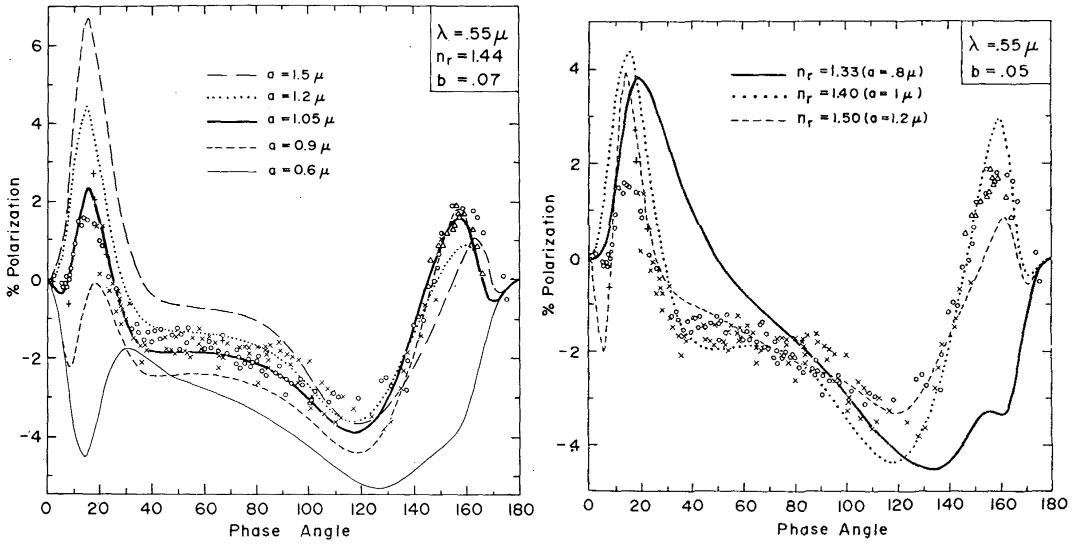

(a) Variations of the effective radius.

(b) Variations of the refractive index.

Figure 1.3: Observations of the polarization of sunlight reflected by Venus in the visual wavelength region and the theoretical computations for $\lambda = 0.55\,\mu\mathrm{m}$. The ○'s are wide-band visual observations by Lyot (1929) while the other observations are for an intermediate bandwidth filter centred at $\lambda = 0.55\,\mu\mathrm{m}$; the ×'s were obtained by Coffeen and Gehrels (1969), the +'s by Dollfus and Coffeen (1970), and the △'s (which refer to the central part of the crescent) by (Veverka, 1971). The theoretical curves in (a) are all for a refractive index 1.44. The different curves show the influence of the effective radius (a) and refractive index (b) on the polarization. The figures are from Hansen and Hovenier (1974).

mosphere down to the surface.

Clouds are stratified and have complicated, time varying structure, but main properties can be generalized. The global and time-averaged properties of the Venus clouds are following. “Upper clouds” — the uppermost cloud layer, is the level generally seen in visible remote-sensing and tends to be uniformly opaque and featureless, exhibiting contrasts which are observable mainly in the ultraviolet region. “Middle” and “lower” clouds as well as “upper clouds” characterizations are derived from *in situ* measurements of particle densities and sizes (Knollenberg and Hunten, 1979, 1980). Before the discovery of the near infra-red transparency “windows” in the Venus spectrum by Allen and Crawford (1984), the middle and lower clouds had never being observed by remote sensing techniques.

Descent probes performed *in situ* determinations of droplets sizes and optical properties. Particles in the clouds appeared to have trimodal size distribution. The smallest ones, abundant in hazes, have radii of less then 0.5 µm (so-called “mode 1”). The most abundant in clouds (“mode 2”) have radii ∼ 1 µm. The most part of the clouds mass is contained in largest particles (“mode 3”) with commonest radius of ∼ 15 µm (see fig. 1.4 and Knollenberg and Hunten (1980)).

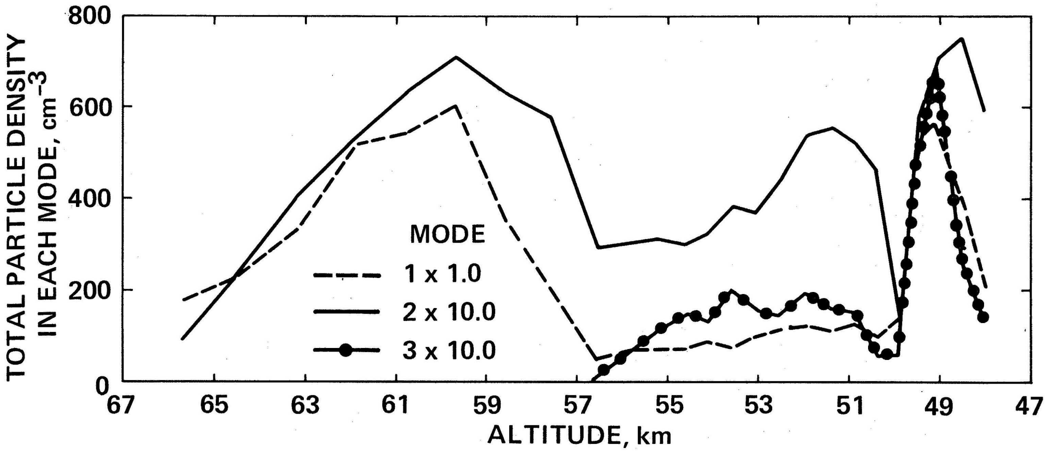

Figure 1.4: Particle number densities in the three size modes obtained from Large Probe Cloud Particle Size Spectrometer on-board Pioneer Venus probe. The five descent probes entered the atmosphere at different locations. These data, as presented in Kliore et al. (1986).

The properties and variability of haze and cloud particles were analyzed from Pioneer Venus Orbiter Cloud Photopolarimeter experiment (Kawabata et al., 1980). Analysis of linear polarization data indicates that the visible clouds at low and mid-latitudes are composed predominantly of 1 µm radius H_2SO_4 droplets (“mode 2” particles), an identification was made previously by using earth-based observations. “Mode 3” particles are H_2SO_4 droplets also. Mixed within and extending above this main visible cloud is an extensive haze of submicron-sized “mode 1” particles. These haze particles have a refractive index of 1.45±0.04 at $\lambda \simeq$ 0.55 µm, an effective radius of (0.23±0.04) µm, and a size distribution with an effective variance of 0.18±0.10. Composition of “mode 1” particles is still unknown. The sub-micron haze has been found to exhibit large spatial and temporal variations. Substantial diurnal variations exist at low latitudes, with a greater amount of haze near the morning terminator than near the noon meridian.

A number of models representing the structure of the atmosphere of Venus have been proposed since the early years of the exploration of Venus by spacecrafts (*e.g.* Avduevsky et al., 1970; Marov et al., 1973; Noll and McElroy, 1972; Kuz'min and Marov, 1974; Seiff, 1983b). They were relatively accurate for the deep atmosphere, but became increasingly uncertain for cloud levels and above. At the first Venus International Reference Atmosphere (VIRA) Workshop, at Hamburg in August 1983, models for the atmosphere below 100 km were proposed by Kerzhanovich et al. (1983), Seiff (1983a), and Schofield and Taylor (1983). They were based on results of *in situ* data from 15 Soviet and American atmospheric probes and remote sensing data from the Pioneer Venus Orbiter and number of US and the USSR flyby spacecrafts. Results of these works have been published in Advances in Space Research, volume 5, in 1985. Some additions were published after further missions (*e.g.* Moroz and Zasova, 1997). After Venus Express started to observe Venus in 2006, some of these data were clarified in details, but VIRA model is still the most complete description of the general properties of Venus atmosphere.

Measurements of the light flux during descents, combined with particle measurements, measurements of the gas properties, allowed to compile optical model of the atmosphere (see, *e.g.* Tomasko et al., 1980, 1985).

1.4 Venus surface

Two main sources of the information about Venus surface are the data of *in situ* analyses, obtained by the Venera landers, and the radar albedo, emissivity and topography maps obtained by Magellan mission. The landers cameras showed very dark, desert-like landscape, strewed by boulders and covered by fine dust (fig. 1.5). Radar albedo contains information about surface roughness (at the scale of the radar wavelength) and about electrical permittivity ε of the soil. The ε is connected (empirically) to the density of the soil. It has to be noted, that radar emission is sensitive to the depth of the order of wavelength. Another tool for the remote sensing of the surface is sounding in NIR transparency "windows". Because of the smaller wavelength, the NIR is sensitive to the very top (a few µm) of the surface.

1.4.1 Geology and surface properties

From the Magellan radar maps (fig. 1.6) it is seen that the Venus surface is dominated by volcanic plains, often called regional plains (*e.g.* Basilevsky and Head, 1998, 2000; Basilevsky and McGill, 2007), which have been interpreted to be formed by emplacement of mafic (basaltic) lavas. This inference follows from the results of the *in situ* analysis of the soil by the Venera and Vega landers in six sites located on these plains (Abdrakhimov, 2001a,b,c,d,f). The γ-ray spectrometers measured contents of uranium, thorium, and potassium appeared to be similar to the ones of the Earth basalts, and estimated the density of the soil, appeared to be $2.7 - 2.9\ \mathrm{g/cm^3}$, also similar to that one of the Earth basalts (see summary by Surkov, 1997). This is also supported by observations of plains morphology on high-resolution radar imagery (*e.g.* Barsukov et al., 1986; Head et al., 1992).

The most of the highlands regions (see fig. 1.6) are tesserae (Ivanov and Head, 1996; Tanaka et al., 1997; Ivanov, 2008). Tessera terrain (fig. 1.7), that covers approximately 8 – 10 % of the surface, is characterized by high relief comparing to surrounding plains, and by high surface roughness at scales from cm to m (Barsukov et al., 1986; Ivanov and Basilevsky, 1993). Tesserae

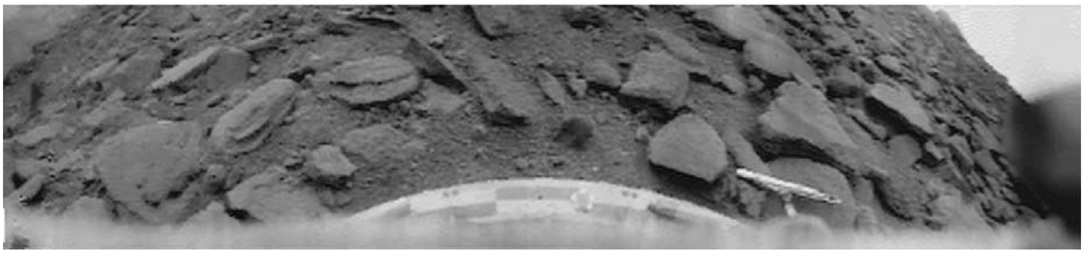

(a) Venera-9, at 32.1°N, inside the large continent of Beta Regio, on 22 October 1975.

(b) Venera-14, at 13.1°N, near the eastern flank of Phoebe Regio, on 5 March 1982.

Figure 1.5: Pictures of the surface of Venus obtained by Venera-9 (a) and Venera-14 (b). The Venera-14 site shows flat, basaltic rocks probably formed by the geologically recent break-up of volcanic lava flows, while Venera-9 shows what seem to be older, more weathered rocks sitting on a bed of finer material, like sand or soil. The details and ages of the processes that shaped these localities remain unknown, as does the stratigraphy and composition of the layers underneath the exposed surface. The chemical interaction of surface materials with the atmosphere may have a key role in explaining the extreme climate on Venus today. The figure's caption is taken from Taylor (2006).

usually form continent-like blocks or small islands that stand above and are embayed by the adjacent plains. None of the Venera or Vega geochemical probes landed on tessera terrain; thus, all information about its composition is indirect.

Venus surface has many different signs of tectonic activity. In the Magellan SAR images of Venus more than a hundred volcanic constructs larger than 100 km in diameter and about 300 constructs of 20 – 100 km in diameter are observed (Crumpler et al., 1997; Magee and Head, 2001). The youngest lavas related to these constructs are clearly superposed over regional plains. These large- and intermediate-size volcanoes are morphologically very similar to basaltic shield volcanoes on the Earth, although the latter are typically smaller than their counterparts on Venus. Venus does not have plate tectonics, and because of that hot-spots do not move (with respect to crust), and shield volcanoes accumulate lavas at the same place. A basaltic composition of lavas of at least one volcanic edifice is supported by the *in situ* geochemical measurements by Venera-14 (Surkov, 1997), which landed within the lavas of the Panina Patera volcano (Abdrakhimov, 2001e).

There are many coronae at Venus, which are large (typically several hundreds kilometres in size) circular structures. Largest of them are clearly visible on the global topography map (fig. 1.6), while examples of smaller ones are shown in fig. 1.8. They are believed to be formed by raising plumes of a hot mantle material, which push crust upwards.

Another volcanic feature is so called steep-sided, or pancake, domes. The steep-sided morphology of the domes suggests that they were formed by eruptions of viscous lavas(fig. 1.9).

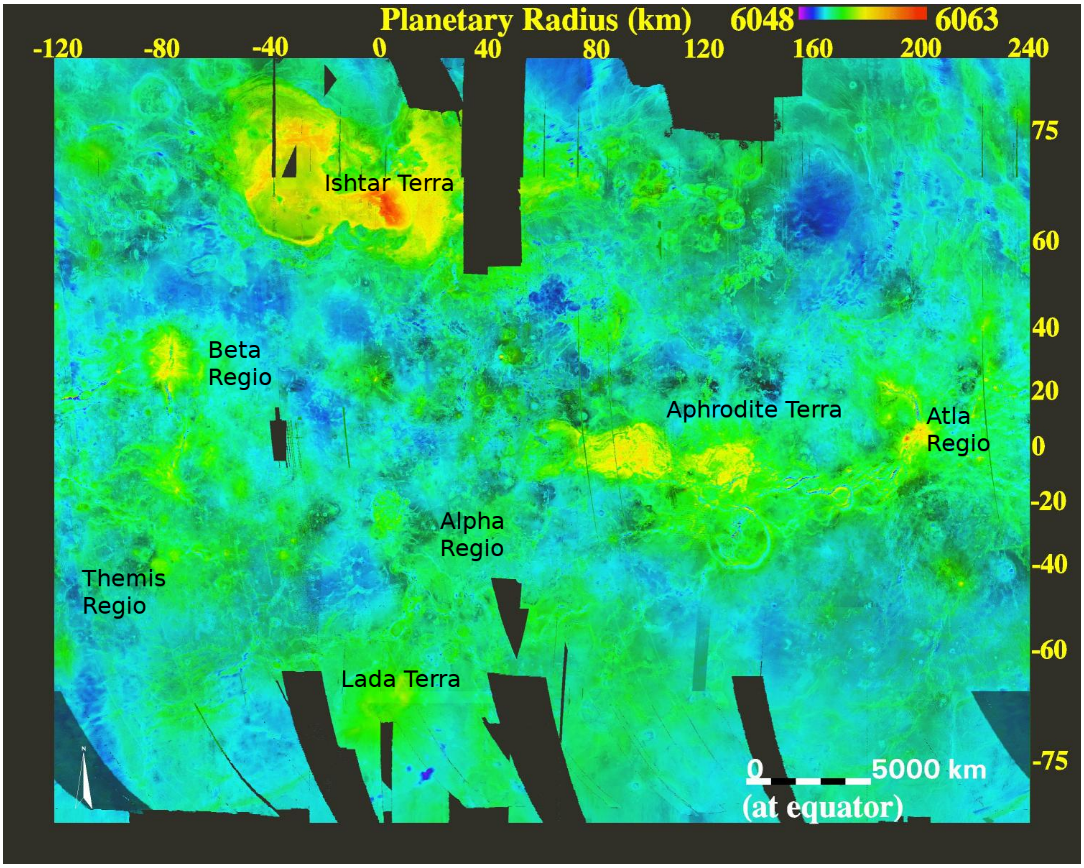

Figure 1.6: Topography is shown in colour and the SAR imagery defines the intensity in this map of Venus. Figure is taken from Herrick and Price (n.d.).

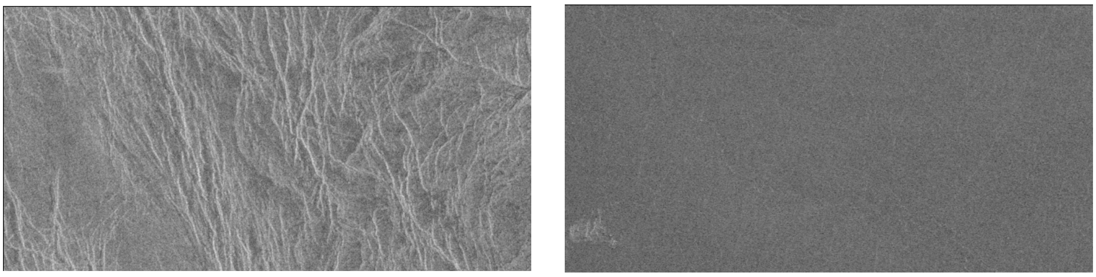

(a) Mosaic centred at 0° latitude, 274.26°E longitude, tesserae.

(b) Mosaic centred at 37°N latitude, 310.5°E longitude, plains.

Figure 1.7: Magellan SAR mosaics showing areas of ≈ 50 km by ≈ 27 km of tesserae terrain (a) with comparison to plains (b).

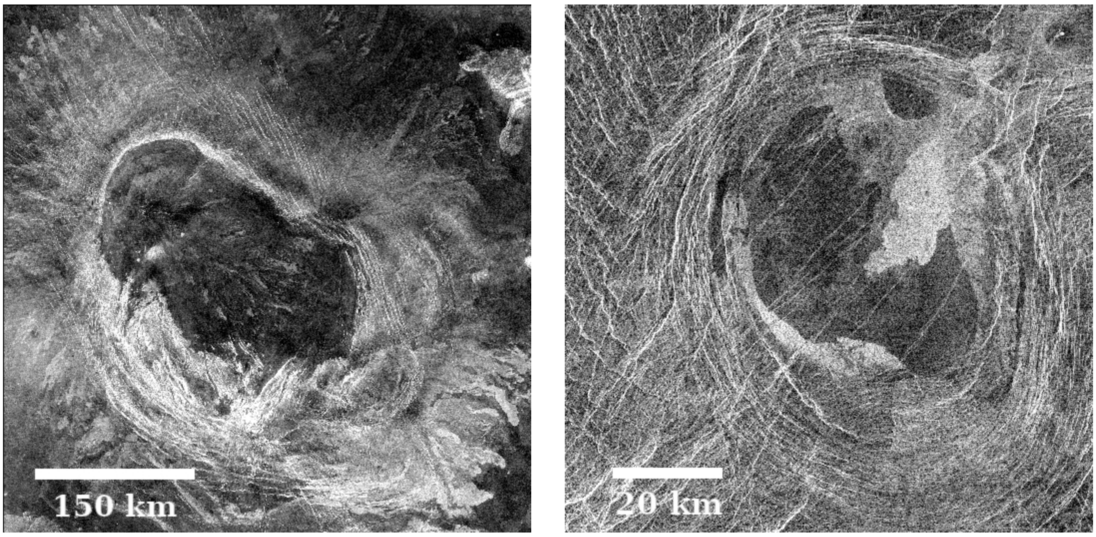

(a) Aruru corona, 9°N, 262°E.

(b) Small corona at 2.2°N, 219°E.

Figure 1.8: Magellan Venus Radar Mapping Mission (MGN) SAR images of the coronae.

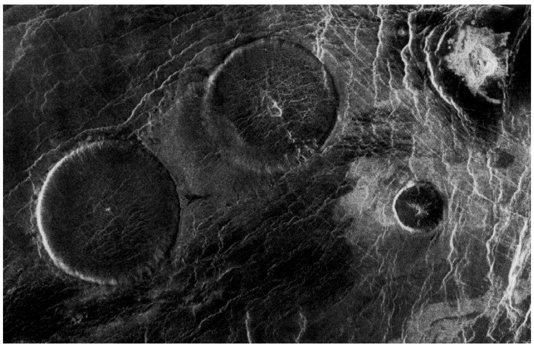

Figure 1.9: Magellan mosaic, centred at 12.3°N latitude, 8.3°E longitude, shows an area 250 km by 160 km in the Eistla region. The prominent circular features are volcanic domes, 65 km in diameter with broad, flat tops less than 1 km in height. Credits to NASA/JPL.

There are large rift systems on Venus. At the Earth the rifts are formed because of plates movements, but at Venus there are no such processes, *i.e.* the Venus crust is not divided into plates. Thus, formation of the rifts is driven by some local processes. Volcanic constructs on Venus are often associated with rifts resembling continental rifts of Earth (*e.g.* Schaber, 1982; Head et al., 1992; Solomon et al., 1992; Price and Suppe, 1994; Basilevsky and Head, 2000). Sometimes Venusian rifts are also sources of plains-forming lava flows.

Impact craters can be used, as usual, to estimate the age of the surface. There are around 1000 impact craters on Venus. Obviously, because of the dense atmosphere only large impactors can reach the surface. But even with this in mind, one would find the total number of craters surprisingly low, taking into account absence of water erosion on the planet. What is also interesting is that these craters distributed almost randomly (fig. 1.11). Some of them have radar-dark parabolic halos, that must be sign of their very young age (Basilevsky et al., 2003). Such distribution suggests that the age of the surface does not vary significantly. Together with the total number of craters it is possible to estimate the age of the surface to be

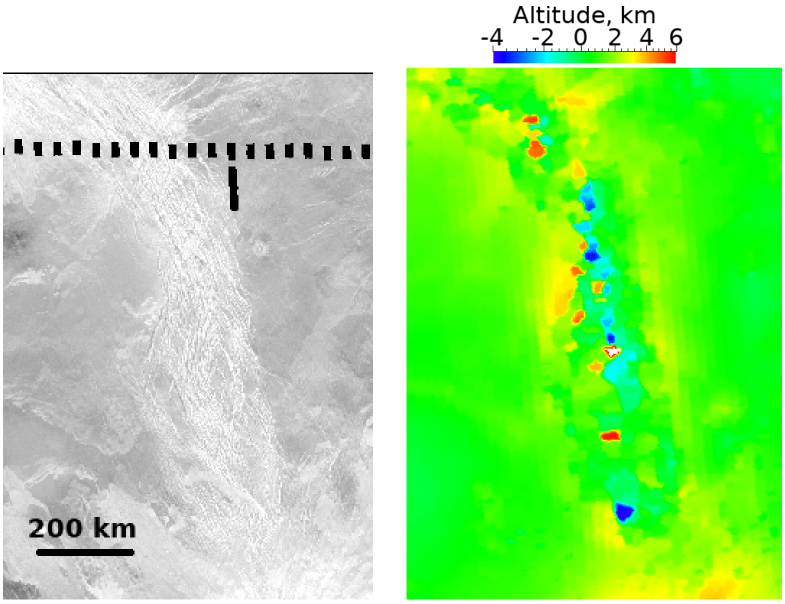

(a) MGN SAR.

(b) MGN topography map.

Figure 1.10: Example of rift. Images are centred at 11.5°N, 198.15°E.

500 – 700 Myr (Basilevsky and Head, 1998). There are no enough craters to determine the age of any particular surface feature, but for large ones it is possible. Some of the lava streams from volcanoes superimpose craters with radar-dark parabolas, that must be a an indication of their very recent activity. From impact craters density, the age of tesserae terrain appeared to be 1.4 times older than that of plains (Ivanov and Basilevsky, 1993).

1.4.2 Targets for sounding in NIR

Sounding in NIR can detect different emissivity of the surface and thus different composition. A few geologic features and units of the Venus surface could have non-basaltic, geochemically more evolved compositions. These are the following.

Tesserae Helbert et al. (2008), Mueller et al. (2008), and Gilmore, Mueller, et al. (2011) retrieved the 1-micron emissivity of tessera terrain in Lada Terra and Alpha Regio from the Visible and Infra-red Thermal Imaging Spectrometer (VIRTIS) data; they found that the tessera emissivity is different from the emissivity of the adjacent supposedly basaltic plains suggesting compositional difference. Nikolaeva et al. (1992) have compiled several lines of evidence that tessera can be composed of the material geochemically more differentiated than basalts, for example, essentially feldspatic materials such as silicic to intermediate rocks or anorthosites. Later, joint analysis of the gravity field and topography of Ishtar Terra allowed Kucinskas et al. (1996) to conclude that some parts of Maxwell Montes highland consisting of material structurally similar to tessera, could be composed of material less dense than basalt and possibly be silicic. Recently Gilmore, Resor, et al. (2011) have performed structural analysis of a block of tessera in Tellus region and applied a model of deformation formed the ridges in that block from the VIRTIS data analysis. They concluded that the material of this block could be a range of compositions including felsic (Gilmore, Mueller, et al., 2011). At the same time, in several

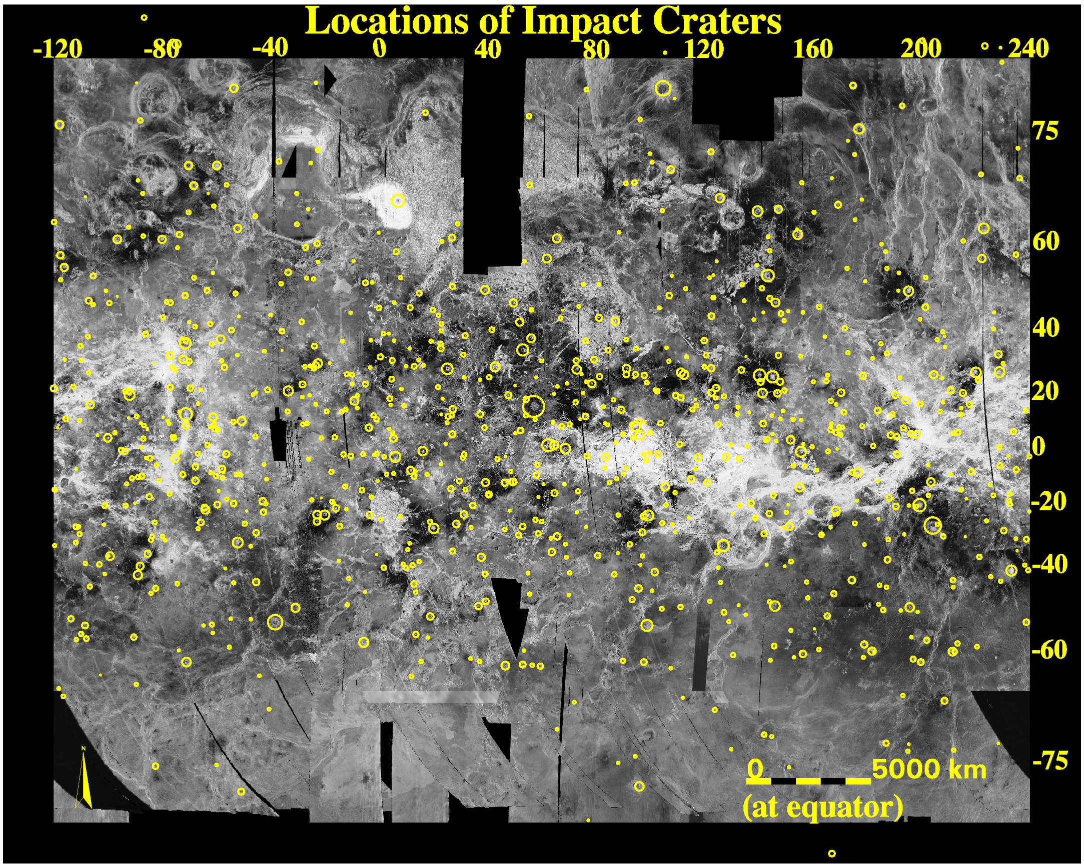

Figure 1.11: Impact crater distribution overlaid on SAR imagery. Symbols represent locations of impact craters on the planet, and symbol size indicates relative crater diameter. A few of the craters are correctly placed on the Mercator image but are located slightly beyond the formal map boundary. Figure is taken from Herrick and Price (n.d.).

localities Ivanov (2001) has observed evidence that tessera was formed through tectonic deformation of some precursor plains. Suggesting that these plains have basaltic composition, he concluded that the tessera material could be also basaltic. Tessera forms blocks of different sizes, up to several hundreds to thousands kilometres across, that makes it possible to study them through the analysis of the NIR emission in the atmospheric transparency "windows" despite of light scattering in the atmosphere.

Mountain tops seems to have different composition because they are very bright in radar rays at altitudes, higher than 3 – 4 km (Pettengill et al., 1992).

Steep-sided domes might be formed by more viscous lavas, which are often typical for geochemically evolved compositions (*e.g.* Pavri et al., 1992) although other suggestions on their nature have been published: low-eruption rate basaltic volcanoes (Fink and Griffiths, 1998), increased content of dissolved water and difference in crystallinity (Bridges, 1995) or foamy basaltic lavas (Pavri et al., 1992). Sizes of these features are only a few tens of kilometres, which is not good for NIR sounding.

Due to their wide areal distribution basaltic regional plains represent a good reference surface for the analysis of the NIR images of the surface. In places amid the regional plains there are areas of geologically younger morphologically distinctive volcanic plains, so-called lobate and smooth plains, which also seem to be basaltic based on morphology.

Another possible target for NIR sensing is fresh hot lavas. Due to their higher than normal surface temperature, the lava right after volcanic eruption must produce significantly higher NIR flux. Thus, NIR imaging can be used for detection of ongoing volcanic activity. The highest volcano on Venus, Maat Mons, stands about 9 km above the mean planetary radius of 6051.8 km. Lava flows radiating from Maat Mons cover an area about 800 km across. In their eastern extension, these lavas are superposed on 40-km crater Uvaisy, which has an extended radar-dark parabola. Presence of the latter suggests that crater is very young, not older than a few tens of millions years (Basilevsky, 1993; Basilevsky and Head, 2002a). This is a strong indication that Venus has volcanoes active in the geologically recent time with high chances that some can be active at the present time, although the mean rate of venusian volcanism in the geologically recent time is probably by 1 – 2 orders of magnitude lower than the mean rate of volcanism of the Earth in the current geologic epoch (Basilevsky and Head, 2002b).

Since NIR emission originates from the very top of the surface, it is sensitive to the properties of the very thin layer on the surface. Matter of this layer can be a subject for changes via chemical weathering and eolian resurfacing (in particular, fine dust is visible in surface panoramas from landers), let us consider these processes with application to Venus.

1.4.3 Chemical weathering

Surface materials on Venus most likely are involved in chemical interaction with atmospheric gases. Thermodynamic calculations (see *e.g.* Barsukov et al., 1980, 1982; Klose et al., 1992; Fegley Jr., 2003; Zolotov, 2007) supported by still scarce modeling experiments (*e.g.* Fegley and Prinn, 1989; Johnson, Fegley, et al., 2003; Abbey et al., 2011) suggest several effects of chemical weathering on Venus, including: 1) oxidation and sulfurization of surface rocks through gas – solid-type reactions; 2) isochemical weathering of individual solid phases with respect to elements being nonvolatile at Venus' surface temperature (*e.g.* Al, Si, Mg, Fe, Ca, Na); 3) a strong altitude-dependent effect for the chemistry and physics of gas – surface interactions. Current hydration of anhydrous phases is considered as unlikely and original hydrated phases (if any) would be dehydrated (Zolotov, 2007).

At plains elevations the expected mineral assemblage of weathered basalts includes (in order of decreasing abundance): plagioclase, clinoenstatite, pyrite or magnetite, anhydrite or diopside, microcline, and a few minor phases (Barsukov et al., 1982; Klose et al., 1992). Later considerations showed that redox conditions on the plains level of Venus are most probably close to coexistence of magnetite and hematite and thus pyrite can not be stable there (Fegley, Klingelhofer, et al., 1995; Fegley, Lodders, et al., 1995; Zolotov, 1996, 2007). The major difference of the assemblage of weathered basalts from that of unweathered basalts is the expected presence of anhydrite ($CaSO_4$) formed due to sulfurization of diopside ($CaMgSi_2O_6$) and anorthite component of plagioclase ($Ca_2Al_2Si_2O_8$) as well as presence of hematite (Fe_2O_3) due to oxidation of olivines and pyroxenes containing ferrous iron (*e.g.* Zolotov, 2007). Presence of hematite and anhydrite in the weathered surface material of Venus was assumed in a recent paper of Smrekar et al. (2010). A degree of possible chemical weathering on Venus is unknown but its effect should be most prominent for the uppermost surface layer and thus potentially could influence the NIR emission. Appearance of anhydrite may be noticeable in the NIR observations because of its high reflectivity and thus low emissivity at 1 micron wavelength (see below).

The chemical surface modification effect is directly seen in the results of the microwave remote sensing of Venus in the areas higher than some critical altitude, typically ≥4 km above the mean planetary radius. These mountain tops, with a few exceptions, show very low microwave emissivity (and correspondingly very high radar reflectivity). These microwave emissivity anomalies are a subject of controversy and have been attributed to the temperature-controlled presence of conductive, semiconductive, ferroelectric or ferrimagnetic materials (*e.g.* Klose et al., 1992; Pettengill et al., 1997; Shepard et al., 1994; Starukhina and Kreslavsky, 2002; Wood, 1997). Among the proposed variety of materials, the least exotic and the most plausible from physical chemistry point of view are hematite, magnetite or pyrite. The 1-micron emissivity of these minerals, however, is rather close to that of unweathered basalts so the mountain tops mineralogy is probably not a promising target for the NIR image analysis.

There are no reliable data on how fast chemical surface modification works on Venus. Only one estimate (applicable to high altitudes) is available: Klose et al. (1992) noted that the top surface of very high (9 km) Maat Mons volcano shows a significant decrease in microwave emissivity only in some places while most part of its summit has microwave emissivity close to the values typical for the plains. The authors of this work suggested that this is because this volcano is so young that only earliest lavas of it had enough exposure time to get chemically modified, while the majority of its lavas had not. It should be kept in mind that microwave signature considered by Klose et al. (ibid.) is relevant to upper centimetres of the surface while the NIR optical properties are relevant to upper microns and chemical alteration of the micron layer is obviously much faster than in the centimetre-thick layer. The hypothesis of a very young age of Maat Mons volcano was then independently supported by the above mentioned studies of Basilevsky (1993) and Basilevsky and Head (2002b). They analysed age relations of lavas of this volcano with the crater Uvaisy having associated radar-dark parabola implying that at least part of lavas of this volcano formed less than a few tens of millions years ago, while the mean surface age of Venus is estimated to be of several hundred millions of years (McKinnon et al., 1997). The fact that all other high enough mountains on Venus have the low emissivity tops suggests that they are old enough for the chemical modification to be developed. Some of these highs (Maxwell, Ovda) have ages somewhat older than the mean surface age of Venus, but majority of the highs are younger. For example, the Beta Regio rise has microwave low-emissivity tops and associated rifting in Devana Chasma shows evidence of activity more recent than 0.5 of the mean surface age (Basilevsky and Head, 2002b, 2007).

Pieters et al. (1986) measured spectra of hematite heated up to temperature of 500 °C and compared them with the data taken by the Venera-9 and Venera-10 wide-angle spectrophotometer (Ekonomov et al., 1980). They concluded that the spectra of the surface materials at the landing sites resemble the spectra of hematite and hematite-bearing weathered basalt, rather than that of magnetite. Because hematite is not typical for unaltered basalts, this suggests that surface materials in these sites are weathered (oxidized).

The Venera-9 site is in the area with tectonic steep-sloped graben (Abdrakhimov, 2001f) where down-slope mass wasting and thus rather effective resurfacing is logical to expect. The Venera-10 site is in the regional plains (Abdrakhimov, 2001c) with almost absent steep slopes that suggests negligible role of the down-slope mass wasting and associated resurfacing. Thus, if observations of Ekonomov et al. (1980) are interpreted as indication on the chemically weathered surface in the Venera-9 and Venera-10 sites, then one can conclude that the chemically weathered surface material is typical not only for plains (Venera-10) but for the areas with indications on down-slope mass wasting (Venera-9).

Wood (1997) calculated how much sulfur could be present in the Venera-13, Venera-14 and Vega-2 surface materials, if they would be totally weathered (sulfurized) basalts, and compared the result with the actually measured sulfur contents; he concluded that weathering is only partial: 50 % for Vega-2 and 7 – 20 % for Venera-13 and Venera-14. The analysed samples, each about 1 cm^3, were taken by drilling from the depth down to ~ 3 cm. Thus, these estimates represent the mean weathering degree in a few centimetres thick surface layer, while for the very surface seen in NIR range, the weathering degree can be essentially higher.

The Venera-13 and Venera-14 landers also measured electrical resistivity of surface soil and found it unexpectedly low: 89 and 73 Ω m respectively (Kemurdzhian et al., 1983). A co-author of Kemurdzhian et al. (ibid.), V. V. Gromov, (personal communication to J. Wood) ascribed "this low resistivity to the presence of a thin film of electrically conductive material on the soil particles" (Wood, 1997, page 649). Presence of high content of magnetite can also lead to low resistivity. This is evidence of the weathering of surface material.

Thus, the observations *in situ* and their analysis suggest that the Venus surface material, especially its thin uppermost layer, is mineralogically modified, unless the material has been exposed for rather short time due to its recent emplacement or continuing resurfacing. The case of recent emplacement is probably exemplified by the summit of Maat Mons discussed above. The cases of ongoing resurfacing are probably associated with down-slope material movement, which in scale and intensity probably is most prominent on slopes of rift zones and walls of large impact craters. These slopes however have large range of altitudes at short horizontal distances, which makes them difficult to be analyzed using the NIR observations (see section 2.1.2.1 for clarification why it is so). Besides, as it was mentioned above, observations by Ekonomov et al. (1980) in the place with the down-slope material movement (Venera-9 site) provide evidence of chemically weathered rather than unweathered material.

1.4.4 Eolian resurfacing

Volcanic and tectonic features on Venus may be affected by eolian resurfacing caused by normal "meteorological" winds (Greeley et al., 1997) and locally by strong winds, which are thought to accompany impact cratering events (Ivanov et al., 1992; Schultz, 1992). The eolian features observed in Magellan SAR images are represented by radar-dark mantles, wind streaks, yardangs and dunes. The first two types of eolian features are rather common on Venus, while the features of the second two types, large enough to be seen on the Magellan images, are observed only in a few localities. Yardangs indicate effective wind erosion but their rarity (Greeley et al., 1997) suggests that wind erosion does not play a great role among surface processes on Venus at the scale of features observed on the Magellan images.

For smaller features, however, deflation, eolian transport and deposition certainly play an important role. It is seen, in particular, in localization of the surface fines (considered to be a loose material) in local lows in between slab-like outcrops of the finely-layered rocks at the Venera-10, Venera-13 and Venera-14 landing sites (Florensky et al., 1977; Basilevsky et al., 1985). Deflation of loose fines was directly observed in panoramas taken by the Venera-13 lander. The three panoramas taken with 20 min time interval showed that a clod of dark fines thrown at the landing upon the supporting ring of the lander was shrunk with time to much smaller size. The only reasonable explanation of this observation is deflation of this fine material by the near-surface wind (Selivanov et al., 1983).

For our analysis we have a special interest in radar-dark mantles, which represent a veneer of fine-grained material covering the local bedrock. Radar-dark mantles are commonly seen in association with impact craters, forming halos of different sizes and forms. They look dark in SAR images because their surface is smooth (Campbell et al., 1992; Bondarenko and Head, 2009). The source of the radar-dark-mantle material is fine debris formed and lifted into atmosphere by crater-forming impacts and then deposited from the air. When the fine-grained ejecta material is at high levels of the atmosphere, it is driven by strong zonal winds and travels long distances before it is deposited on the surface and covers the local material. This is how the hundreds- to thousands-km-long radar-dark parabolas associated with young impact craters form (Campbell et al., 1992; Vervack and Melosh, 1992).

With time, the deposited material is being reworked by the near-surface winds. Its surface looses its smoothness and extended radar-dark parabolas shrink into smaller non-parabolic radar-dark haloes and then the haloes disappear. But significant part of the deposited material is essentially not moved far away and we probably see it in the TV panoramas taken by the Venera landers as the mentioned above slabs of fine-layered lithified material (Florensky et al., 1977; Basilevsky et al., 1985). Basilevsky et al. (2004, 2007) have shown that these fine-grained debris probably represent the ejecta material of the upwind impact craters but not the local bedrock. The radar-dark crater-related deposits are not seen on tessera terrain, probably because the deposits of loose material do not cover completely all steep scarps making the radar-bright tectonic fabric of tessera, and the strong radar signature of the tectonic fabric totally overwhelms that of the crater-related deposits. Thus, looking in NIR transparency "window" on the surface of tessera we might see not tessera material but material ejected from the upwind crater(s) which could be derived from very different (from tessera) geologic unit(s). This possibility should be taken into account in further analyses.

The velocity of near-surface winds, which are a driving force of eolian resurfacing, have been measured by the Venera landers using anemometers and by recording the acoustic noise after landing (see, for example, Avduevskii et al., 1976; Ksanfomality et al., 1983). It was found to be about 0.5 – 1 m/s. The landers made these measurements on venusian plains with altitude level close to the mean radius of Venus. On higher elevations wind velocity should be higher. We can roughly estimate it from the Doppler tracking of the Venera/Vega and Pioneer Venus landers during their descent in the atmosphere. The lowest altitude where reliable measurements made by this technique were done is 10 km above the mean radius of Venus and wind velocities there were found to be from 2 to 10 m/s (see summaries in Schubert et al., 1980; Moroz, 1981; Kerzhanovich and Marov, 1983). So the vertical gradient of wind velocity is probably from a few dm/s to about 1 m/s per kilometer of altitude and we may expect that on the surface of high-standing landforms the wind velocity is noticeably higher than at lows so the smaller particles may be suspended and blown to the lowland (Leeder, 2007).

Besides, the mentioned above strong winds, which are believed to accompany impact cratering events (Ivanov et al., 1992; Schultz, 1992) might episodically strip out and suspend in the air the loose surface material which would not be mobilized by normal "meteorologic" winds. Taking in mind that for the morphologically observed part history of Venus, these events ($\sim$ 1000) together with blasts of meteoroids in the lower atmosphere (responsible for formation of "splotches") could play a noticeable role in the mobilization and redistribution of fines on the surface of this planet.

1.4.5 Reflectivity and emissivity of potential surface materials at 1 micron wavelength

In attempt to study mineral composition of Venus surface through analysis of the NIR emissivity, spectral data on materials, which are potentially present there, have been collected and analysed. These materials are: 1) basalts as major candidates for rocks composing dominant part of venusian surface and 2) more silicic rocks, rhyolites and andesites, which could compose tessera terrain, as well as some minerals. Among the latter are some components of basalts, minerals, which are considered to be products of chemical weathering on Venus surface, and some minerals hypothesized to be present on the low-microwave-emissivity mountain tops. Spectral data on Ca-rich plagioclases anorthite and labradorite, as well as on anhydrite, hematite, magnetite and pyrite have been collected from the ASTER spectral library (http://speclib.jpl.nasa.gov, Baldridge et al., 2009) and Brown University Keck/NASA Relab Spectra Catalog (http://www.planetary.brown.edu/relab/) to estimate emissivity values of these materials at 1 µm. Due to the absence of laboratory data on mineral and rock emissivity (ε) in the near-infrared spectral range, 1-µm reflectivity (R) has been used, and Kirchhoff's law ($\varepsilon = 1 - R$) applied. All types of reflectances (bidirectional, hemispherical and biconical) have been used, which is not rigorously grounded, and our quantitative results on ε should be treated with caution, while the trends are qualitatively reliable.

Note that the material reflectivities/emissivities at the considered wavelength depend not only on the material composition and temperatures but also on the particle size. For silicates and common rocks, whose optical properties at 1 µm are controlled by volume scattering, reflectivities at 1 µm typically increase with decreasing particle size (see table 1.3). The opposite trend or the lack of particle size dependence are typical of highly absorbing materials, *e.g.* magnetite and sulfides.

Table 1.3: The biconical reflectivities of several samples of rock-forming minerals at 1 µm as a function of grain size, from Moroz et al. (2007). The samples are described in Helbert et al. (2007).

Mineral	Reflectivity of different size (in µm) fractions			
	0 – 25	25 – 63	63 – 125	125 – 250
Anorthite	0.70	0.60	0.53	0.43
Oligoclase	0.78	0.76	0.70	0.62
Orthoclase	0.72	0.64	0.57	0.47
Ortho-pyroxene En85	0.45	0.25	0.17	0.1
Olivine Fo90	0.48	0.28	0.18	0.1

As follows from the collected data, a negative correlation between 1-µm reflectivitiy and particle size is typical for basalts, rhyolites and andesites, as well as for anorthite, labradorite, and anhydrite. For example, the mean value of the 1-µm reflectivity of fine-grained basalts is ~ 0.2 while for the coarse-grained separates and whole rock chips it is by 2 – 3 times lower. Hematite reflectivity at 1 µm is also higher for the finer size fractions and rather high (up to 0.4) for nanophase synthetic powders (Baldridge et al., 2009; Morris et al., 1985), meanwhile the 1-µm reflectivity of magnetite for finer size fractions is slightly lower than for the coarser ones, while pyrite shows no prominent dependence of this sort.

As mentioned above, rocks and minerals on the surface of Venus are probably chemically weathered. This weathering happens through the surface-atmosphere interaction in the oxidizing environment (*e.g.* Zolotov, 2007) at not very high temperature and very low partial pressure of H_2O. In this environment, the major rock-forming components (Na, Si, Mg, Al, Ca, K, Fe) do not form volatile species (*e.g.* Wood, 1997). So the primary minerals and glasses decompose and recrystallize *in situ* with or without addition of oxygen and/or sulfur dioxide from the atmosphere into new mineral assemblages (*e.g.* Zolotov, 2007). So we assume that surface materials on Venus are typically fine-grained, and for the materials of our interest we consider mostly 1-µm reflectivity of fine (<25 to <5 µm) separates. Other researchers (*e.g.* Smrekar et al., 2010) also consider that weathering products are fine-grained. Very young lavas, however, probably have rough unweathered surfaces and thus should show lower 1-µm reflectivity. And for the high-standing landforms we may suspect eolian removal of the fine-grained fractions so the residual fractions may be coarser and thus have lower reflectivity (and higher emissivity).

The acquired from the above mentioned spectral libraries mean values of 1-µm reflectivity for fresh and weathered (oxidized) basalt, as well as for rhyolite, andesite, anorthite, labradorite, anhydrite, hematite, magnetite and pyrite are given in the "Room temperature" line of table 1.4. The table shows that relatively dark in visual range fine-grained powders of fresh and weathered basalt, hematite, magnetite and pyrite are also dark at 1 µm, while visually brighter fine-grained powders of rhyolite, andesite, anorthite, labradorite and anhydrite are also brighter at 1 µm. The table also contains mean values of calculated emissivity ($\varepsilon = 1 - R$).

It was found in several works that for common rock-forming minerals reflectance spectra, in general, and reflectivity at some wavelengths, in particular, may significantly change with temperature (*e.g.* Singer and Roush, 1985; Pieters et al., 1986; Roush and Singer, 1986; Moroz et al., 2000). These changes can be due to temperature-dependent change of amplitude of the thermal vibrations of absorbing cations about the centres of their coordination sites, resulting in widening an absorption band as the temperature increases (Burns, 1970). An increase in temperature may also change bond lengths between cations and surrounding ligands, resulting in wavelength shifts of electronic absorption bands. These shifts would affect reflectivity values at band wings. Since we are interested in the reflectance values at 1-µm, minerals with absorptions band wings at this wavelength (notably low-Ca pyroxenes) would be especially affected by temperature.

Hinrichs and Lucey (2002) showed that at the temperature increase from 80 K to 400 K (from (−193 °C to 127 °C), the 1-µm reflectivity changes from 0.43 to 0.2 for orthopyroxene En86, from 0.265 to 0.225 for eucrite EET83551, and from 0.125 to 0.09 for mature basaltic lunar soil 12023. The changes are correspondingly 54, 15 and 28 %. This temperature dependence of 1-µm reflectivity is just an example and cannot be applied to all pyroxenes and basaltic rocks. Basaltic rocks may vary in composition and contents and sizes of opaque grains. 1-µm reflectivity of basalts containing low-Ca pyroxenes and/or poor in fine-grained opaques should depend on temperature more significantly compared to basalts enriched in high-Ca clinopyroxenes, olivines, and/or opaques (see *e.g.* Burns, 1993).

Based on the results of Hinrichs and Lucey (2002) one can suggest that for basalts the decrease of the 1-µm reflectance due to temperature increase from 80 K to 400 K ($\Delta T = 320$ K) may be ~ 20 %. As a very rough guess we can suggest that for basaltic materials, the temperature increase from the room temperature to the Venus surface temperature ($\Delta T \approx 500$ K) could lead to the 1 µm reflectance decrease by maximum 30 %. Pyrite and magnetite show

Table 1.4: Estimates of the 1-µm reflectivity/emissivity for potential candidates materials of Venus surface materials.

Material	Number of samples	Samples	Reflectivity/emissivity	
			∼ 20 °C	∼ 500 °C
Basalt fresh	11	Kilauea, samples H1, 2, 5. 7, 9, 10; Mariana isl., 4f; C. Massif, France	0.2/0.8	0.15/0.85
Basalt oxydized	1	C. Massif, France	0.3/0.7	0.2/0.8
Rhyolite	1	Custer Co	0.5/0.5	0.5/0.5
Andesite	2	andesi1f, andesi2f	0.3/0.7	0.3/0.7
Anorthite	1	TS05Af	0.7/0.3	0.7/0.3
Labradorite	3	Lake Co, Oregon, Nain, Labrador	0.7/0.3	0.7/0.3
Anhydrite	6	Birmingham, Bouse, Mesab, unknown location	0.7/0.3	0.7/0.3
Hematite	2	Nova Scotia, Ajo	0.2/0.8	0.15/0.85
Magnetite	20	Utah, Langesundfjord, Balmet, San Benito — 2 samples,San Bernandin, Hot Sping, Grangesberg, Oka, Gladhammar, Marquette, Barrio, Mother Lode, Evje Washington, Glacier MP, Nye, Iron Co, Putnam, Sussex	0.05/0.95	0.05/0.95
Pyrite	4	Rio Mariana, Rouyn District, Austin, Alberta	0.12/0.88	0.12/0.88

electronic absorption bands centered at 1 µm. If these bands do not significantly shift at high temperatures, we suggest that their 1-µm reflectivity does not change significantly. This is not the case for hematite, which shows an absorption band at 0.85 µm, so that the 1-µm reflectivity (long wavelength wing of the band) can significantly decrease at 500 °C. If the band does not shift with temperature, based on the data of Pieters et al. (1986) for wavelengths shorter than 0.8 µm we can roughly estimate that the 1-µm reflectivity decrease by maximum 30 % may be expected at 500 °C. For minerals and rocks having low iron content and stable at 500 °C the effects of Venus temperature on 1-µm reflectivity are probably minor or negligible. Here we assume that temperature dependence of 1-µm emissivity does not differ from that of $(1 - R)$. Our estimates for 1-µm reflectivity (emissivity) of materials expected on Venus surface for the room temperature and the Venus environment are summarized in table 1.4.

The data and estimates given in table 1.4 show that fresh and weathered basalts have rather close high temperature emissivity ($\varepsilon \approx 0.8$) and these are values expected for Venusian plains and for majority of volcanic constructs. Materials expected to be present on the mountain tops (iron oxides and sulphides) have the high-temperature emissivity ($\varepsilon \approx 0.9$) only slightly higher than basalts, so probably they cannot be distinguished from basalts in the NIR image analysis. Materials which could compose tesserae (rhyolites, andesites as well as anorthitic and labradoritic anorthosites) all except andesites probably have high-temperature emissivity significantly lower (0.5 and less) than those of basalts and this gives hope to find in further analysis if tesserae are basaltic or not. Comparison of tables 1.3 and 1.4 shows, however, that the emissivity dependence on grain size could be more significant than the dependence on mineralogy and this makes the analysis even more difficult (see also Helbert et al., 2008).

1.5 Key questions, goals of the study. Thesis structure

Venus Monitoring Camera (VMC) maps Northern hemisphere of Venus using observations of the night side in 1 µm transparency “window”. This dataset is unique in terms of coverage both in space and in time. Since NIR emissivity of different materials, which are expected to be present on the surface is estimated to vary, observations of the surface in NIR give unique opportunity to detect differences in the surface composition on large spatial scales. In foreseeable future such information can be obtained only by remote sensing. Even detection that composition of some terrain differs from its surrounding might be very much helpful for understanding of the geology of the planet. Unusually high flux in the NIR range might indicate the presence of a hot spot on the surface. Such a spot would mean presence of hot lava and ongoing volcanic eruption. The data of night-side VMC observations cover significant part of the Northern hemisphere of the planet and give opportunity to study systematically variations of the surface composition and search for volcanic activity.

Unfortunately, the hot and dense atmosphere above the surface absorbs significant part of the surface emission. Up to now, there is no laboratory data for the continuum absorption of the CO_2 and H_2O under Venus conditions (high temperature and pressure). Thus, the information about absorption can not be obtained independently but instead has to be derived from the VMC data itself. To do that, observations of the plains could be used, where one does not expect composition (and thus emissivity) variations.

The goals of the thesis are: to study emissivity of the Venus surface and variations of mineralogical composition and to search for the present volcanic activity by analysis of the VMC images in the 1 µm transparency "window".

Since the Venus surface is observed through the thick clouds we made a special effort to model the light propagation through the atmosphere, compare results with VMC images, and derive emissivity of the surface or absorption of the atmosphere.

Thus, the following questions had been fulfilled by the thesis:

1. Determine sensitivity of the VMC NIR night side images to the surface properties (emissivity).
2. Develop a strategy of the VMC nigh side observations.
3. Develop a data processing pipeline for the VMC night-side near-infrared images.
4. Implement radiative transfer code to produce synthetic images of the surface for comparison with VMC observations.
5. Estimate absorption in the very lower atmosphere.
6. Retrieve from VMC images and compare emissivities for plain and tessera terrain (as well as for other interesting geological objects).
7. Search for a present volcanic activity in VMC images and assess detectability of the potential hot lava spots on the surface under various conditions.

The thesis is structured as follows:

Chapter 1 gives short overview of the Venus explorations, summarizes known facts about its atmosphere and surface, and introduces the goals of the work.

Chapter 2 describes VMC observations and data from Magellan mission, used in the study.

Chapter 3 describes used models and techniques, in particular radiative transfer model and data reduction pipeline.

Chapter 4 presents results of the emissivity retrievals for a particular regions.

Chapter 5 contains searches for ongoing volcanic activities, and analysis of their results.

Chapter 6 contains conclusions and further studies.

2 Observational data

2.1 Venus Express mission

The mission is aimed at investigations of planet's atmosphere, plasma environment and addresses some aspects of the surface physics (Svedhem et al., 2007). The Venus Express (VEX) spacecraft payload consists of 7 instruments (5 of them were inherited from other missions, 2 — designed specifically for this one). VEX continues intense exploration of Venus, that was done in 1970 – 1980 by series of Venera and Pioneer spacecraft, and then in 1990 – 1994 by Magellan mission.

The key topics for the mission are (ibid.):

- atmospheric structure;
- atmospheric dynamics;
- atmospheric composition and chemistry;
- cloud layer and hazes;
- energy balance and greenhouse effect;
- plasma environment and escape processes;
- surface properties and geology.

VEX has been launched on 9th of November 2005 and inserted into an orbit on 11th of April 2006. Since that time the spacecraft operates on polar, highly elliptical orbit (altitude in pericenter — hundreds of kilometres, altitude in apocenter — around 66 000 km), with orbital period of 24 h.

VEX conducts observations of the plasma and magnetic environment around Venus, its atmosphere and surface. Very brief descriptions of the experiments with references to the detailed specifications follow (ibid.).

ASPERA: an analyser of space plasma and ENAs The ASPERA-4 instrument is a copy of the ASPERA-3 instrument on-board Mars Express (Barabash et al., 2007). It comprises five sensors: two Neutral Particle Detectors (NPD1 and NPD2), a Neutral Particles Imager (NPI), an Electron Spectrometer (ELS), and an Ion Mass Analyser (IMA).

MAG: the magnetometer MAG is a magnetometer with two fluxgate sensors to measure magnitude and direction of the magnetic field around Venus (Zhang et al., 2006).

PFS: a high-resolution IR Fourier spectrometer The planetary Fourier spectrometer is an IR spectrometer optimised for atmospheric studies (Formisano et al., 2006). The experiment is inherited from the Mars Express mission with a few modifications. The two channels of the instrument together cover spectral range 0.9 – 45 µm with a boundary at about 5 µm. Unfortunately, due to an operational failure it does not work.

SPICAV/SOIR: A UV and IR spectrometer SPICAV/SOIR is a suite of three spectrometers to study the atmosphere of Venus in solar and stellar occultation, limb and nadir geometry (Bertaux et al., 2007). SPICAV-UV is a highly sensitive instrument in the range of 110 – 310 nm with resolution of 1.5 nm based on an intensified CCD detector. The SPICAV-IR covers the range 0.7 – 1.7 µm with a resolving power of 1500.

VERA: the radio-science experiment The Venus Express Radio Science Experiment uses radio signals of the telecommunication subsystem at X- and S-bands (3.5 and 13 cm wavelengths, respectively) to probe the neutral atmosphere and the ionosphere, surface properties, gravity field, and the interplanetary medium (Häusler et al., 2006).

VIRTIS: a visible and near-IR imaging and high-resolution spectrometer The VIRTIS instrument consists of two major parts: a mapping spectrometer (VIRTIS-M) that covers the range 0.25 – 5 µm with moderate spectral resolution ($\lambda/\Delta\lambda \approx 200$), and a high spectral resolution spectrometer (VIRTIS-H) for the spectral range 2 – 5 µm ($\lambda/\Delta\lambda \approx 1200$), (Drossart et al., 2007). The field of view of VIRTIS-M is 64 mrad and the pixel size is 0.25 mrad. The single resolution cell of VIRTIS-H is 0.58×1.75 mrad.

VMC: the Venus monitoring camera The VMC is a wide-angle camera for observation of the atmosphere and the surface through four narrow-band filters. The instrument consists of one unit that houses optics, CCD detector, and electronics (Markiewicz et al., 2007). The camera field of view is 17° with an image scale of 0.7 mrad/px, which results in a spatial resolution from 0.2 km at pericentre to 50 km at apocentre.

While VEX is mainly targeted at atmospheric studies, VMC together with VIRTIS performed imaging of the thermal radiation from almost the whole Venus surface. VMC observations cover the Northern hemisphere and VIRTIS — the Southern. In combination with MGN data these observations provide a unique possibility to investigate surface properties (see section 1.5).

2.1.1 Venus Monitoring Camera instrument

The VMC is an instrument, designed to perform imaging of the planet atmosphere and observations of the surface when the spacecraft is in the planet's shadow (Markiewicz et al., 2007; Titov et al., 2012). The VMC takes images in four spectral channels (fig. 2.1 and table 2.1). These channels are: UV — for studying clouds morphology, atmosphere dynamics and so-called "unknown UV absorber" — substance that is responsible for contrast in UV images of Venus, VIS — for studying airglow in the night atmosphere, and two near-infra-red channels: NIR1 and NIR2, the first one is centred at the water absorption band and the second one — at the atmosphere transparency window (*e.g.* Meadows and Crisp, 1996). And, of course, all of that channels might be used for studying the clouds and hazes by modelling the scattering of light inside them.

All VMC filters share the same CCD and readout electronics, some of their characteristics are listed in table 2.2. The VMC is rigidly mounted on the spacecraft in such a way that its optical axis approximately co-aligned with the spacecraft $+Z$-axis and optical axes of VIRTIS, PFS and SPICAV. This means that pointing during observations is performed by the spacecraft.

VMC performs observations of Venus from different orbital positions, that results in quite different observation possibilities, aims and techniques. After the VEX spacecraft finishes communication with the Earth on ascending branch of its orbit (fig. 2.2), VMC can start to perform global imaging of the Venusian disk. For that it takes images with the interval between them approximately equal to the interval of clouds displacement by one CCD pixel due to wind motions ($\sim$ 10 – 20 min). Then VMC can perform limb observations (at the distance

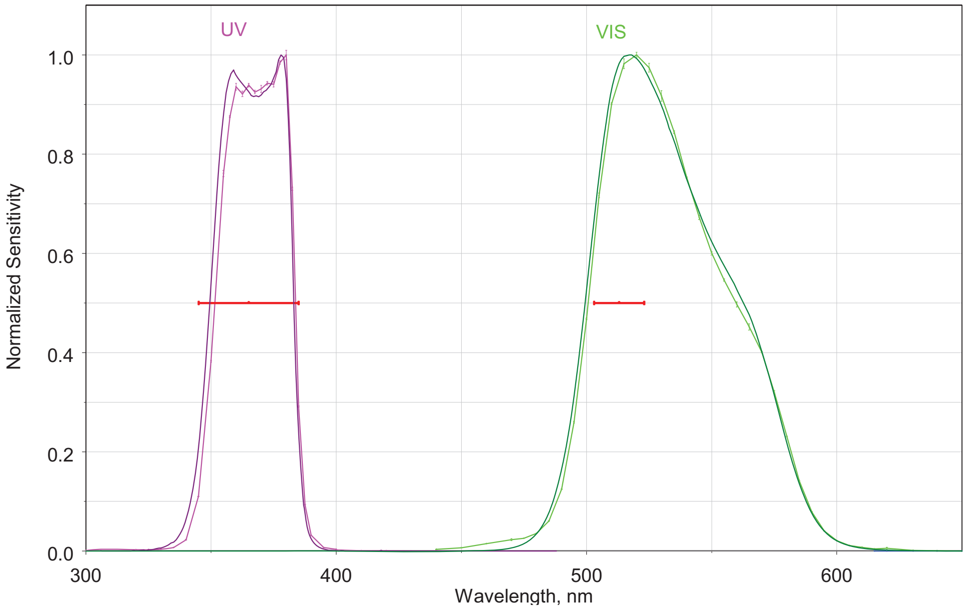

(a) UV and VIS channels.

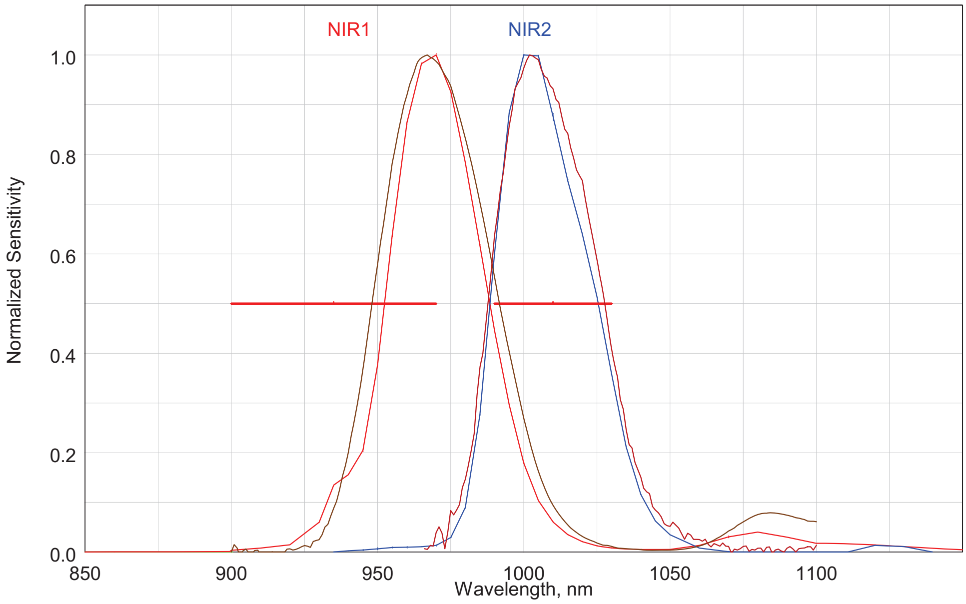

(b) NIR1 and NIR2 channels.

Figure 2.1: Normalized spectral sensitivities of the VMC channels. Bright curves with error bars — measurements at MPS; dark curves — sensitivities derived from the CCD quantum efficiency and filter transmissions provided by manufacturers; red bars — original specification.

Table 2.1: Venus Monitoring Camera optics (from Markiewicz et al. (2007)).

Total field of view	≈ 17.5° (0.3 rad)
Image scale	≈ 0.74 mrad/px
Filters	
UV	365 / 40 nm
VIS	513 / 50 nm
NIR1	965 / 40 nm
NIR2	1000 / 40 nm
F-number	UV: 7; VIS, NIR1, NIR2: 5

Table 2.2: VMC CCD detector and readout electronics (from Markiewicz et al. (2007)).

Type	Kodak KAI-1010, front illuminated, interline architecture, antiblooming
Detector size, V × H	1032 × 1024
Pixel size, µm	≈ 9.0 × 9.0
Full well	30 000 e
Gain	$\sim 5\,e$/DN
Total noise	≈ 100 e @ 37 °C
Exposure time	$N \cdot 0.504$ ms, $N = 1, 2, 3 \ldots 64449$
Sensitivity, DN/erg/s/cm^2/sr/µm/s	71.8 (UV), 11 (VIS), 0.97 (NIR1), 0.26 (NIR2)
Linearity	<1 %
Sensitivity variations	≈ 20 %

~ 2000 km) and when VEX is close to the planet near pericentre, VMC can track small cloud features. From distances 250 – 10 000 km the spatial resolution of the camera is 0.2 – 7 km/px. When the spacecraft happens to be in the planet shadow (that could happen near the pericentre, twice per Venus sidereal period), VMC can observe the night side of the planet without the stray light. This allows to map a thermal emission from the surface. These observations are limited to ~ ±40° latitude (where the spacecraft remains in the shadow, fig. 2.2b).

2.1.1.1 VMC calibration

Radiometric calibration, focus and distortion tests have been performed in a laboratory as described in *VMC calibration report* (2008). During this calibration, sensitivity of the camera at various temperatures and exposures have been determined using integrating sphere. Unfortunately, all the images in NIR2 channel with ~ 4 s and more exposures were saturated (signal level was more then 9300 DN). Thus, there is no reliable radiometric calibration for the nightside observations (30 s exposures).

During the cruise phase, the camera, which does not have a shutter, was exposed to the direct Sun illumination for more then 500 h. With the start of the observations, it was discovered that there are numerous complicated artefacts in the field of view (fig. 2.3). Because of the intensive illumination, material of micro-lenses on top of the CCD was damaged and

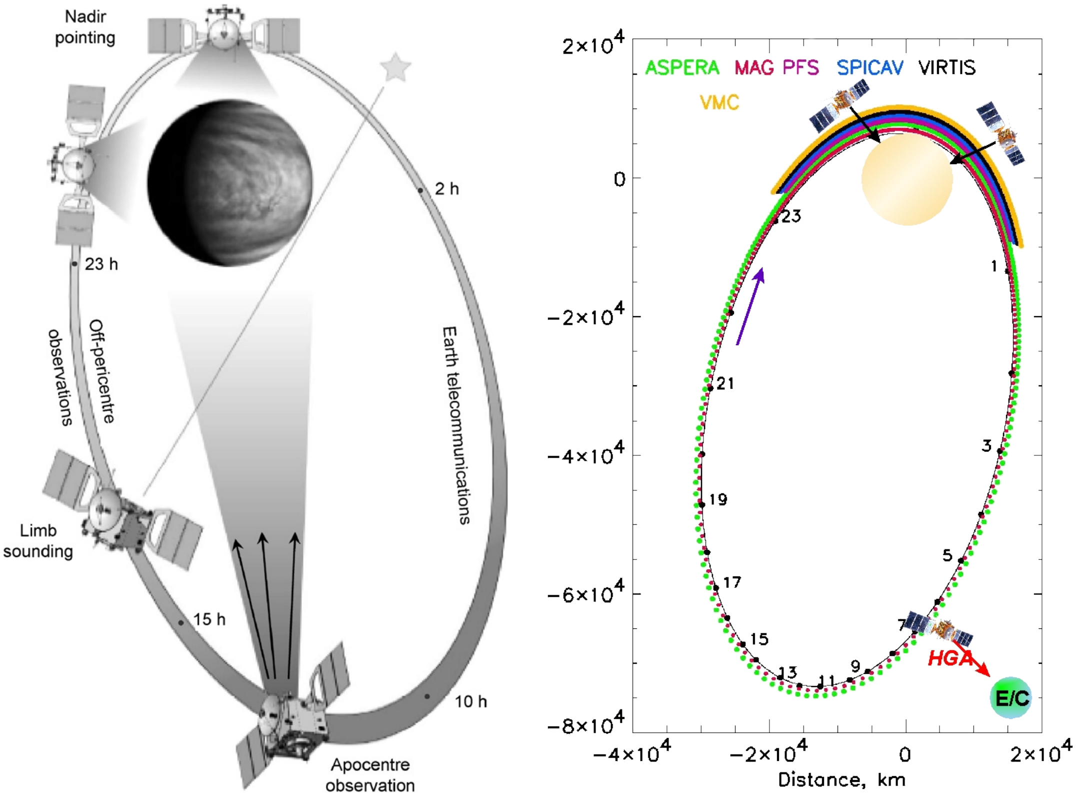

(a) Main types of observations (sketch from Markiewicz et al. (2007)).

(b) VMC nadir observations.

Figure 2.2: VEX orbit sketch.

that resulted into appearance of a dark strip in UV (fig. 2.3a), and complicated irregular dark and bright features in all channels (figs. 2.3a and 2.3b). The dark strip is believed to be caused by yellowing of the micro-lenses, and it stays at the same position. The artefacts of the other kind are not stable but evolving and moving with the time scale of several days. Additional flat-fielding is used to remove these artefacts. As a source for flat-fields, images of clouds near the north pole are used. Images, taken from close distance, are featureless. However, if the plane of VEX orbit is close to the terminator plane, large brightness gradient is present. The linear part of this gradient is removed by fitting a plane to the brightness field. Since artefacts of the second kind change not significantly during one day, it is possible to use such flat-fields. When it is not possible to take images of the cloud near the pericentre, or when these images contain features, images from another neighbour orbit are used.

In-flight recalibration of the VMC using stars has been performed by Ignatiev (Ignatiev, 2008; Titov et al., 2012) and updated in November, 2012 (Ignatiev, 2012). However, sensitivity of the NIR2 channels is not high enough to get precise enough results. Cross-calibration with VIRTIS also has been done by Ignatiev (ibid.). Unfortunately, there are no much overlapping between VMC and VIRTIS coverage. Re-calibration coefficients, obtained by these methods for NIR2 filter and 30 s exposures differ: 3.0±1.5 via stars method and 1.73±0.01 via comparison with VIRTIS-M (night-side).

Taking into account all the above, one can say that radiometric calibration of the VMC for night-side observations is rather uncertain. Because of that, this work does not rely on abso-

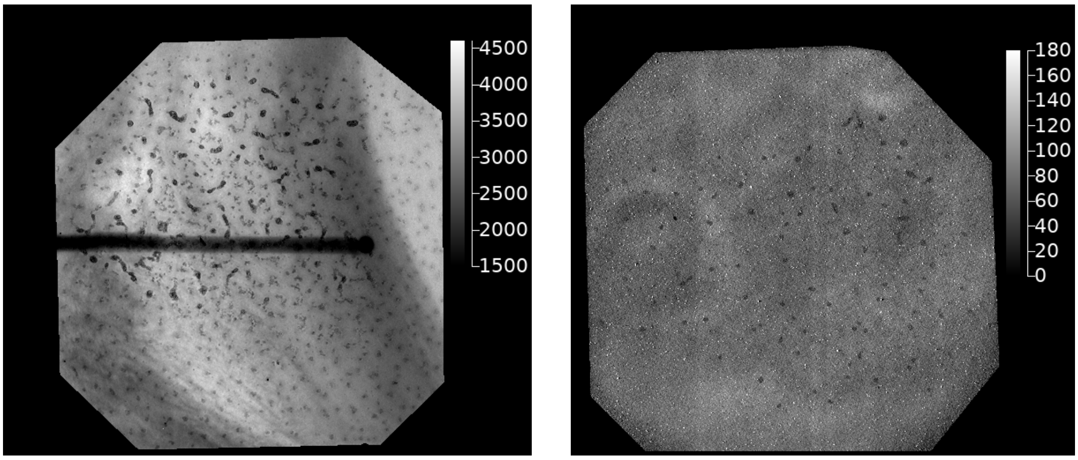

(a) Image # 44 from orbit # 2032, UV channel. (b) Image # 66 from orbit # 1376, NIR2 channel.

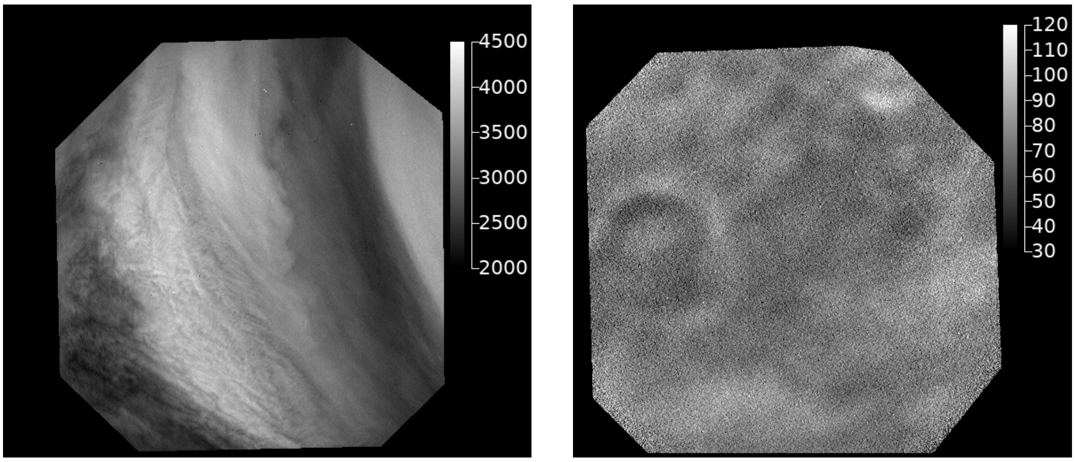

(c) Image # 44 from orbit # 2032, UV channel, additional flat field applied. (d) Image # 66 from orbit # 1376, NIR2 channel, additional flat field applied.

Figure 2.3: Examples of artefacts in VMC images.

lute calibration of the instrument, except for the time stability of the instrument response. All night-side images are taken with the same exposure of 30 s and at almost the same temperatures. This makes the calibration for night-side data self-consistent, even if it is not correct.

2.1.1.2 Data format

VMC data are delivered by Institute of Planetary Research (German Aerospace Center) as 16 bits per pixel uncompressed integer images with labels in VICAR format. Each particular image contains a quarter of the CCD frame with pixels of the given channel. Every image has dimensions of 512 by 512 pixels. Images are delivered with dark current subtracted, laboratory and additional (see section 2.1.1.1) flat fields applied. Image labels contain, *inter alia*, imaging time and radiance calibration coefficients, based on laboratory calibration.

2.1.2 Surface observations in near infra-red

The temperature on the surface of Venus is high enough ($\approx$ 740 K) to generate significant flux of thermal radiation in NIR. However, strong absorption by atmospheric gases makes impossible to detect it at any wavelength. Discovery of the transparency "windows" in in the wavelength range 1.5 – 2.5 µm by Allen and Crawford (1984), then around 1 µm (Meadows and Crisp, 1996) (see section 1.2) made possible to use regular cameras, but not radars only for imaging of the surface. The transparency "windows" are located at certain wavelengths, where gaseous absorption is much weaker (but not absent completely). This allows thermal radiation from the surface escape into the the space.

Two instruments on-board VEX are performing systematic observations of the surface: VMC (data from which are used in this work), and VIRTIS. Cameras have much smaller mass comparing to radars, that is important for spacecraft. Because of the wavelength ($\sim$ 1 µm) the properties of the thermal radiation in transparency "windows" are sensitive to the composition of the surface material. Radar emissivity is connected, of course, with dielectric permittivity of the surface, but it is much more dependent on roughness and structure on the scale of the wave length (*e.g.* Pettengill et al., 1992). Analysis of the thermal NIR data requires complicated radiative transfer (RT) modelling to account for absorption and scattering in the atmosphere. Since temperature in the the lower atmosphere changes with altitude (adiabatic lapse is -8.1 K/km), the temperature of the surface changes also. This leads to significant changes in the thermal flux from the different altitudes, because micron wavelength is at the short-wavelength shoulder of the Planckian curve. The atmosphere albedo, in upward direction, is high ($\sim$ 0.8 in NIR) and thus it reflects significant part of the thermal flux back to the surface, which, in turn, reflects it back into the atmosphere. Since the albedo a and emissivity $\varepsilon$of the surface are connected ($a + \varepsilon = 1$ if there is a equilibrium between radiation field and the surface), the process of reflections partially compensate low flux from low-emissivity regions. In the very near atmosphere significant role plays gaseous absorption. Transparency "windows" are located aside of strong absorption bands, but under high pressure and temperature, far wings of the absorption lines are strong enough to be significant for surface observations in transparency "windows". But there are neither precise enough laboratory data on CO_2 absorption at such conditions, nor theoretical models of it (Ignatiev et al., 2009, and references).

Thus, the main complications of the NIR sounding of the Venus surface are (in random order):

- unknown optical thickness of the atmosphere (at point and time of observations);
- unknown value of the gaseous absorption in the lower atmosphere;
- unknown lapse in the lower atmosphere (what we know is that none of landers has observed any signs of a haze near the surface, that suggest adiabatic lapse).

However, despite all of mentioned complications, thermal imaging is an unique tool for remote sensing of the geochemical and mineralogical properties of the Venus surface.

2.1.2.1 Surface observations with VMC

One of the VMC spectral channels is centred at 1.01 µm, that corresponds to of one of the transparency "windows". In this filter (named "NIR2") VMC is able to register thermal emission from the surface at the night-side (Baines et al., 2006; Markiewicz et al., 2007, 2008). VMC has been designed to perform observations of both day and night sides of Venus, and because of that with maximal possible exposure of 30 s signal fills only 50 – 250 DN of the 6000 DN full-well at the night side (fig. 2.4). For a region with a big difference in altitudes, like fig. 2.4a, the contrast can be as high as 150 DN in image, but most of them do not have such a big altitude variations, and thus look flatter (fig. 2.4b).

Because VMC does not have any protection from the stray-light, it can efficiently observe the nigh-side only being in the planet shadow, where neither sun light nor light from the day-side of the planet can obstruct. Thus, observations of the surface are only possible shortly (not more than 1 hour) before or after the pericentre of the orbit (fig. 2.2), that corresponds to distances up to ≈ $8.5{\times}10^3$ km. Formal spatial resolution of these images is 1 to 6 km/px, but because the surface radiation on its way to the camera passes through the dense scattering atmosphere and cloud layer, the actual spatial resolution at the surface is about 50 km (figs. 2.4 and 2.5).

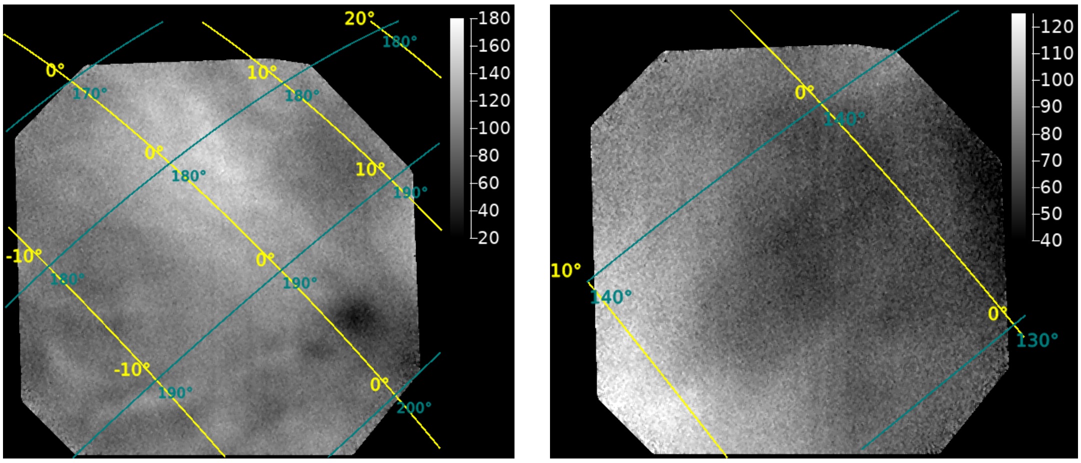

(a) High contrast image (Maat Mons).

(b) Low contrast image.

Figure 2.4: Examples of a single VMC images of the surface. Yellow colour marks parallels, teal — meridians.

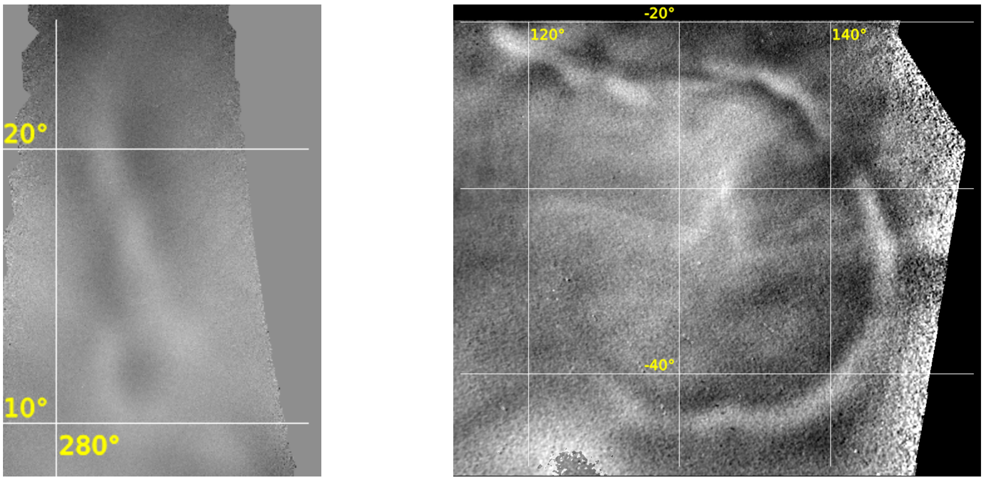

(a) Part of Devana Chasma.

(b) Artemis Corona.

Figure 2.5: Examples of surface mosaics.

Observations of the surface mostly have been performed in a so-called “nadir mode”, when

$+Z$ axis of the spacecraft (and optical axis of the camera) points to nadir. As a result, observations from each orbit produce a “stripe” of images, partially overlapping (fig. 2.6). If there is a point of an interest on the surface, it can be observed more purposefully, like, for instance, Maat Mons (fig. 2.7). Such observations not just only increase signal-to-noise ratio (SNR), but also can be used for estimations of clouds optical thickness, as it will be shown later.

There is a smearing of images caused by long exposures and spacecraft movement. The length of sub-spacecraft point track on the surface varies from $\approx$ 60 km at latitudes of about 40° to less values at low latitudes (can be $\approx$ 35 km). This value is comparable or even less than the blurring, caused by the atmosphere.

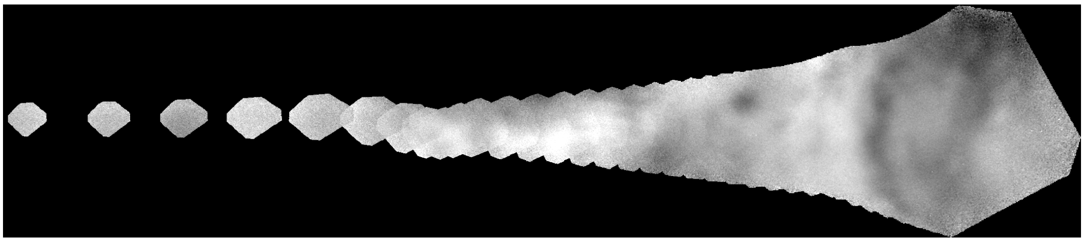

(a) Mosaic of images.

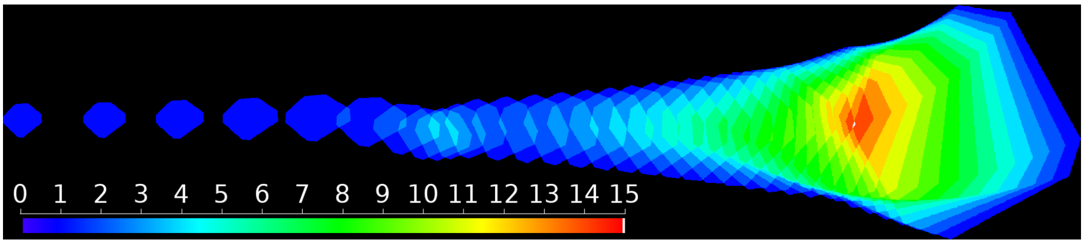

(b) Number of overlapping images.

Figure 2.6: Mosaic of surface images taken in orbit 0470. Mercator projection.

VMC acquired thousands images of the Venus night side. Significant part of the northern hemisphere is covered (fig. 2.8). Unfortunately, not all data are suitable for direct analysis because of the exceptionally thick clouds at time and place of observation, and the reasons explained in section 3.3. Recently observations strategy has changed: the camera performs observations of the same longitudes from 3 consecutive orbits (1 nadir and 2 side-looks). This will allow to do more accurate estimations of the clouds optical thickness in future.

2.1.2.2 Surface observations with VIRTIS

The VIRTIS performs observations of the surface in NIR. The southern hemisphere has been imaged by VIRTIS-M-IR (1 – 5 µm wavelengths) (Mueller et al., 2008), while in the northern hemisphere VIRTIS observation produces narrow latitudinal stripes (Arnold et al., 2008; Haus and Arnold, 2010).

VIRTIS, being a spectrometer, allows one to perform more sophisticated modelling and analysis. However, VIRTIS can not really map the northern hemisphere, where VEX is close to the planet and thus moves fast. While producing full coverage of the souther hemisphere, coverage in the northern one is very limited. This makes VMC and VIRTIS experiments much complementary.

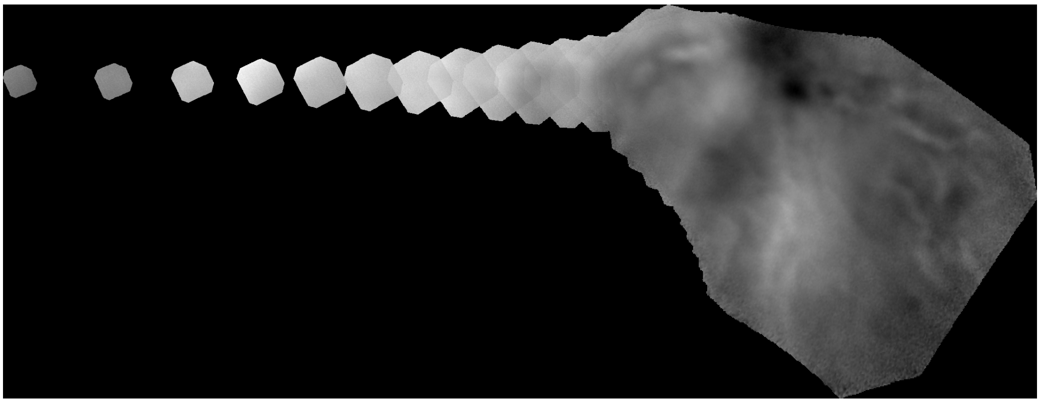

(a) Mosaic of images.

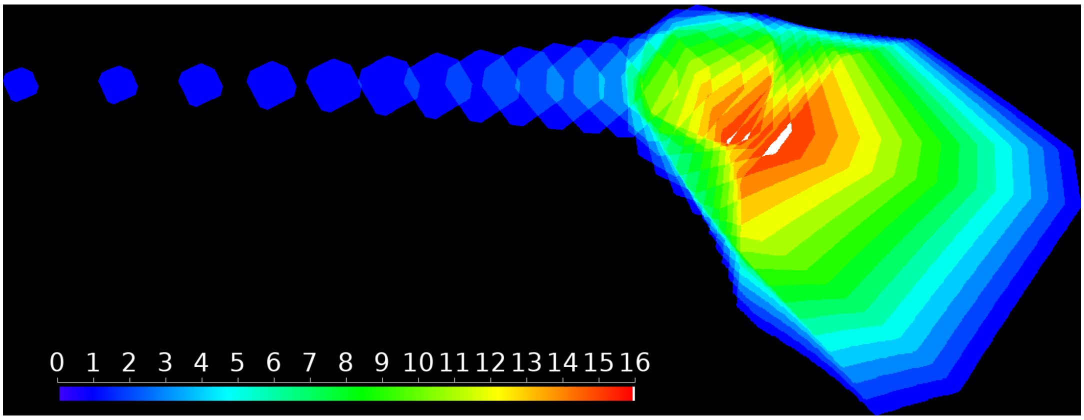

(b) Number of overlapping images.

Figure 2.7: Mosaic of surface images taken in orbit 1148. Mercator projection.

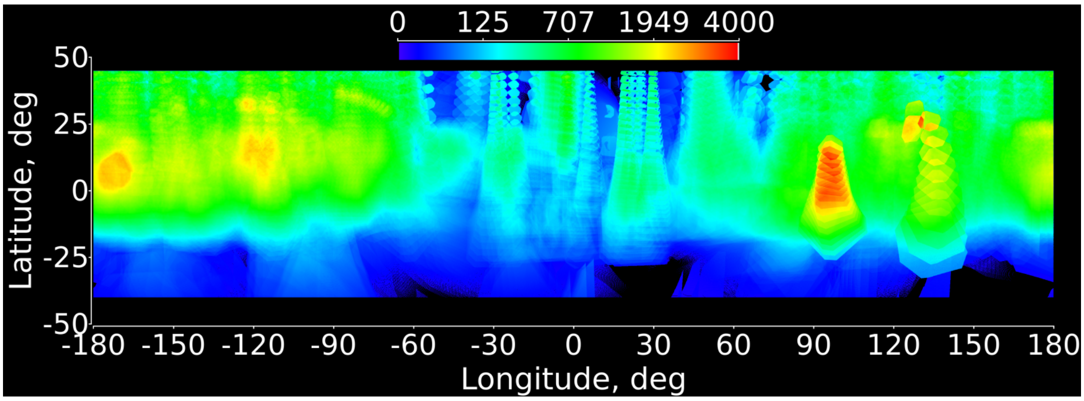

Figure 2.8: Map of surface coverage by VMC observations from orbits 0 – 2030. The map shows number of VMC pixels (non-linear scale) in 0.1° × 0.1° bins.

2.2 Magellan altimetry dataset

Many spacecraft were equipped with radars in order to study the surface of Venus. Up to now, the most full and precise coverage of the surface by radar measurements is provided by the more recent one: Magellan Venus Radar Mapping Mission (MGN) (Saunders et al., 1990).

The radar on-board MGN was operating in 3 modes: synthetic aperture mode, altimeter, and receive-only mode for measuring thermal emission. The spacecraft had high-gain antenna which was used for SAR and data downlink, and a special antenna for the altimeter. Radar was able to switch between these two antennas to perform quasi-simultaneous altimetry and SAR (fig. 2.9). During the mission SAR and altimeter have mapped ≈98 % of the surface.

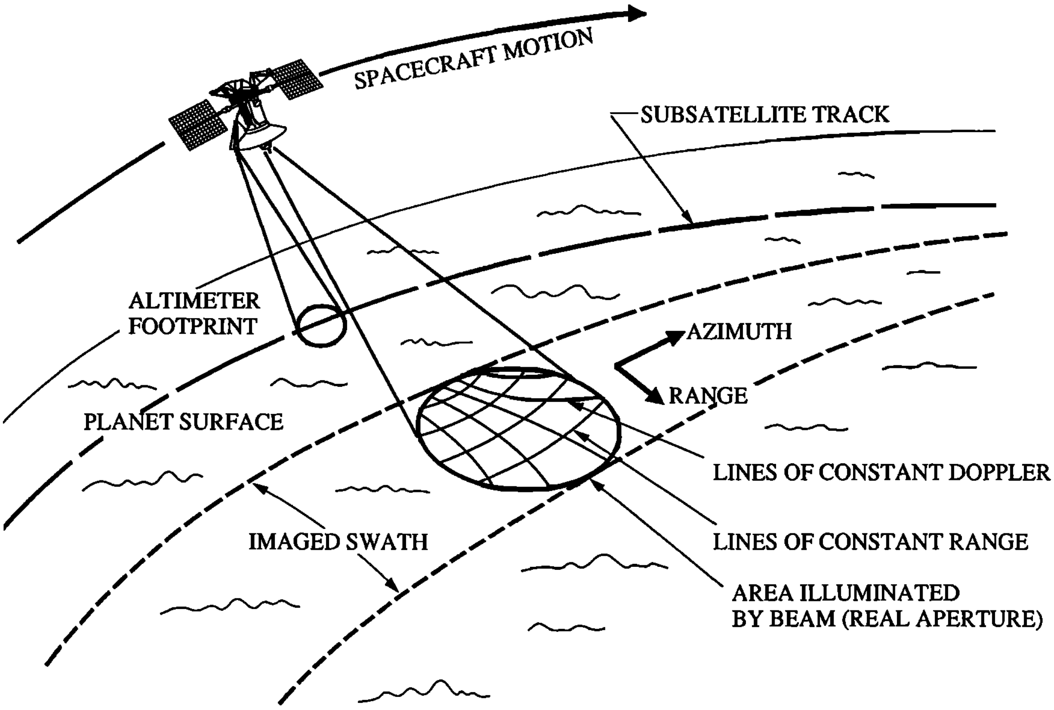

Figure 2.9: Geometry of SAR and altimetry data collection. Picture is taken from Saunders et al. (1990).

Data from the mission are available in per-obit basis as well as re-sampled into planetocentric coordinates grid. One of those re-sampled datasets, Global Topography Data Record (GTDR), is used in this work. The dataset consists of the maps of altitude in meters above 6039.999 km level in the form of 16 bit integer images in VICAR format. The images are available in Mercator or sinusoidal projections for latitudes ±66.5°, and in stereographic projection for higher latitudes. Each image covers several tens of degrees in latitude and longitude.

Because the temperature in the lower atmosphere, and thus the temperature of the surface, strongly depends on altitude, precise enough topography maps are needed for the analysis of NIR data. MGN measured topography with vertical accuracy of $\approx$ 80 m; spatial resolution of the topography maps produced by MGN varies (Ford and Pettengill, 1992), and common value is $\sim$ 4 km, while resolution of the SAR is 0.1 – 0.25 km. The spatial resolution of the Venus' surface observations in NIR is limited by atmospheric blurring with half-width of the point spread function about 50 km. Hereby the resolution of NIR observations is order of magnitude worse than the one of the MGN topography. Therefore MGN topography data are suitable for using in the analysis of NIR observations.

3 Data analysis

Emissivity is an important parameter characterizing composition and morphology of the surface. For geological analysis of the VMC images we will deduce and compare emissivity values ε of two given regions (points). To simplify matters, by "emissivity" we will mean the ratio of thermal flux from the point of the surface to the flux from a black body having the temperature of the atmosphere at given altitude:

$$\varepsilon = \frac{I}{I_P}, \tag{3.1}$$

and

$$I_P \propto \frac{2hc^2}{\lambda^5} \frac{1}{e^{\frac{hc}{\lambda kT}} - 1},$$

where h — Planck constant, T is the absolute temperature, λ is the wavelength of emitted radiation, k is the Boltzmann constant, and c is the speed of light. In case of thermodynamic equilibrium between the surface, the atmosphere, and their thermal emission, ε from eq. (3.1) is the true emissivity of the surface. Any of the descent probes and landers had not observed any hazes near the surface. Presence of the haze would be a sign of turbulence and absence of thermodynamic equilibrium. In the special case of presence of a fresh hot lava spot on the surface, there is no such an equilibrium, naturally. But since we do not want to determine emissivity of the lavas, but want just detect high flux, this is not a problem.

Brightness in the VMC night-side images depends on

1) temperature of the surface,
2) emissivity (and reflectivity) of the surface,
3) extinction and scattering in the atmosphere, and, naturally,
4) how the camera transforms illumination intensity into images.

To deduce emissivity value from the brightness, it is needed to measure or model all the other effects and quantities. It is believed that the temperature in the lower atmosphere changes only with altitude, and does not depend strongly on spatial coordinates (Seiff, 1983b). Thus, altitude maps are needed for the analysis (section 2.2). Extinction and scattering in the atmosphere can be modelled and scaled to fit observations (section 3.1). However, atmosphere parameters obtained for one region must be applicable to other points. To achieve that, optical properties of the atmosphere shall not change significantly between the given point and reference area. The most variable parameter (in both time and spatial dimensions) is the optical thickness of the clouds. The typical wind speed at the level of lower clouds (the most optically thick ones) is hundreds meters per second. Thus, one can expect that if there are no changes in the total clouds optical thickness between two consecutive VEX orbits (24 h) there are no changes on spatial scale of $\sim$ 1000 km also. Since the plane of every next VMC orbit is shifted by $\approx$ 1.5° of longitude to the previous one, the images from these orbits significantly overlap. For mosaics in the same projection the surface features are in same places and thus all contrasts on images of their ratio are due to changes in atmospheric properties. Absence of contrast means absence of clouds opacity changes from one orbit to another. However, sometimes it is needed to involve more than 2 orbits into considerations to find the one without clouds thickness variations. Figure 3.1 shows three of such ratios. They were made by transforming all 3 VMC mosaics into the same projection and dividing them one by one.

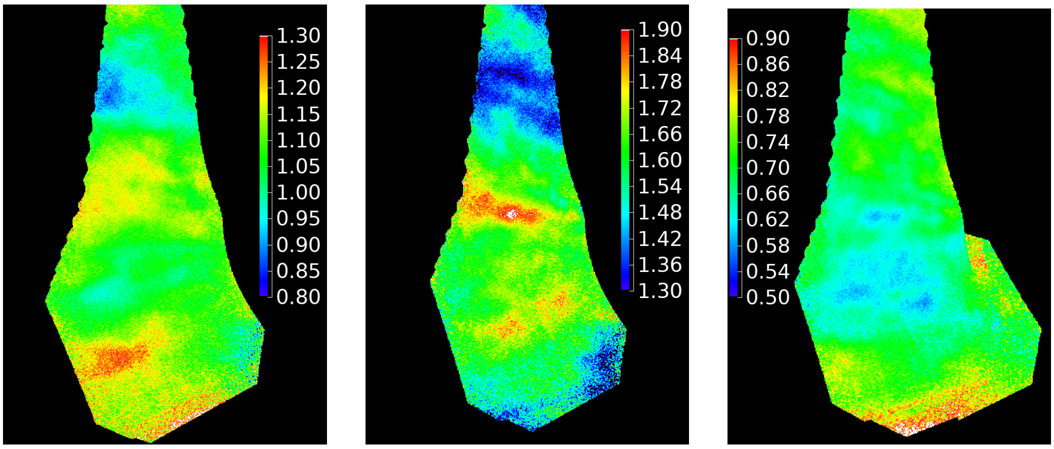

(a) Orbit #470 over #471. (b) Orbit #470 over #472. (c) Orbit #472 over #471.

Figure 3.1: Examples of mosaic ratios.

3.1 Radiative transfer in the Venus atmosphere

On its way to the camera through the atmosphere the light is affected by absorption and scattering, caused by gas (especially by the dense hot one in the very lower part of the atmosphere) and by particles in clouds and hazes (section 1.3). Absorbed energy, naturally, is emitted by the absorbers back into the system. However, temperature of cloud particles is 100 – 200 K and thus their emission at 1 µm is negligible. The temperature of gas in lower atmosphere is the same as that one of the surface. But the density of the gas is not high enough to produce a continuous spectrum. Thus, emission in transparency "windows" is weak. Scattering occurs from particles in the clouds (hazes) and from density fluctuations and molecules in gas. Both scattering processes do not change the wavelength.

In the 1-µm transparency "window" the light travels through gaseous lower atmosphere with $\tau \approx 1.3$ (Moroz, 2002), and then through the clouds with $20 \lesssim \tau \lesssim 40$ (Tomasko et al., 1985). Unfortunately, transparency "windows" are not free from absorption completely: far wings of the CO_2 and H_2O absorption bands are strong enough to be seen in the very low, dense and hot part of the atmosphere. It is extremely complicated to measure this absorption in the far wings in a laboratory. Known estimates are not accurate enough, and the amount of the absorption has to be determined from the NIR observations itself (like in *e.g.* Haus and Arnold, 2010).

In principle, it is possible to perform radiative transfer modelling for geometry of a given VMC image. Results of the modelling might be compared with the image. However, direct modelling of each VMC image is very time consuming. In addition, SNR of a single image is low (section 2.1.2.1). Thus, results of the modelling has to be compared with the VMC surface mosaics. It is not obvious, however, how to perform modelling for mosaics' geometry. As such, the following simplified model was used. As observations in nadir geometry are used, approach with point spread function can be used. Let us note, that this approach is applicable only if radiation flux on top of the atmosphere is orthotropic. One can naturally expect this from such a optically thick atmosphere[1]. This point spread function describes atmospheric blurring. Let's construct our model from the following processes: *1*) absorption in lower atmosphere; *2*) scattering in lower atmosphere; *3*) reflection (mainly from clouds) back to the surface; *4*) reflection from the surface; *5*) scattering and absorption in clouds and hazes. To model item *1* approach, that will be described in section 3.1.1, is used. To model items *2* and *5* and to get a reflection coefficient of the atmosphere for the radiation coming from the surface (item *3*) the Monte-Carlo based RT code is used (see sections 3.1.2 and 3.2). For item *4* Lambertian law is used and albedo $a = 1 - \varepsilon$ approximation is used, that is true in case of thermodynamic equilibrium between the surface and radiation field. Reflections between the surface and the atmosphere (items *3* and *4*) are modelled using two-stream approximation.

Assuming that both surface emissivity and atmospheric transmittance do not strongly vary within the scale of point spread function[2], emission intensity at a point with horizontal coordinates (x, y) at the top of the atmosphere can be expressed by the formula:

$$I(x, y) = \frac{t(x, y)\varepsilon(x, y)}{1 - (r(x, y)(1 - \varepsilon(x, y)))} \cdot \\ \cdot \iint B\left[T_S(x', y')\right] \cdot F(x - x', y - y')dx'dy' \tag{3.2}$$

where $t(x, y)$ is the atmospheric transmittance, $r(x, y)$ is the atmospheric reflectance of surface radiation in backward direction (both depend on surface altitude), $\varepsilon(x, y)$ is the emissivity distribution of Lambertian surface, $B(T_S)$ is the Planck function of the surface temperature T_S, and F is the blurring function. In this formula the two-stream approximation is applied to a single layer atmosphere to account for attenuation; convolution with the blurring function describes smoothing contrasts. We note that both atmospheric transmittance and reflectance depend on surface topography. Mueller et al. (2008) used a similar approach to analyse the VIRTIS surface images. The model surface temperature is equal to that of the atmosphere. The temperature in the lower atmosphere is assumed to have adiabatic lapse rate of ≈ 8.1 K/km (Seiff et al., 1985).

Next sections are dedicated to determination of the parameters in eq. (3.2).

3.1.1 Light absorption in Venus atmosphere

Since surface altitude variations (several km) are comparable with the atmosphere scale heigh, gaseous absorption changes significantly for landforms at different altitudes. Topography related variations of the atmospheric absorption we include in the transmittance t (eq. (3.2)). For a particular surface point we can express corrected coefficient t as $t_0 \cdot k_a e^{kH}$, where H is surface altitude.

To calculate gaseous absorption, we used approach as in Ignatiev et al. (2009) (that uses the same form-factors for line wings as in Meadows and Crisp (1996)). Radiative transfer model

---

[1] To be sure that the flux is indeed orthotropic the check has been performed and it will be discussed further

[2] The full width of the point spread function at half maximum is ~ 100 km as it will be discussed below

for these calculations is based on the DISORT code (Stamnes et al., 1988) and line parameters from the preliminary version of the carbon dioxide spectroscopic database (CDSD) for Venus, the CO_2 high-temperature database, and high-resolution transmission molecular absorption database (HITRAN). More detailed description and references are given in Ignatiev et al. (2009).

Since there is no reliable information on absorption in the far wings of CO_2 and H_2O near 1 µm under Venus conditions (high temperature and pressure) there is no possibility to do precise enough calculations of the absorption coefficient. In our case computation gave $k_a = 1.0034$, and $k = 0.0317\,\mathrm{km}^{-1}$. Emissivity, obtained with these parameters and adiabatic lapse −8.1 K/km, shows linear correlation with altitude, that does not look realistic. Therefore the value of k was adjusted to achieve absence of correlation for plains terrains ($\approx 0.12\,\mathrm{km}^{-1}$). The correlation diagram for emissivity – altitude obtained with these parameters for orbit #470 is shown in fig. 3.2. One can see that major part of points does not show correlation of emissivity with surface altitude.

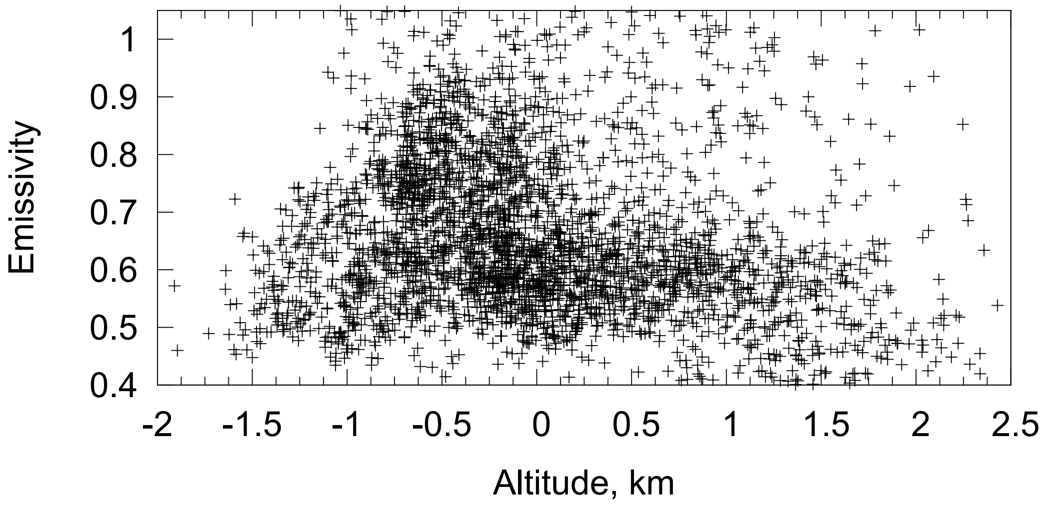

Figure 3.2: Correlation diagram (retrieved emissivity – altitude) for orbit #470. Zero altitude corresponds to the planet radius of 6051.8 km.

3.1.2 Light scattering in Venus atmosphere

As it was mentioned in section 1.3 the optical thickness of the Venus atmosphere is 20 – 40 and scattering results in intensive blurring (section 2.1.2.1). From the numerous experiments on-board descent probes and from other observations (section 1.2) it is know that cloud particles are sulfuric acid droplets (section 1.3). Their refractive index and size distribution are know quit well. All this makes possible precise modelling the scattering from these aerosols.

Naturally, there have to be time and spatial variations of clouds properties. The most significant ones take place in the lower clouds. Optical thickness of the clouds τ is much greater than 1 and therefore expected variations of τ do not change the width of the point spread function significantly. But changes of τ lead to changes in t and r (eq. (3.2) and table 3.1). Since we adjust t for account the gaseous absorption (section 3.1.1), exact value of t is not that important. But uncertainties in r are not compensated in that way. We can not retrieve τ from

Table 3.1: Dependence of r and t on τ.

τ	t	r
1	0.85	0.15
10	0.35	0.64
20	0.21	0.77
30	0.14	0.82
40	0.11	0.85

observations. Differences in the out-of-the atmosphere flux in model, described by eq. (3.2), are negligible for τ values within the range 20 – 40 (around 1 %). We select for analysis most bright VMC mosaics and therefore we assume $\tau = 20$.

We use the vertical structure of clouds and their optical properties from Tomasko et al. (1985), Henyey-Greenstein phase function with asymmetry parameter $g = 0.78$ and single scattering albedo $w_0 = 0.9995$, and optical thickness for the Rayleigh scattering in the lower atmosphere $\tau = 1.3$ from Moroz (2002). Thermal emission of the surface is a product of the Plank function that strongly depends on surface temperature and therefore on altitude, and surface emissivity ϵ defined by mineralogical composition and surface material grain size.

3.2 Model of light scattering in arbitrary atmosphere-like medium based on Monte-Carlo approach

3.2.1 Introduction

Monte-Carlo methods (Metropolis and Ulam, 1949) are a class of computational methods. They are based on implementation of some stochastic (random) process whose statistical properties are the same as of the process under study. As such, the Monte-Carlo methods can be used for modelling physical systems *ab initio*. On the other hand, the Monte-Carlo methods can be used for numerical integration. If the function is well-behaved then according to the central limit theorem accuracy of integration with n samples has $1/\sqrt{n}$ convergence. If integration is performed over a multi-dimensional space with N dimensions (degrees of freedom), number of function computation for deterministic numeric method grows as N^{th} power. Speaking about radiative transfer one can treat Monte-Carlo either as simulation method or as a method for integration of the radiative transfer equation (which has 5 dimensions in case of plane medium and more in other cases). Thus, speed of the Monte-Carlo can compete with other numerical methods for radiative transfer simulations. But, in comparison to other methods, it allows easy expansion to the domain of three-dimensional medium, where its properties change in all dimensions. This is applicable, for instance, to limb observations, to cases where relief of the surface plays significant role. Its another important quality is that Monte-Carlo code can be paralleled vary easily with very small amount (or even none) information transferred between computation nodes during its working cycle, that is important for modern computational environments.

In the next sections the Monte-Carlo based algorithm for modelling of light propagation in arbitrary atmosphere-like medium will be described. The exact meaning of the term "arbitrary" will be specified below. In general words it means that the medium might have any space configuration (*i.e.* be non plane-parallel). The algorithm will (partially) follow *ab initio* principle. As any Monte-Carlo based algorithm it extensively uses random numbers. Unless otherwise explicitly indicated, by "random" number we will mean a random real number from range $[0 : 1]$. We will use term "random" but it is obvious that for a computer-based implementation this means "pseudo random".

The section 3.2.2 will formally introduce simplifications, that are applicable to planetary atmospheres. Section 3.2.2.3 will describe some modifications to a straightforward Monte-Carlo simulations to speed up computations and establish relation between used quantities and generally used ones. In section 3.2.2.4 step-by-step scheme of the computations will be given. Since usually RT problems in atmosphere include reflection (*e.g.* from a planet surface), the section 3.2.2.5 gives description of the reflection using the same quantities as for light scattering and established their relation with the general used ones.

3.2.2 The algorithm

3.2.2.1 Applicable simplifications

Let us consider light propagation in a medium that contains small scale (comparing to the mean free path) refractive index fluctuations. In general case these fluctuations generate secondary waves and results of their interference is a new wave. Hereafter we will speak about particles in the medium, but all the following is applicable to any refractive index fluctuations.

Under some conditions the complicated process of light interaction with the matter could be described in a much simpler way. Let us assume the following.

1. Medium between particles is homogeneous.
2. Distance between particles is significantly larger than their size and the wavelength of light.
3. Particles do not have constant positions but instead of that concentration distribution by coordinates is defined.

These conditions are reasonable for a medium that is similar to a planetary atmosphere. Under such assumptions one can consider not fields but beams propagating in the medium. One can neglect interference (as it follows from conditions 1 and 2). This allows to follow the propagation of beams and moreover, only one beam at the same time (conditions 2 and 3). With these simplifications a model of light scattering in a medium could be described as follows.

3.2.2.2 Model of light scattering in rarefied medium

The model operates with the following abstractions:

particle — an individual scatterer/absorber, which is defined by single scattering albedo and a scattering matrix (see section 3.2.2.3);

medium — space filled with particles, defined by dependence of particles' concentration on coordinates and a bounding volume;

a beam of electromagnetic energy, defined by its origin, direction, and radiation state;

light source — an object that emits beams into the medium;

receiver — an object that analyses beams and might be a model of a camera or another detector.

Beam is emitted by a light source and moves in the direction of studied medium. After entering the medium, beam continues its movement until it encounters a particle. This event is determined by some probability, because we do not know particles' coordinates in advance but do know distribution of their concentration only. After that beam either scatters from the particle or is absorbed. A new beam, appeared after the scattering, moves in the medium until it encounters another particle or exits the medium bounds. Some beams that has exited from the medium might enter receiver. In the receiver an analysis of the beams is performed.

Using this scheme it is possible to model light scattering by arbitrary medium that meets the mentioned requirements using the Monte-Carlo method.

However, this scheme has a significant disadvantage. In most astronomical applications angular size of the receiver is very small or it is even a point. It means that very small or even zero part of beams that exits medium will be caught by the receiver. Therefore this scheme is useless in practical sense.

Lets try to change this algorithm in a such way that as much as possible part of beams (and as soon as possible, because every scattering act "costs" computational resources) falls into the receiver. It is obvious that in case of point receiver it is possible to increase amount of beams that falls into it *only* by directing beams into the receiver intentionally because probability of random fall is equal to zero. To increase speed of accumulation of scattered energy in a receiver we will modify scheme of light scattering on a particle.

3.2.2.3 Light scattering on particles

The process of beam's scattering on a particle can be modelled in the two ways[3]: 1) the incident beam scatters in all directions and intensity of scattered radiation depends on direction as defined by particle's phase function; 2) the incident beam scatters in random direction and its energy does not change while probability density distribution on directions is defined by the same phase function. Transformation of parameters of incidence radiation into parameters of scattered radiation could be described by scattering matrix and single scattered albedo (*e.g.* van de Hulst, 1981). Consider this process in more details. Let $\mathbf{E}_0$ — energy that falls on the particle, $\mathbf{E}$ — energy of scattered beam, $\mathbf{X}$ – scattering matrix. Then:

$$\mathbf{E} = \eta \mathbf{X} \times \mathbf{E}_0 \tag{3.3}$$

where η – norming coefficient which depends on used scattering algorithm. Normalization condition for $\mathbf{X}$ we will write as follows:

$$\int\limits_{4\pi} \left|\mathbf{X} \times \mathbf{E}_0\right| \frac{d\Omega}{4\pi} = \left|\mathbf{E_0}\right| \tag{3.4}$$

in order to make

$$\chi = \frac{\left|\mathbf{X} \times \mathbf{E_0}\right|}{\left|\mathbf{E}_0\right|} \tag{3.5}$$

particle's phase function. Factor η is equal to 1 in case of homogeneous (by directions) distribution of scattered beams or to $1/\chi$ if distribution by directions is defined by particle's phase function.

Consider algorithm where distribution of beams by directions is inhomogeneous. In this case $\eta = 1/\chi$ and

$$\mathbf{E} = \frac{1}{\chi} \mathbf{X} \times \mathbf{E}_0.$$

---

[3] Equality of these methods will be shown below in this section.

From normalization condition for **X** (eq. (3.4)) one can derive:

$$|\mathbf{E}| = \left|\frac{1}{\chi}\mathbf{X}\times\mathbf{E}_0\right| = \frac{|\mathbf{E}_0|}{|\mathbf{X}\times\mathbf{E}_0|}\times|\mathbf{X}\times\mathbf{E}_0| = |\mathbf{E}_0|\,.$$

Thus energies of incident and scattered beams are equal.

Modified scattering algorithm Now we will change the algorithm to increase amount of energy that falls into the receiver. After the each scattering a new special beam will be directed straight to the receiver. Let Ω — solid angle subtended by the receiver, $\mathbf{E}_0$ — energy of incident radiation, $\mathbf{E}$ — energy of radiation scattered in random direction, and $\mathbf{E}_\Omega$ — energy of the beam that goes into solid angle Ω (*i.e.* to the receiver).

$$|\mathbf{E}_\Omega| = \int\limits_{\Omega} |\mathbf{X}\times\mathbf{E}_0|\frac{d\Omega}{4\pi} = |\mathbf{E}_0|\int\limits_{\Omega}\chi\frac{d\Omega}{4\pi}.$$

From the energy conservation law:

$$|\mathbf{E}| + |\mathbf{E}_\Omega| = \int\limits_{4\pi} |\mathbf{X}\times\mathbf{E}_0|\frac{d\Omega}{4\pi} = |\mathbf{E}_0|\int\limits_{4\pi}\chi\frac{d\Omega}{4\pi} = |\mathbf{E}_0|\,.$$

Now suppose that $\Omega \to 0$. Then:

$$|\mathbf{E}_\Omega| = |\mathbf{X}\times\mathbf{E}_0|\frac{\Omega}{4\pi} = \chi\,|\mathbf{E}_0|\,\frac{\Omega}{4\pi} \tag{3.6}$$

$$|\mathbf{E}| = \int\limits_{4\pi} |\mathbf{X}\times\mathbf{E}_0|\frac{d\Omega}{4\pi} = |\mathbf{E}_0|\,.$$

As the energy is converted during scattering as $\mathbf{E} = \eta\mathbf{X}\times\mathbf{E}_0$, then to meet condition of eq. (3.6) the following has to be valid:

$$\mathbf{E}_\Omega = \mathbf{X}\times\mathbf{E}_0\cdot\frac{\Omega}{4\pi} = \mathbf{M}_\Omega\times\mathbf{E}_0 \tag{3.7}$$

To get rid of Ω, lets calculate albedo of the observed area. Suppose that N beams fall on area S. After scattering part of them goes into solid angle Ω. Their averaged energy is equal to E. Intensity of falling light

$$\mathbf{I}_0 = \frac{N\mathbf{E}_0}{S\cos i}.$$

Brightness **B** of the same area is

$$\mathbf{B} = \frac{N\mathbf{E}}{\Omega S\cos\varepsilon}.$$

In scalar case albedo of the area:

$$A = \frac{\pi}{\Omega}\cdot\frac{E}{NE_0}\cdot\frac{\cos i}{\cos\varepsilon}.$$

In vector case

$$\mathbf{B} = \frac{\mathbf{A}}{\pi}\cdot\mathbf{I}_0.$$

Thus:

$$\frac{N\mathbf{E}}{\Omega S\cos\varepsilon} = \frac{\mathbf{A}}{\pi}\cdot\frac{N\mathbf{E}_0}{S\cos i},$$

or cancelling N:

$$\frac{\mathbf{E}}{\Omega\cos\varepsilon} = \frac{\mathbf{A}}{\pi}\cdot\frac{\mathbf{E}_0}{\cos i}.$$

Let us introduce

$$k = \frac{\Omega\cos\varepsilon}{\pi\cos i}.$$

Then:

$$\mathbf{E} = k\mathbf{A}\mathbf{E}_0.$$

Now unwind the summations:

$$\frac{\sum\mathbf{E}_i}{N} = k\mathbf{A}\mathbf{E}_0$$

$$\mathbf{E}_i = k\mathbf{A}_i\times\mathbf{E}_0$$

$$\frac{\sum\mathbf{E}_i}{N} = \frac{k\sum\mathbf{A}_i\times\mathbf{E}_0}{N}$$

$$\mathbf{A} = \sum\frac{\mathbf{A}_i}{N}.$$

As a result of the modelling we will get a matrix $\mathbf{M}$, that connects incident and scattered beams: $\mathbf{E} = \mathbf{M}\times\mathbf{E}_0$. It is clear that

$$\mathbf{M} = k\mathbf{A}.$$

If so, then albedo

$$\mathbf{A} = \mathbf{M}/k.$$

Therefore, for calculations of albedo, matrix $\mathbf{M}_\Omega$ shall be divided by k. As Ω during that will be cancelled, then for receiver of infinitely small size result does not depend on Ω, and $\mathbf{M}_\Omega/\Omega$ can be used as a result. It might have sense to simulate panoramic receivers. Panoramic receiver might be constructed from a number of point receivers, which is similar to a panoramic CCD detector. Obviously as far as the receiver does occupy negligible part of the sphere (its size $\ll 4\pi$) all above said is applicable to the each cell of the receiver.

Particle's optical properties can be defined as dependence of scattering matrix $\mathbf{X}$ on scattering angle θ and azimuthal angle φ:

$$\mathbf{X} = \mathbf{X}(\theta, \varphi). \tag{3.8}$$

In this case beams in the model should carry information about radiation state. Thus, if scattering matrix would be similar to the Jones matrix this information is the Jones vector, if scattering matrix would be similar to the Müller matrix — it is the Stokes vector. Lets find relation between matrix $\mathbf{X}$ and, for example, Müller matrix $\mathbf{F}$. To do that assume that scattered beams distributed homogeneously by all directions. Then:

$$\mathbf{J} = \mathbf{F}\times\mathbf{I},$$

where $\mathbf{J}$ — power of light of scattered radiation and $\mathbf{I}$ — intensity of the incident one.

$$\mathbf{I} = \frac{N\mathbf{E}_0}{\sigma},$$

where

$$\sigma = \int\limits_{4\pi} \frac{|\mathbf{F} \times \mathbf{I}|}{|\mathbf{I}|} d\Omega,$$

and N — number of incident beams. From the energy conservation law:

$$\int\limits_{4\pi} \mathbf{J} d\Omega = \sum \mathbf{E}_i = \sum \mathbf{X}_i \times \mathbf{E}_0.$$

Now substitute integral by a sum:

$$\sum \mathbf{J}_i \Delta\Omega_i = \sum \mathbf{X}_i \times \mathbf{E}_0.$$

Since beams are distributed by directions homogeneously, $\Delta\Omega_i = 4\pi/N$. Energy per beam: $\mathbf{E}_i = \mathbf{J}_i \Delta\Omega_i$. Avoiding index i we can write:

$$\mathbf{X} \times \mathbf{E}_0 = \mathbf{J} \frac{4\pi}{N}$$

$$\mathbf{X} \times \mathbf{E}_0 = \mathbf{F} \times \frac{N\mathbf{E}_0}{\sigma} \frac{4\pi}{N},$$

and, consequentially:

$$\mathbf{X} = \frac{4\pi}{\sigma} \mathbf{F}.$$

3.2.2.4 Computation steps

On the basis of above said the working algorithm of the model (which is used in the computations) can be written as follows.

1. A light source emits the beam.
2. The beam enters the medium which is filled by particles.
3. Distribution of extinction coefficient along beam's trajectory is computed.
4. Random point of scattering is determined from extinction coefficient distribution along the beam line.
5. If there are particles of different kind at the scattering point, then random kind of scattering particle is selected.
6. According to the particle's single scattering albedo and random number decision is made whether this beam is absorbed or it will be scattered. If it is absorbed, we finish tracing of this beam.
7. Beam scatters from particle in the direction of receiver and scattered beam caught by the last one.
8. Beam scatters from particle in random direction. Then we continue from the step 3 with the new beam.

Consider these steps in more details.

The beam enters the medium The medium is not infinite. Let us introduce a bounding volume. Assume concentration of particle to be zero outside of this volume.

Computation of extinction coefficient distribution along beam trajectory For that one has to determine extinction probability distribution of the beams along their trajectory. Probability in each unit volume is determined by extinction cross-section of particles in that volume (we assume that medium itself is homogeneous and thus does not scatter light). Consider a pipe inside of which the beam propagates. It is clear that extinction probability at some small part of the pipe is proportional to ratio of total extinction cross-section of particles in this small volume to cross-section of the pipe. Integrating this probability by beam's trajectory we get the needed distribution.

Determination of a scattering point Knowing the distribution of extinction coefficient along the path from previous step, one can get a random number described by this distribution and, thus, determine the coordinates of the scattering point.

Determination of a scattering particle There might be particles of different types in the medium. Each class of particles has their concentration distribution by coordinates. Determining the concentration of particles (and thus extinction coefficient) of each class in a given point in space one can randomly choose one of the classes.

Scattering of a beam on a particle Scattering of a beam from a particle is described by two parameters: single scattering albedo and scattering matrix.

Scattering of a beam into the receiver Beam is forced to scatter in the direction of the receiver. We assume that this beam carries zero energy, but produces non-zero illumination. It means that intensity of this beam (for receiver) has to be non-zero. It shall be proportional to probability of scattering in direction of the receiver for the beam (*i.e.* integral of the phase function over receiver aperture). It shall be proportional to the probability of the beam to reach the receiver without subsequent absorption or scattering (*i.e.* leave bounding body without absorption/scattering inside).

Scattering of a beam in random direction Direction of scattered beam is determined by particle's phase function in the following way. By integration of the scattering matrix (eq. (3.8)) and vector that determines incident radiation state (Stokes or Jones vector) that falls on particle by θ and by φ one can obtain of scattering probability density distribution by directions for the given beam. Using this distribution one can determine random direction of scattered beam.

3.2.2.5 Reflecting surfaces

It is needed to discuss reflecting surfaces separately. Since usual description of reflection differs from the description of scattering, this means that the model have to deal with two different processes. We would like to avoid this, therefore let's write the laws of reflection in terms of particles and their phase functions. In order to do that we represent a surface composed of particles packed so tightly that beams can not penetrate deeper than the first (surface) layer of particles. Therefore they always scatter from the particles at the boundary surface. We will introduce a function that will play role of the phase function for these reflecting particles.

Let I_0 — radiation that falls onto the surface at angle i and reflects at angle ε. If actual reflection law depends not (only) on i and ε, the following can be changed accordantly. Then brightness of the surface S will be:

$$B\cos\varepsilon S = \frac{1}{\pi} A I_0 \cos i S.$$

Using vectors one can write:

$$\mathbf{B} = \frac{1}{\pi}\mathbf{A}\mathbf{I}_0,$$

where **B** — brightness and **A** is albedo (**A** depends on i and ε). The plane albedo of the surface will be:

$$A_p = \frac{\int_{2\pi} A I_0 \cos\varepsilon d\Omega}{\pi\cos i I_0}.$$

This quantity is the same as single scattering albedo for a particle. And now it is easy to see that

$$\frac{\left|\mathbf{A}\mathbf{I}_0\right|\cos\varepsilon}{A_p\pi\cos i\left|I_0\right|}$$

suits normalization condition for particle phase function (eq. (3.4)). Because $I_0 \neq 0$ we can simplify this expression to

$$\frac{\mathbf{A}\cos\varepsilon}{A_p\pi\cos i}. \tag{3.9}$$

Thus, eq. (3.9) allows one to transform reflection law $\mathbf{A} = \mathbf{A}(i,\varepsilon)$ into artificial particle with the *ad hoc* phase function. Layer of such particles will produce the same reflection as the original $\mathbf{A}(i,\varepsilon)$.

3.2.2.6 Absorption and emission in medium

A matter inside medium might emit light either because it absorbs light or by other reason. Since we deal only with far fields (section 3.2.2), interference between the fallen and emitted beams can be neglected. As such, emission might be performed independently from absorption. Thus we can add light sources to the medium which will be “charged” by absorption.

3.2.2.7 Light receiver

Receiver object in the model analyses incoming beams and can store or handle somewhere extracted information. This information may include:

- direction of the beam;
- intensity of the beam;
- polarization state of the light;
- total scattering matrix;
- scattering history of the beam.

3.2.3 Conclusions

The described algorithm was implemented as the computer code. The multi-threaded C++ code allows to compute the light propagation in an arbitrary atmosphere-like medium. Some additional optimizations were implemented for one-dimensional atmosphere (*i.e.* where properties of the atmosphere change only along one direction) and for atmosphere with a shape of a spherical shell. As a result of computations one can obtain flux at a number of specified points.

3.3 VMC pointing problem

During the work with VMC surface images it was found that pointing information for VMC images is not accurate enough. It leads to a certain misalignments in limb images (several VMC pixels) and significant misalignments in the surface images. It seems that pointing error increases near pericentre of the VEX orbit, and for a typical surface image the error is about hundred of kilometres on the surface. Numerous attempts have been made to find the true cause of the problem involving colleagues at DLR and ESOC. None of them succeeded[4].

Misalignment is different for every consequent image in orbit and thus it is impossible to fix the problem by affine transformation of the mosaic. But we found that by applying a shift (constant for all images in an orbit) to the imaging time one can fix misalignments between VMC and MGN data. Details of the problem and the workaround are presented in appendix A. However, this workaround can be applied only to orbits, where we can see a sharp contrast enough details, *e.g.* mountains. This significantly reduces the amount of data available for quantitative analysis.

3.4 Calculation of the surface emissivity maps

To obtain maps of the surface emissivity the VMC observations must be compared to the model images. Due to unknown cloud opacity and uncertainties in the VMC radiometric calibration (section 2.1.1.1) we normalized the images by the value at a reference location(s), where the surface was assumed to be of basaltic composition.

The Monte Carlo radiative transfer simulations (section 3.2) were used to determine the atmospheric blurring function, atmosphere transmittance and reflectance. The modelling gave the blurring function $F(x, y)$ with half-width of $\approx$ 50 km, which is in agreement with both apparent blurring of VMC images and previous results obtained by Hashimoto and Imamura (2001) (fig. 3.3). The difference between our blurring functions and the one from Hashimoto and Imamura (2001) could be caused by using the different phase function of atmospheric particles and different cloud models. Values of atmospheric reflectance r and transmittance t for selected atmosphere model (obtained from same simulations) are $r = 0.77$ and $t = 0.21$, for zero surface altitude. Also these calculations were used to check if outgoing flux on the top of the atmosphere is orthotropic, because eq. (3.2) is valid only in that case.

---

[4] When writing of this thesis was almost finished, it was found that during image processing, DLR's program writes the moment of shutter opening (*i.e.* the *start* of the exposure) into the VMC image headers as *imaging time*, that in fact moves time stamp of the image by half of the exposure time, *i.e.* by 15 s for the surface observations, into the past. This explains pointing errors (at least partially), and our guess of the error main source was correct.

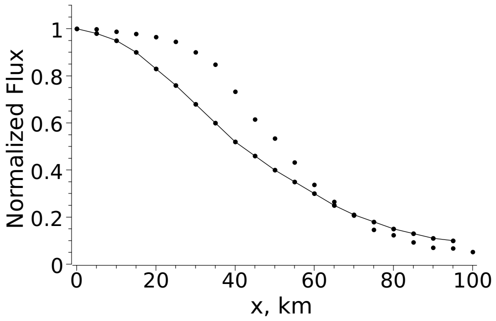

Figure 3.3: Blurring functions from our model (dots) and Hashimoto and Imamura (2001) (dots with line).

To calculate synthetic VMC images we used the Magellan topography derived from Magellan Radar Altimeter (Ford and Pettengill, 1992). The topography data were converted into the maps of temperature and surface brightness distribution assuming thermal equilibrium with the atmosphere, constant lapse rate of −8.1 K/km (Seiff et al., 1985) and constant emissivity (exact emissivity value does not matter because of further normalization). Then synthetic VMC images were obtained by convolving the surface brightness distribution with the blurring function (eq. (3.2) and fig. 3.3).

In order to get rid of uncertainties in the VMC absolute calibration and cloud opacity, we normalized the measured images dividing them by the brightness at a reference location individually selected for each mosaic. From eq. (3.2) we can derive the following expression for the VMC normalized image V:

$$V(x,y) = \frac{t(x,y)\varepsilon(x,y)\left[1 - r(1-\varepsilon_0)\right]}{t(x_0,y_0)\varepsilon_0\left[1 - r(1-\varepsilon(x,y))\right]} \cdot \\ \cdot \frac{\iint B\left[T_s(x',y')\right] \cdot F(x-x',y-y')\,dx'dy'}{\iint B\left[T_s(x',y')\right] \cdot F(x_0-x',y_0-y')\,dx'dy'} \tag{3.10}$$

where ε_0 is the assumed surface emissivity at the reference location (x_0, y_0).

In addition, we considered a model case with constant surface emissivity. The expression for normalized model image is derived in a similar way:

$$M(x,y) = \frac{t(x,y)}{t(x_0,y_0)} \cdot \\ \cdot \frac{\iint B\left[T_s(x',y')\right] \cdot F(x-x',y-y')\,dx'dy'}{\iint B\left[T_s(x',y')\right] \cdot F(x_0-x',y_0-y')\,dx'dy'} \tag{3.11}$$

All contrasts in the model image are due to temperature differences and not emissivity variations. From eqs. (3.10) and (3.11) we derive the following expression for the unknown surface emissivity distribution:

$$\varepsilon(x,y) = \frac{R(x,y)\varepsilon_0(1-r(x,y))}{1 + r(x,y)\left[\varepsilon_0(1-R(x,y)) - 1\right]} \tag{3.12}$$

where

$$R(x,y) = \frac{V(x,y)}{M(x,y)}.$$

Thus eq. (3.12) allows us to derive spatial distribution of the surface emissivity from the ratio of the normalized VMC and model images and assumed emissivity ε_0 at a reference location. We make two remarks on eq. (3.12). First, it is applicable only to emissivity variations of spatial scale greater than the full width of the blurring function (≈ 100 km, or ≈ 10 VMC pixels), which holds for large-scale surface features. Second, the distance between the reference site and the place where we determine emissivity should not exceed typical scale of deep cloud inhomogeneities (~ 1000 km). Both conditions are met in the areas analysed in this work.

3.5 Data processing pipeline

Previous sections gave detailed description of the data processing steps. To summarize and to collect this spare information, a list of all data processing steps is given below. List items contain brief description of the step and a reference to a section with detailed information when applicable.

1. For an area of interest, VMC orbits without strong cloud opacity variations are selected (section 2.1.2.1). A single orbit is considered in the further steps.
2. VMC images are transformed from DNs into absolute brightness units.
3. Mosaic (in Mercator projection) is made from individual VMC images.
4. For the region, covered by VMC mosaic, an MGN topography mosaic in the same projection as VMC mosaic is made.
5. MGN topography mosaic is transformed into map of brightness as described above (section 3.4), assuming constant surface emissivity.
6. VMC and MGN-based mosaics are compared. Comparison is performed using a blink comparator. If at this step mosaics do not match each other (section 3.3), then imaging time of individual VMC images is adjusted and steps 3 – 6 repeat.
7. Several reference locations, where surface is supposed to be of basaltic composition, are selected.
8. Equation (3.12) is applied to the mosaics and the map of emissivity is made (section 3.4).
9. The emissivity map is transformed into a required projection for geological investigation.

3.6 Summary

In this chapter we gave a description of algorithms and methods that have been developed to obtain maps of certain characteristic of the Venus surface. This characteristic is called “emissivity” here and means ratio of the brightness of the surface at 1 µm wavelength to the brightness of the black body with the temperature of the atmosphere at the given level. This quantity is connected with physical properties of the very thin (with the order of few µm) surface layer as well as with the temperature of the surface. Physical properties of the surface are, in turn, connected with the mineralogy of the surface while significant increase in the temperature might mean presence of a hot lava on the surface.

These algorithm, being implemented in computer programs, allowed us to obtain maps of surface emissivity from VMC images for a certain areas of Venus. These maps were used to perform geological analysis of these areas and to look for a ongoing volcanic activity, which are the subject of the next chapters.

4 The geologic analysis of the VMC data

4.1 Introduction

The major objective that is pursued by this study is to test, if tessera terrain material is different in its chemical/mineralogical composition from the surrounding plains, which as was said above are considered to be basaltic (section 1.4). We approached this objective not globally but within rather small region which has the appropriate objects of the study and is well covered by the VMC images.

4.2 Study areas

This is the area South-West (SW) of Beta Regio (fig. 4.1). Here there is a relatively small but distinct massif of tessera terrain, Chimon-mana Tessera, the surface emissivity of which we try to determine and compare with that of the adjacent plains. About 1000 km to the north, among the plains, there is a relatively small volcano, Tuulikki Mons, whose morphology (gentle slopes and extended outskirts of lava flows) are indicative of basaltic composition (*e.g.* Head et al., 1992). Its presence in the study area is important for our analysis because its summit stands about 0.5 – 1 km above the plains, as the summit portion of Chimon-mana tessera does. Thus, we can eliminate the altitude effect and try to search for the effects of surface composition or texture.

Quantitative emissivity measurements presented in section 4.3 below are obtained using orbit-wise mosaics, built from individual images taken in orbit 470 (fig. 4.2), obtained on 2007-08-04. From eq. (3.12) and ratios of mosaic for orbit 470 to orbits 46x and 47x we estimate clouds opacity variations across studying area to be not more than 10 % and likely smaller. This gives errors in emissivity 10 – 20 % (assuming that all other parameters in eq. (3.12) are constant).

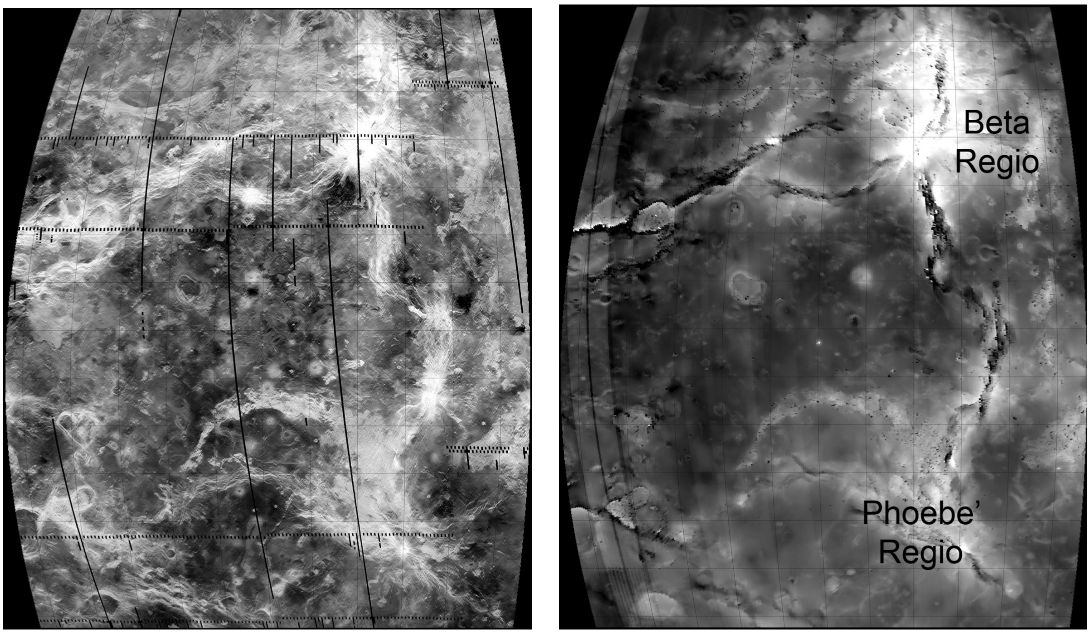

(a) MGN SAR image.

(b) MGN topographic map (highs are bright).

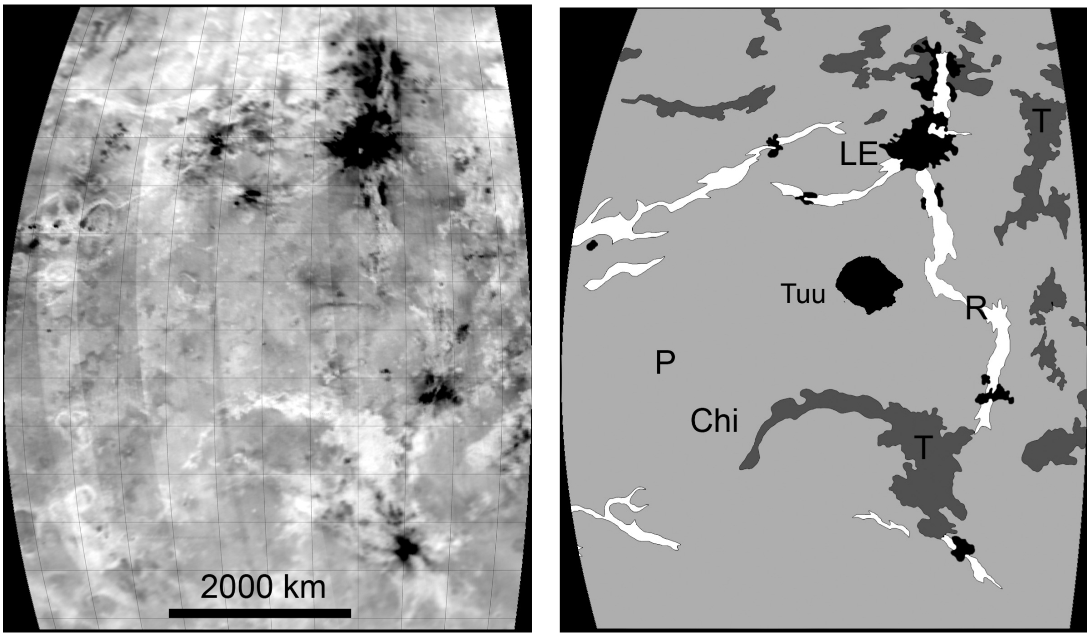

(c) MGN map of microwave emissivity (brighter shades denote higher emissivity).

(d) simplified geologic map of the area: P — plains, T — tessera terrain, R — rifts, black spots — young lavas, LE — low radar emissivity deposits, Chi — Chimon-mana Tessera, Tuu — Tuulikki volcano.

Figure 4.1: Maps of the study area SW of Beta Regio.

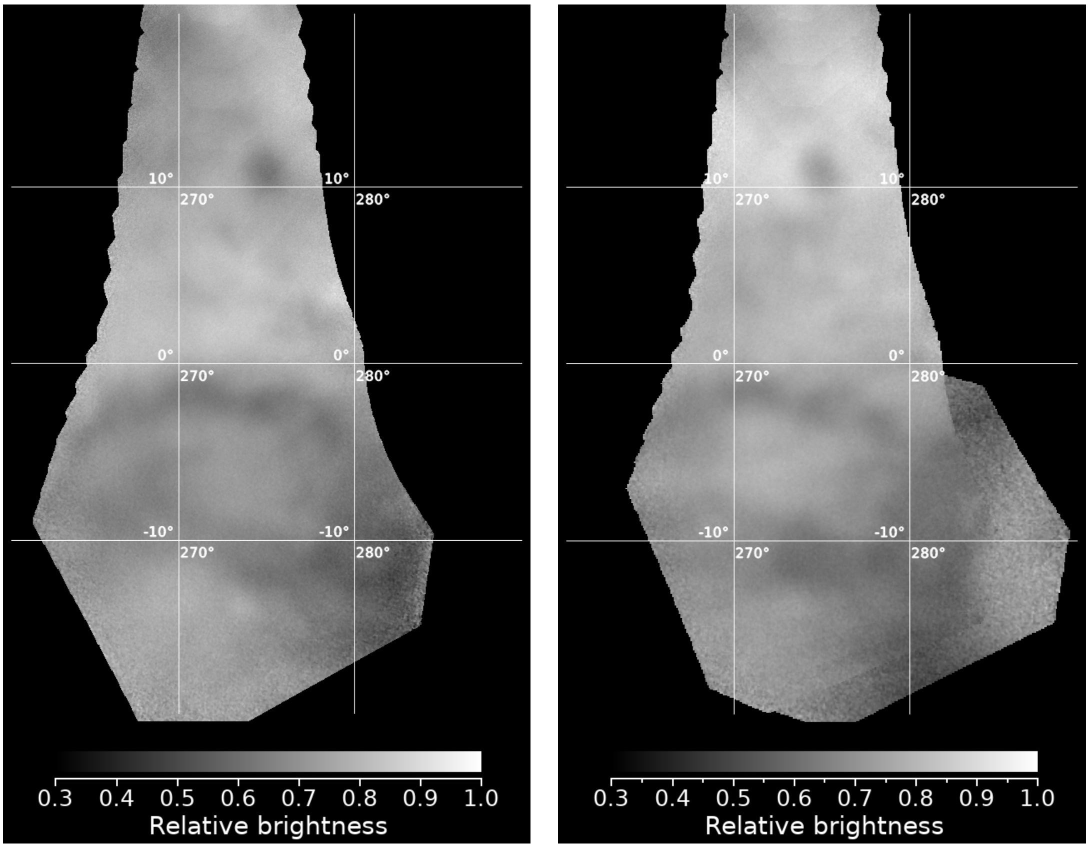

(a) Orbit # 470.

(b) Orbit # 471.

Figure 4.2: VMC mosaics of study area.

4.3 Search for compositional difference among the studied units

We compare (fig. 4.3) the central part of Chimon-mana Tessera (unit 1) against surrounding regional plains (unit 2), divided into subunit 2n (northern plains) and 2s (southern plains), and relatively young Tuulikki Mons volcano (unit 3) and its summit part (unit 4) against its surrounding regional plains (unit 5). The unit altitudes are given in table 4.1.

As it was said above, calculation of 1-µm emissivity ε from the observed thermal emission requires two assumed model parameters: temperature lapse rate L and reference surface emissivity ε_0. For each pixel we calculated ε for 2 values of the reference emissivity $\varepsilon_0 = 0.8$ and $\varepsilon_0 = 0.58$. The values $L = -8.1$ K/km and $\varepsilon_0 = 0.8$ have been used in a number of previous publications (*e.g.* Meadows and Crisp, 1996), while $\varepsilon_0 = 0.58$ have been used by Smrekar et al. (2010).

Before discussing the calculation results, it is worthwhile to consider effects of different assumptions. The decrease of the assumed reference surface emissivity ε_0 from 0.8 to 0.58 should "proportionally" reduce calculated emissivity of all terrains. The decrease of the assumed lapse rate (for example from -8 K/km to -5 K/km) leads to a hotter model temperature of the high-standing landforms and thus to a higher 1-µm model emission, which in turn leads to lower emissivity of the high-standing landforms calculated from the comparison of

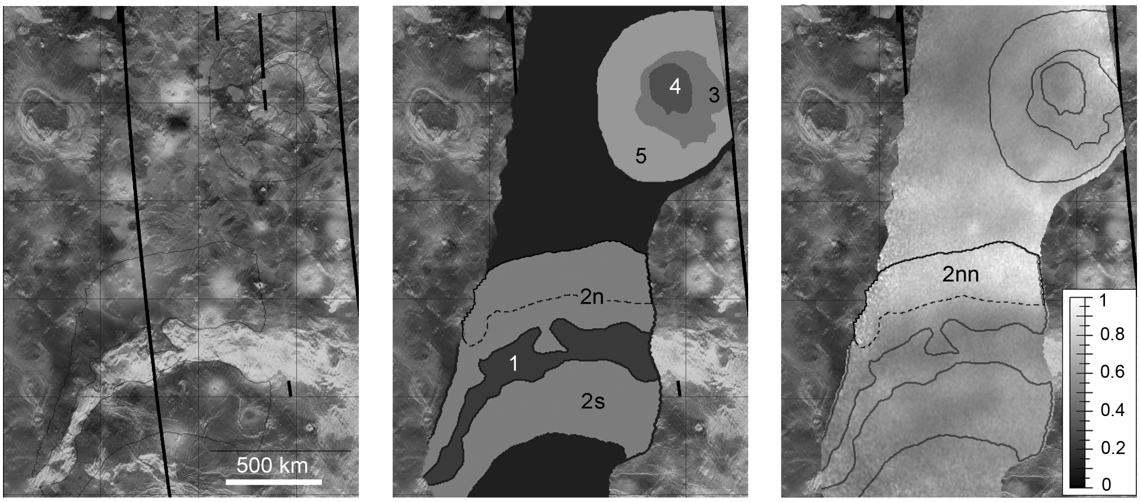

(a) SAR image.

(b) Outlines of VMC surface mosaic 470 with simplified geologic map showing units under study.

(c) Map of retrieved emissivity.

Figure 4.3: Part of area SW of Beta Regio where 1-µm emissivity measurements were done. Units: 1 — Chimon-mana Tessera, 2 — adjacent plains with units 2n (including subunits 2nn and 2ns) and 2s, 3 — major body of Tuulikki Mons volcano, 4 — the volcano summit, 5 — plains adjacent to Tuulikki Mons.

Table 4.1: Surface features under study (see fig. 4.3), their altitudes, area and virtual points count (see below).

Unit identifier	Surface type	Mean altitude and its std. dev., km	Virtual points count	Area, 10^3 km^2
1	Chimon-mana	0.6±0.4	103	142
2	Plains around Chimon-mana	−0.22±0.30	337	605
2n	Plains to the north from Chimon-mana	−0.4±0.3	180	323
2nn	Plains to the north from Chimon-mana (northern part)	−0.6±0.2	98	175
2ns	Plains to the very north from Chimon-mana (southern part)	−0.2±0.3	75	148
2s	Plains to the south from Chimon-mana	0.0±0.2	157	282
3	Tuulikki middle	−0.2±0.3	47	90
4	Tuulikki top	0.8±0.4	16	33
5	Plains around Tuulikki	−0.4±0.2	144	260

Table 4.2: Description of used models.

Model name	Model description	
	Temperature lapse L, K/km	Reference emissivity ε_0
lr8-e08	-8.1	0.8
lr8-e058	-8.1	0.58

the model and measured (by VMC or other instrument) data (fig. 4.4a). The increase of the assumed lapse rate leads to the opposite effect, that is to a higher calculated emissivity of the high-standing landforms (fig. 4.4b). This is true only if the studied landform is a kind of plateau, wide enough in comparison to the width of the blurring function. If the studied landform is not a plateau, but a mountain with prominent summit, then at any lapse rate the summit due to blurring of the NIR emission by the scattering in the clouds will not be seen as cold as it is. Because of averaging with hotter pixels surrounding the summit, the latter on the model image would appear hotter, its model emission will be higher. If the model point spread function size is smaller than the real one, then the model emission of the summit will be lower than its measured emission and this will result in higher calculated emissivity of the mountain (fig. 4.4c). If the point spread function radius is larger than the real one, then the model emission of the summit will be higher than its measured emission and this will result in lower calculated emissivity of the mountain (fig. 4.4d).

This effect is illustrated by calculation of model images of the surface emission done for real topography of Tuulikki Mons vicinity and area south of it. The topography of this area is characterized by presence of Tuulikki Mons (relatively large mountain with summit rising in the upper right of the image), two smaller mountains South-South-West of it and a crater south of Tuulikki (fig. 4.4e). Figure 4.4f shows the ratio of the surface emission images calculated for the point spread function diameter 50 km (numerator) and for diameter 100 km (denominator). It is seen on fig. 4.4f that decrease of the point spread function radius leads to decrease of model emission for the mountain tops and this should lead to their higher calculated emissivity. For the crater (depression, antimountain) the effect is opposite.

The combined effect of higher/lower lapse rate and the degree of the model blurring may lead to significant differences in the calculated emissivity of the studied landforms.

We calculated the mean ε and estimation of its standard deviation for each unit (table 4.3). To assess significance of the observed differences in the mean ε we applied Welch's test (Welch, 1947) for the unit pairs of interest. The atmosphere blurring makes our effective spatial resolution to be $\sim$ 100 km, which is much larger than a formal field of view of the VMC pixel. So, one cannot consider a value of each pixel as single and independent measurement. To correct this situation the study surface was "paved" with sub-areas of 100 km across. The number of such "tiles" on each unit (virtual points in table 4.1) was taken as the number of measurements for the test. The results of the estimates are given in table 4.3.

It is seen from table 4.3 that, as expected, the use of surface reference emissivity $\varepsilon_0 = 0.58$ has lead to the decrease of all calculated ε and differences between emissivities of different features. Most cases do show significant differences between selected units (table 4.1); we discuss this below.

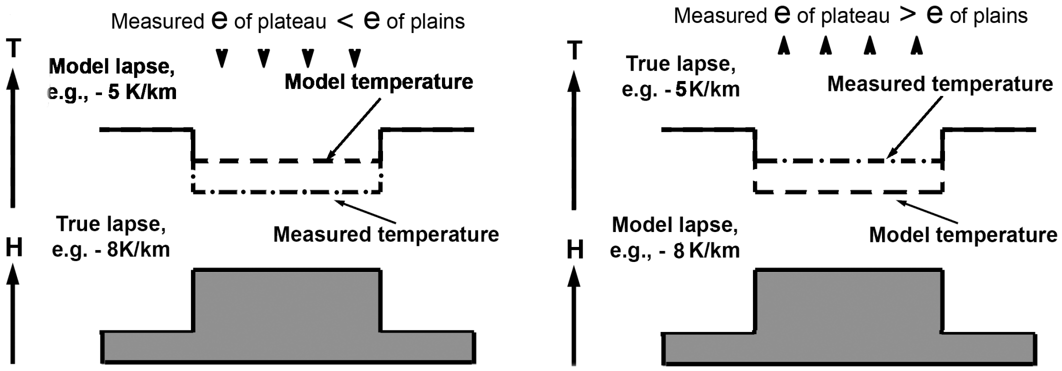

(a) Low lapse.

(b) High lapse.

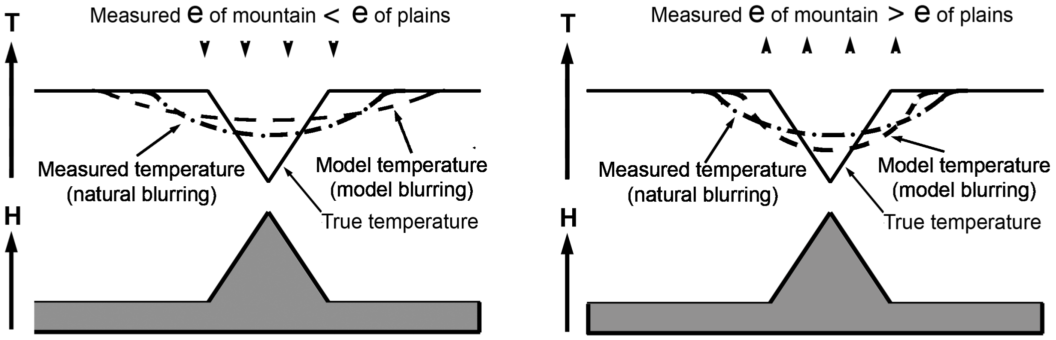

(c) Narrow point spread function.

(d) Wide point spread function.

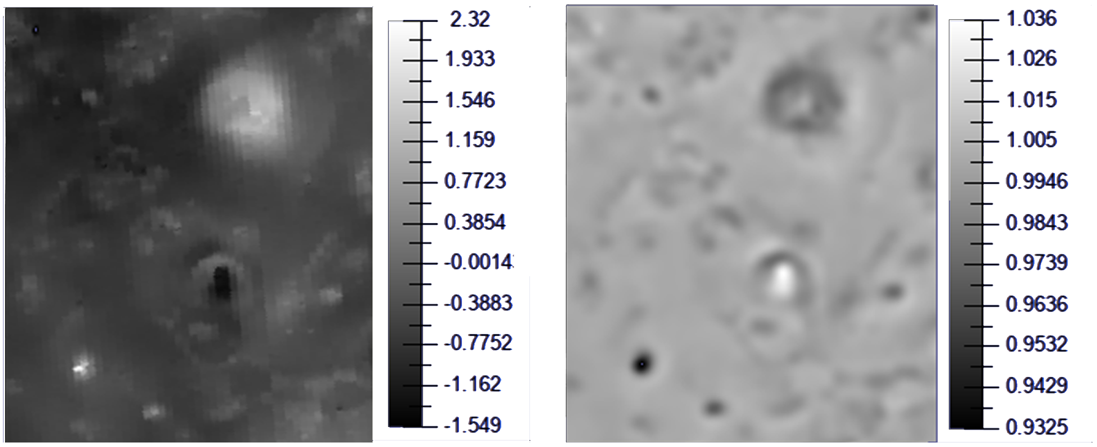

(e) Example: topography map of area 1.5°N – 13°N, 268°E – 278°E.

(f) Example: ratio of surface emission for model with 50 and 100 km blurring function width.

Figure 4.4: Dependence of measured emissivity on various model assumptions. The triangles on the diagrams visualize the sign of the effect: the triangle tip up indicates the emissivity increase, the tip down, the emissivity decrease.

Table 4.3: Comparison of emissivities of different surface units. See table 4.2 for models and table 4.1 for units description.

Unit A /	$\varepsilon\pm$ std. dev.		Diff. at	$\varepsilon\pm$ std. dev.		Diff. at
Unit B	Unit A	Unit B	0.05 level	Unit A	Unit B	0.05 level
	Lapse −8.1 K/km, $\varepsilon_0 = 0.8$			*Lapse* −8.1 K/km, $\varepsilon_0 = 0.58$		
1/2	0.55±0.37	0.56±0.31	No	0.43±0.03	0.42±0.27	No
1/2n	0.55±0.37	0.64±0.24	Yes	0.43±0.03	0.48±0.19	Yes
1/2s	0.55±0.37	0.47±0.35	No	0.43±0.03	0.35±0.32	Yes
2n/2s	0.64±0.24	0.47±0.35	Yes	0.48±0.19	0.35±0.32	Yes
1/2nn	0.55±0.37	0.76±0.15	Yes	0.43±0.03	0.55±0.11	Yes
1/2ns	0.55±0.37	0.50±0.27	No	0.43±0.03	0.38±0.24	Yes
2nn/2ns	0.76±0.15	0.50±0.27	Yes	0.55±0.11	0.38±0.24	Yes
2n/2nn	0.64±0.24	0.76±0.15	Yes	0.48±0.19	0.55±0.11	Yes
2n/2ns	0.64±0.24	0.50±0.27	Yes	0.48±0.19	0.38±0.24	Yes
3/4	0.63±0.07	0.55±0.04	Yes	0.48±0.04	0.43±0.02	Yes
3/5	0.63±0.07	0.53±0.45	Yes	0.48±0.04	0.38±0.4	Yes
4/5	0.55±0.04	0.53±0.45	No	0.43±0.02	0.38±0.4	No
2n/5	0.64±0.24	0.53±0.45	Yes	0.48±0.19	0.38±0.4	Yes
2s/5	0.47±0.35	0.53±0.45	No	0.35±0.32	0.38±0.4	No
2nn/5	0.76±0.15	0.53±0.45	Yes	0.55±0.11	0.38±0.4	Yes
2ns/5	0.50±0.27	0.53±0.45	No	0.38±0.24	0.38±0.4	No

4.3.1 Plains units v.s. plains units variabilities

Before we compare the 1-µm emissivities of Chimon-mana Tessera and the plains let us look what are emissivities of the plains. As it is seen from table 4.3 and fig. 4.3c they vary in the study area.

The plains units around Chimon-mana (units 2n and 2s) and Tuulikki Mons (unit 5) were outlined as bands surrounding these two landforms keeping the total widths of these two areas to be about 1000 km. Then from analysis of the map of calculated emissivity (fig. 4.3c) we divided unit 2n into two subunits (2nn and 2ns) which are noticeably different in their surface emissivities. The plains north from Chimon-mana Tessera (unit 2n) have significantly higher emissivity than the plains to the south (unit 2s). Statistically significant difference is observed for both the lr8-e08 and lr8-e058 models for all identified units and subunits of the Chimon-mana area (table 4.1).

The emissivity of plains around Tuulikki volcano (unit 5) is lower than that of units 2n and 2nn but higher than that of units 2s and 2ns. The unit 5 is 500 – 1000 km north of unit 2n and 1000 – 1500 km north of unit 2s, so potential variability in the clouds' density at these distances makes comparisons of unit 5 with units 2n including 2nn and 2ns and 2s less reliable than for the case unit 2n v.s. unit 2s, but probably acceptable. If we apply statistical estimates to these comparisons then the mentioned differences between unit 5 and units 2n and 2nn are statistically significant and between unit 5 and units 2s and 2ns are insignificant for both the lr8-e08 and lr8-e058 models. So the units 2n, 2s and 5 have different 1-µm emissivities (unit 2nn, the highest and unit 2s, the lowest) and the differences in most cases are statistically significant.

In attempt to understand the potential nature of these differences we put outlines of all the mapped units on the Magellan images (fig. 4.5). It is seen in this figure that plains of the study area are geologically variegated. On the background of radar-dark regional plains are patches of radar-bright ones and the younger volcanic centres with radially spreading lobate flows, also radar-bright. One of such volcanic centers is Tuulikki Mons volcano, which will be discussed below. Unit 2n is the most abundant in these radar-bright spots (the most abundant is subunit 2nn), unit 2s is the least abundant and unit 5 is in this respect intermediate. Figure 4.5b shows that unit 2n is on average at the lowest altitudes while unit 2s, on the highest and unit 5, at the intermediate, but close to unit 2n. Figures 4.5c and 4.5d show that unit 2n has on average the higher microwave emissivity and the lower Fresnel reflectivity comparing to units 2s and 5. We interpret the observed microwave emissivities and Fresnel reflectivities of these units (figs. 4.5c and 4.5d) as indication that the surface material within unit 2n and especially subunit 2nn is on average more consolidated comparing to that of units 2s and 5 and taking in mind that unit 2nn has the largest abundance of radar-bright patches (fig. 4.5a), which represent geologically younger materials comparing to the radar-dark regional plains, one may conclude that the surface material of the unit 2nn is less weathered and this is why it has the higher 1-µm emissivity. As it was shown in section 1.4.5 the weathered basalts typically have the lower 1 micron emissivity. This is probably due to the presence of highly reflective anhydrite, which according to thermodynamic modelling (*e.g.* Zolotov, 2007) is a typical product of weathering of basalts on Venus. The lowest 1-µm emissivity typical for unit 2s may also be because of smaller surface grain size due to presence of aeolian dust. The relatively high altitude typical for unit 2s is probably not the reason for its lowest 1-µm emissivity because the altimetrically higher main body (unit 3) and summit (unit 4) of Tuulikki Mons (see below) show an increase rather than a decrease of emissivity.

4.3.2 Chimon-mana Tessera (unit 1) v.s. adjacent plains (unit 2)

Here we compare the 1-µm emissivity of Chimona-mana Tessera with the adjacent plains to the north (unit 2n) and to the south (unit 2s). It is seen in the Table 4.3 that the calculated emissivity of this tessera is lower than that of the unit 2n and especially lower comparing to unit 2nn and higher than that of the unit 2s. In these cases the difference is statistically significant for both models lr8-e08 and lr8-058. As it follows from the consideration given in section 4.3.1, the northern plains (especially the unit 2nn) seem to be more pristine and less weathered than the southern plains. So we may conclude from the table 4.3 that the surface material of Chimon-mana Tessera has the lower (by 15 – 35 %) 1-µm emissivity than the basaltic material. This agrees with the results published by Helbert et al. (2008), Mueller et al. (2008), Hashimoto et al. (2008), and Gilmore, Mueller, et al. (2011), where lower (comparing to supposedly basaltic plains) emissivity for other tessera massifs have been reported.

If the lower (comparing to tessera) emissivity of the southern plains would be due to weathering of their material, one could expect that tessera surface material, which was exposed to

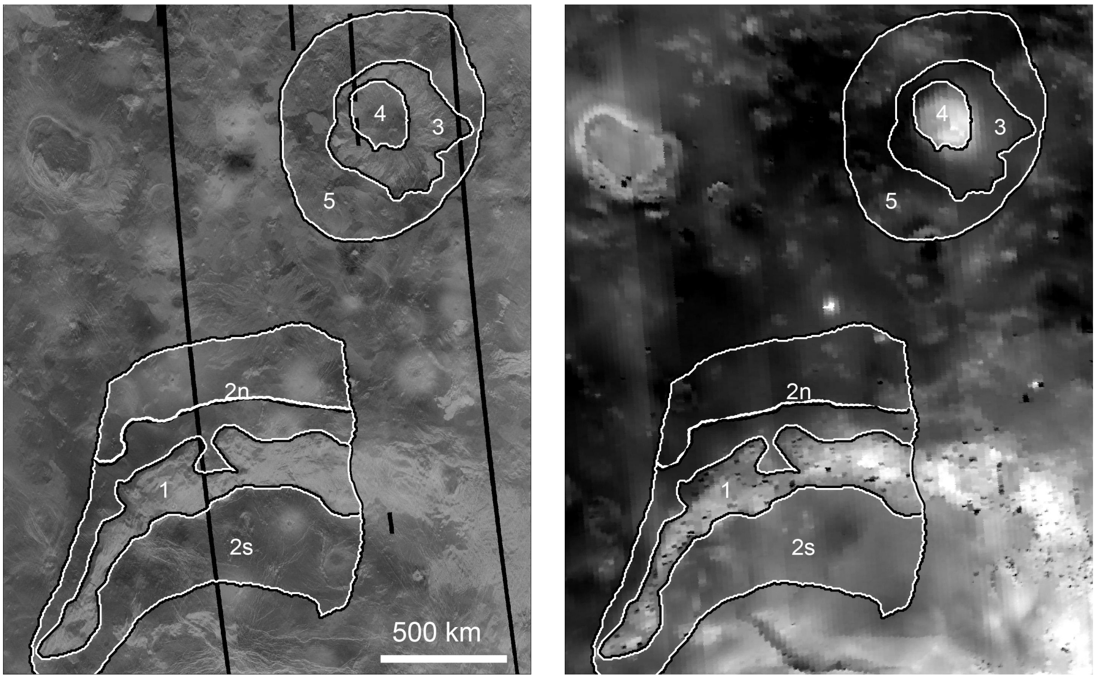

(a) SAR. (b) Topography.

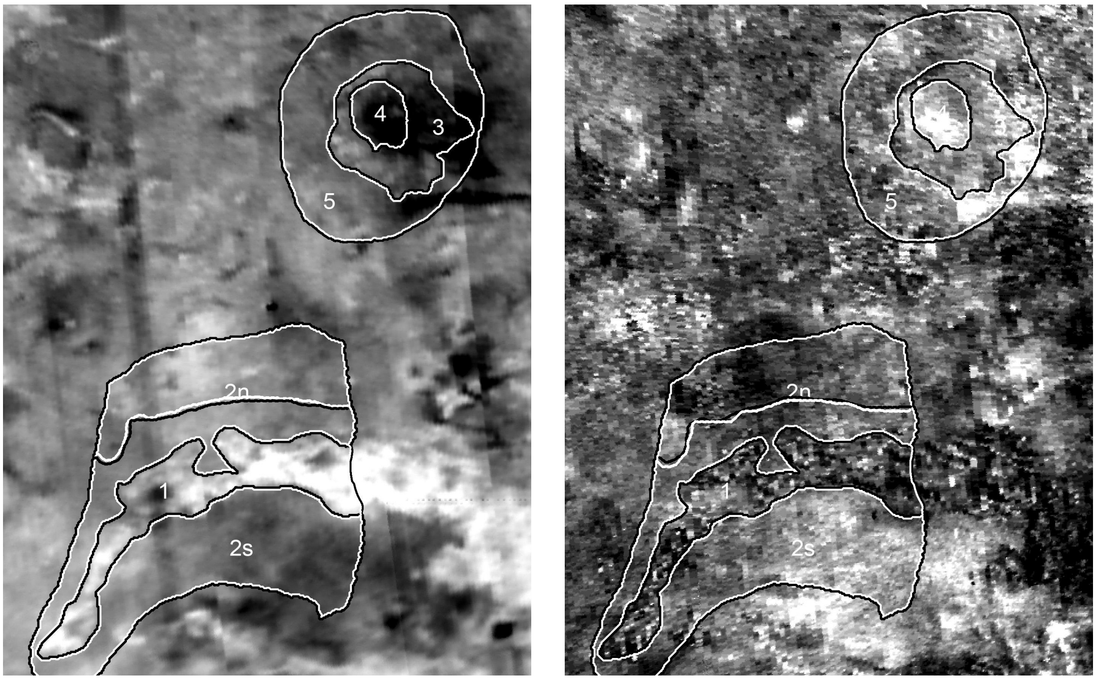

(c) Microwave emissivity. (d) Fresnel reflectivity.

Figure 4.5: Outlines of the mapped units on the background of the MGN-based images.

the atmosphere for the longer (comparing to the plains) time should also be weathered. However, thermodynamic calculations done by Barsukov et al. (1980, 1982) show that felsic materials should be stable in Venus surface environment and the weathering-involved changes of their mineralogy and thus emissivity are not expected.

The tessera surface is on average higher by $\approx 0.6\,\text{km}$ than the surface of adjacent plains (see table 4.1). On Venus at higher altitudes winds should be stronger than at the lower ones (Kerzhanovich and Marov, 1983) and this may control the surface grains size: the higher the surface, the stronger the wind, and probably the coarser the surface material grain size. This change, however, should favor the higher (comparing to the plains) emissivity of the tessera surface material and the fact that when comparing tessera with the northern plains we do not see the increase, but see a decrease, is an indication that the altitude effect even if it exists is weaker than the effect of mineralogic composition.

4.3.3 Tuulikki Mons volcano main body (unit 3) v.s. surrounding plains (unit 5)

It is seen in the table 4.3 that calculated emissivity of the material of the main body of Tuulikki Mons volcano (unit 3) is higher than that of surrounding plains (unit 5) and this difference is statistically significant for both models lr8-e08 and lr8-e058. As it was mentioned above, the Tuulikki morphology, the radial assemblage of rather long lobate lava flows on very gentle slopes, suggests a basaltic composition. The most part of the volcano is only slightly higher than the adjacent plains, but lobate flows, composing it, are geologically younger than the surrounding plains. So it is natural to expect that the Tuulikki material is less weathered than that of the surrounding plains and this probably explains its higher 1-µm emissivity. The unit 3 emissivity is virtually the same as that of unit 2n and this supports our suggestion that the units 2n material is not significantly weathered.

4.3.4 Tuulikki Mons summit (unit 4) v.s. its main body (unit 3)

It is seen in the table 4.3 that calculated emissivity of the material of the Tuulikki Mons summit (unit 4) is lower than that of the volcano main body (unit 3), but this is statistically significant only for the model lr8-e058 and not significant for the model lr8-e08. If nevertheless we assume that the difference is real, the lower emissivity of the summit material can be explained neither by the differences in the degree of weathering (on the volcano summit and slopes it should be approximately the same) nor by the coarser grain size of the summit surface material due to its higher altitude/higher wind velocities (it should work in the opposite direction. The reason may be different (more felsic) composition of the summit part of the volcano. This suggestion is supported by the presence of a steep-sided dome on the volcano top (fig. 4.6). As it was mentioned above in section 1.4, steep-sided domes were considered to be formed by eruptions of lavas geochemically more evolved comparing to basalts (Pavri et al., 1992) although other suggestions on their compositions have been also published (Fink and Griffiths, 1998; Bridges, 1995; Pavri et al., 1992).

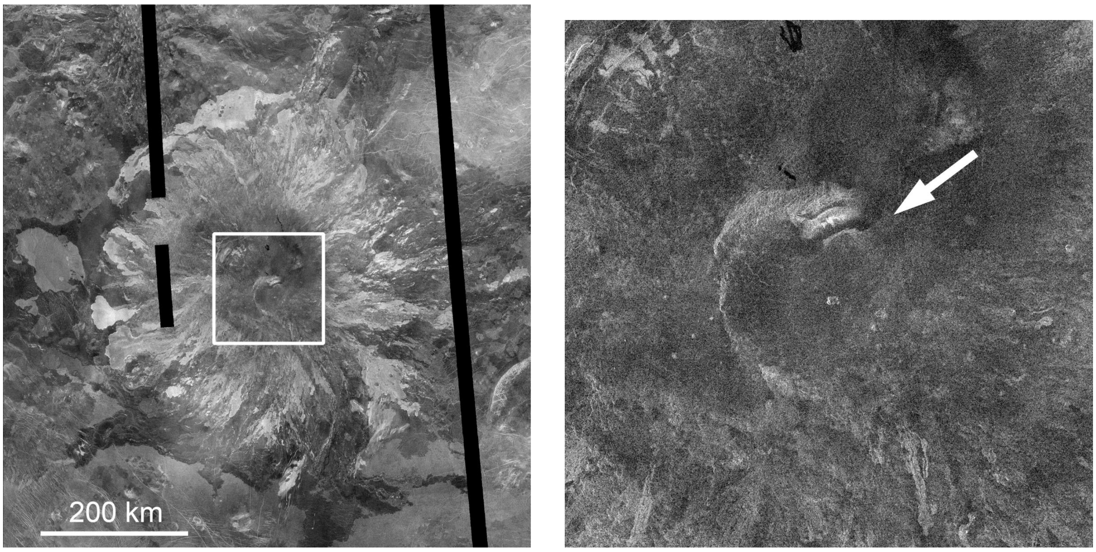

(a) General view.

(b) Steep-sided dome on its summit.

Figure 4.6: Tuulikki Mons volcano from MGN SAR images.

4.3.5 The 1-micron emissivity v.s. altitude correlation diagrams

As additional evidence of natural clustering of the identified units in the altitude – 1-µm emissivity space we have made for them correlation diagrams of these characteristics (fig. 4.7, fig. 4.8).

The figures show that in the values of 1-µm emissivity and altitude, plains show a significant scatter that obviously reflects their geologic variabilities as it was mentioned in the section 4.3.1. However, despite the mentioned variabilities, the considered units, are rather well clustered suggesting their geologic individualities.

4.3.6 Summary of the analysis of the 1-micron VMC data

Summarizing the results of our analysis of the 1-µm channel VMC images for the area SW of Beta Regio we can say that the plains here are rather variegated in their 1-µm emissivities. This seems to be mostly due to the degree of the weathering of their surface materials, that, in turn, probably depends on the geologic age with the younger materials being less weathered. The calculated emissivity of the surface material of Chimon-mana Tessera is about 15 – 35 % lower than that of the less weathered plains. So the tessera material here has lower emissivity than the material of supposedly basaltic plains. The lower 1-µm emissivity of tessera material may be indicative of its non-basaltic, probably felsic composition as it was suggested, first by Nikolaeva et al. (1992) and then by Helbert et al. (2008), Mueller et al. (2008), Hashimoto et al. (2008), and Gilmore, Mueller, et al. (2011). The calculated emissivity of the main body of Tuulikki volcano is very close to that of the plains which are considered to be the least weathered and higher than that of the surrounding plains of supposedly intermediate degree of weathering. The emissivity of the Tuulikki summit is somewhat lower than that of the volcano main body that can be due to different (more felsic?) composition of the surface material of the summit.

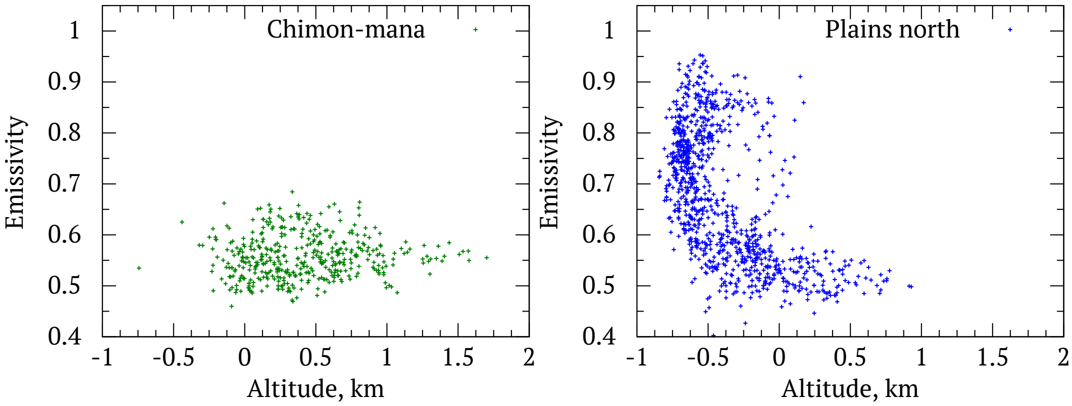

(a) Unit 1, Chimon-mana Tessera.

(b) Unit 2n, the northern plains.

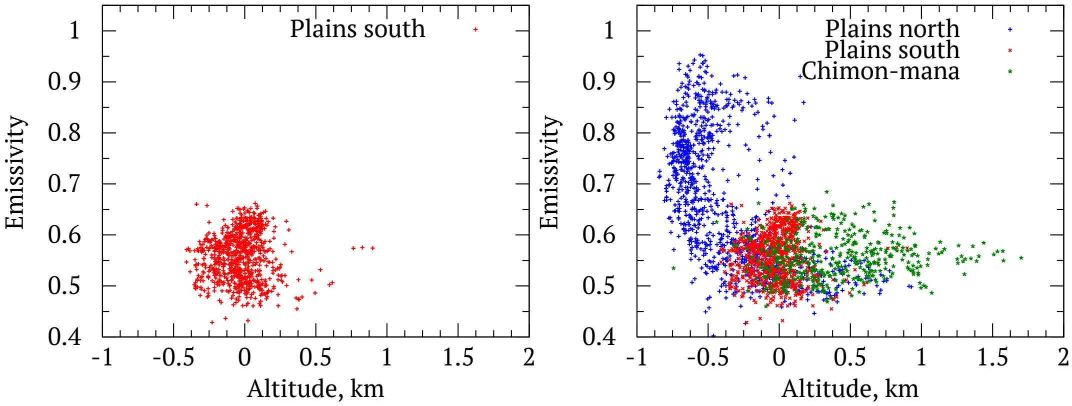

(c) Unit 2s, the southern plains.

(d) Units 2n, 2s and 1 altogether.

Figure 4.7: Correlation diagram for emissivity – altitude for Chimon-mana region.

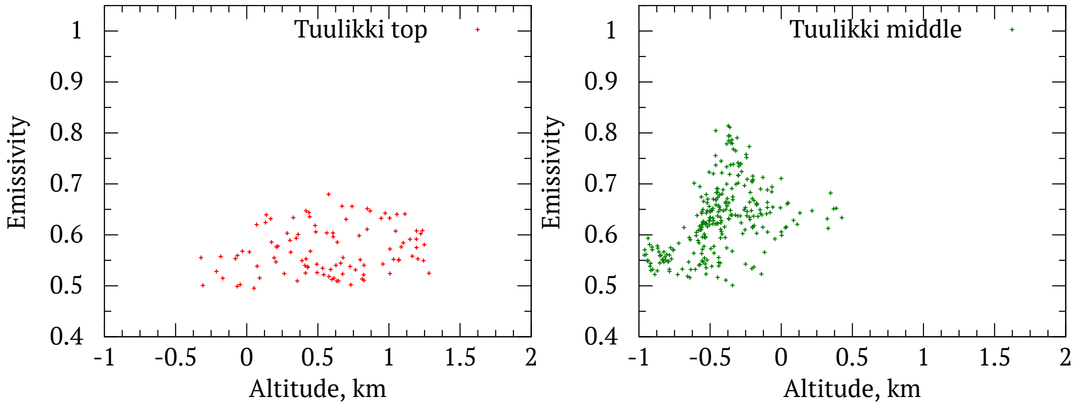

(a) Unit 4, Tuulikki summit.

(b) Unit 3, Tuulikki main body.

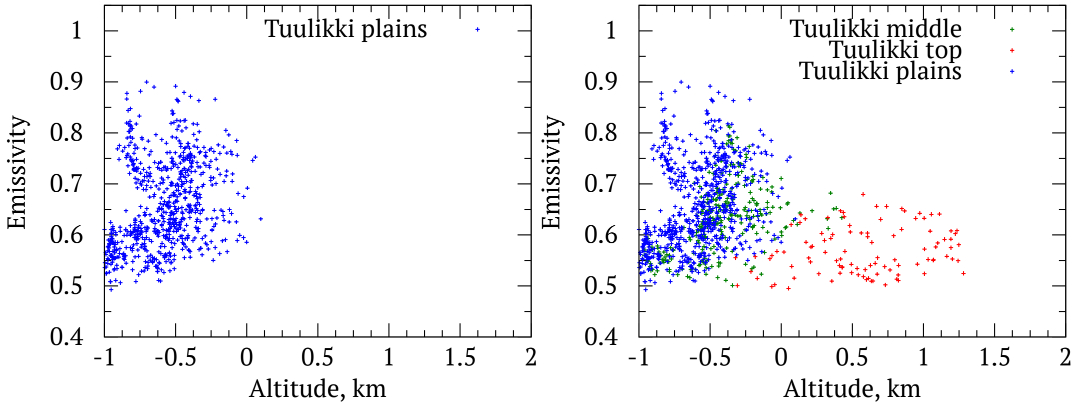

(c) Unit 5, plains adjacent to Tuulikki volcano.

(d) Units 3, 4, 5 altogether.

Figure 4.8: Correlation diagram for emissivity – altitude for Tuulikki region.

4.4 Discussion

During the 1990 Galileo Venus flyby, the Near Infrared Mapping Spectrometer (NIMS) investigated the night-side atmosphere of Venus in the spectral range 0.7 to 5.2 micrometers. The acquired data were analysed by Hashimoto et al. (2008) to study Venus surface emissivity at 1.18 µm wavelength in the part of Venus disk from 20°W to 90°E. To reduce the random noise the data were averaged within a circle with radius 250 km. The temperature lapse used in the analysis is given by the Venus International Reference Atmosphere (Seiff et al., 1985), that is close to −8 K/km.

Hashimoto et al. (2008) mostly do not discuss a regional difference, but analyse surface emissivity as a function of surface altitude. They found that the majority of observed lowlands (<0 km altitude) has higher emissivity compared to the majority of highlands (>2 km altitude). Their interpretation is that the highland materials are generally composed of felsic rocks (granites?), while the lowlands are basaltic. Some regional differences are nevertheless mentioned: Ishtar Terra, Eistla Regio, and Alpha Regio have relatively low emissivity, while Bell Regio and a band from Tahmina Planitia and Fonuecha Planitia have relatively high emissivity values.

Most highlands on Venus are tesserae (Ivanov and Head, 1996; Tanaka et al., 1997; Ivanov, 2008) so the lower emissivity of highlands found by Hashimoto et al. (2008) seems to be attributed to tessera terrain. However if we consider the mentioned above three particular regions of relatively low emissivity the association of low emissivity with tessera is not so straightforward: Two of these regions, Ishtar Terra and Alpha Regio, are dominated with tessera, but Eistla Regio is the area of extensive, essentially young volcanism with morphologies suggesting basalts.

It is very appropriate to compare our results with results from VIRTIS (section 2.1.2.2). The issue of emissivity differences of various landforms and terrains is described in Helbert et al. (2008), Mueller et al. (2008), and Gilmore, Mueller, et al. (2011). Their major finding is that the studied by them several massifs of tessera terrain show 1-micron emissivity lower than that of the surrounding supposedly basaltic plains. This implies that tessera material may be felsic although other options are also considered: different (from the plains) weathering regime and different surface grain size. Gilmore, Mueller, et al. (2011) suggest one more option: tessera material could be non-igneous, which would affect the emissivity through the difference in composition and/or in grain size. Some, but not all, volcanic edifices, according to these works, show emissivity higher than that of surrounding plains. In Lada Terra, high emissivities were measured for young volcanic flows extending from the rim of Boala Corona, nested inside Quetzalpetlatl corona. Mueller et al. (2008) explains their emissivity increase by possible ultramafic composition of the lavas.

Our results lead to generally the same conclusions: our calculated 1-µm emissivity of tessera surface material is lower than that of relatively fresh lavas of plains and volcanic edifices. This suggests that the tessera material is probably not basaltic and may be felsic.

We have found that the surface materials of plains are very variegated in their 1-µm emissivity that probably reflects variability of their local geologic histories, mostly the degree of chemical weathering with less weathered materials showing the higher emissivities.

We have also found a possible decrease of the calculated emissivity at the top of Tuulikki Mons volcano which may be due to different (more felsic?) composition of volcanic products on the volcano summit comparing to its slopes. This suggestion seems to be supported by the observation that at the volcano summit there is a steep-sided dome.

We did not find any indication of the increase of surface material emissivity at higher altitudes which could result from the expectedly higher wind velocities (and thus the coarser grain size of the surface materials) on the higher altitudes. This suggests that within the considered altitude range, which is only 1 – 1.5 km, this effect, if exists, is not noticeable.

4.5 Conclusions

1. The night-side VMC images provide reliable information on spatial variations of the NIR thermal emission of the Venus surface, which potentially may be interpreted in terms of geological characteristics of the studied area, including possible compositional differences between the geologic units.
2. Our calculations for the area SW of Beta Regio showed that 1-μm emissivity of tessera surface material is lower than that of relatively fresh supposedly basaltic lavas of plains and volcanic edifices. This is consistent with the hypothesis that the tessera material is not basaltic and may be felsic. These results are in agreement with the results of Helbert et al. (2008), Mueller et al. (2008), Hashimoto et al. (2008), and Gilmore, Mueller, et al. (2011) and with early suggestions of Nikolaeva et al. (1992). If the felsic nature of Venusian tesserae is confirmed in further studies, this may have important implications for geochemical environments in early history of Venus, indirectly supporting a hypothesis of water-rich early Venus (*e.g.* Kasting et al., 1984; Kasting, 1988; Grinspoon and Bullock, 2003).
3. We have found that the surface materials of plains in the study area are very variegated in their 1-μm emissivity, which probably reflects variability of their local geologic histories, mostly the degree of chemical weathering with less weathered materials showing higher emissivities. Future studies in the areas of geologically more homogeneous plains would be helpful in proving this suggestion.
4. We have also found a possible decrease of the calculated emissivity at the top of Tuulikki Mons volcano which, if real, may be due to different (more felsic?) composition of volcanic products on the volcano summit comparing to its slopes. This suggestion seems to be supported by the observation that at the volcano summit there is a steep-sided dome. More evolved lavas in the latest stages of evolution of basaltic magma chambers are rather typical for magmatism of Earth (*e.g.* McBirney, 2006).
5. Strategy of uniform surface coverage (*i.e.* observation in strictly “nadir mode”) does not provide sufficient information to estimate clouds opacity variations in most of the cases. Observations of the same target from three consequent orbits (with significant overlapping), from the other hand, give much more possibility to estimate clouds optical thickness variations much more precisely.

5 Search for ongoing volcanic activity

5.1 Introduction

In night-time Venus surface observations in NIR transparency "windows" the observed radiation intensity to a great extent depends on the surface temperature and thus may have a signature of the thermal effects of ongoing volcanic eruptions, if they occur. Because the surface temperature on Venus is a function of elevation (the higher, the colder), a typical VMC image shows a diffuse (due to blurring caused by the above mentioned scattering) picture of the large-scale topographic features with darker highs and brighter lows. The volcanic eruption is expected to be seen on this background as a bright spot not correlated with topographic depressions. In this work we describe various aspects of our attempts to search for ongoing volcanic eruptions in the Maat Mons area, but results of our consideration may be applicable to such searches in other areas of Venus as well.

5.2 The study area

We consider the area constrained by coordinates 5°S – 10°N, 185°E – 205°E (fig. 5.1). Here are the Maat Mons volcano (0.5°N, 194.6°E), which is the most promising target of our search (see below), and two more large young volcanoes: Sapas Mons, 8.5°N, 188.3°E, and Ozza Mons, 4.5°N, 201.0°E (Ivanov and Head, 2011).

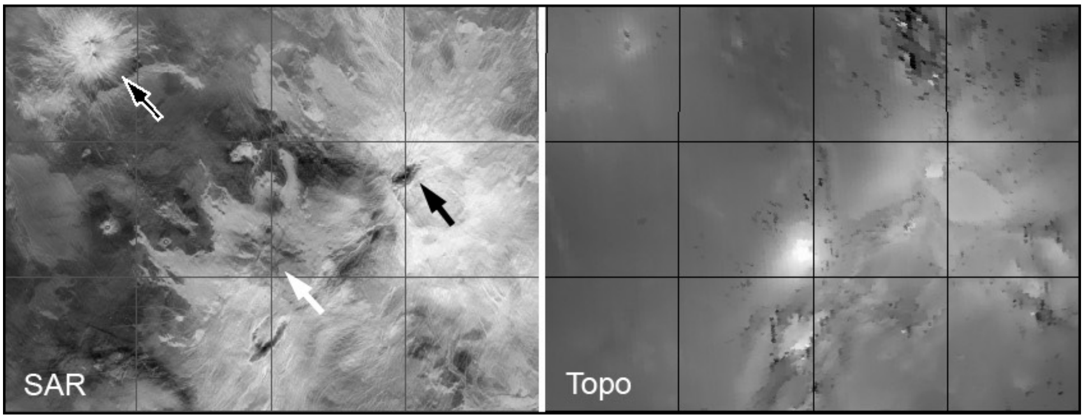

Figure 5.1: Side-looking radar image ("SAR") and topography ("Topo", brighter shades denote higher elevation) of the study area with three large volcanoes: Maat Mons (white arrow), Sapas Mons (black-and-white arrow), and Ozza Mons (black arrow). The coordinate grid is 5 × 5 degrees.

Maat Mons is the highest volcano on Venus; its summit is about 9 km above the mean planetary radius of 6051.8 km. Lava flows radiating from Maat Mons cover an area about 800 km across. In their eastern extension, these lavas are superposed on 40-km crater Uvaisy, which has an extended radar-dark parabola (Campbell et al., 1992). Presence of the latter suggests that the crater is very young, not older than a few tens of millions years (Basilevsky, 1993; Basilevsky and Head, 2002a,b) and this is why we consider this volcano as a perspective site for searching for the ongoing volcanism on this planet.

There is another evidence for youth of Maat volcanic activity. Typically, Venusian mountains above 4 km elevation have unusually low microwave emissivity. The nature of this phenomenon is controversial, but all hypotheses postulate the presence of some material with peculiar electromagnetic properties. Klose et al. (1992) noted that Maat Mons volcano shows a significant decrease in microwave emissivity only in some places, while most part of its summit has microwave emissivity close to the values typical of plains. The authors of that work suggested that this is because the summit lavas are so young that their exposure was insufficient to accumulate the peculiar material.

5.3 VMC observations

For the area of this study, VMC carried out night-time observations in 13 orbits during a 593 days long period from 31 Oct 2007 to 15 Jun 2009. One of these observation sessions (#1144, 2009-06-08) was taken at a very oblique view and the resulting images are of rather bad quality. We have excluded this orbit from our analysis. From the remaining 12 orbits six ones are separated in time and cover one day each while rest orbits cover six subsequent days. Observations taken during these sessions cover only part of the study area: Maat Mons was observed during 11 of these sessions, Sapas Mons, during 7 sessions, and Ozza Mons, during 10 sessions, in 4 of the latter — only partly (fig. 5.2).

Quality of VMC images is much better when taken in so called “nadir mode”, when camera points to nadir. In this mode of observations particular surface point is in sight of camera only for tens of minutes on each orbit.

As one can see from fig. 5.2 (compare for guidance with fig. 5.1) in the VMC images is well seen a prominent dark spot corresponding to Maat Mons mountain, south of which is a smaller spot of elevated feature at the flank of the rift zone. Ozza Mons is seen in VMC images as diffused dark spot northeast of Maat Mons. Sapas Mons is seen as a relatively small and less prominent dark spot comparing to Maat. Images taken on 2007-10-31, 2007-11-02, and 2008-06-24 show a granular noise. Difference in the noise level from mosaic to mosaic is mainly due to different observation geometry, which leads to difference of averaging of the single images. Images taken on 2009-06-11, 2009-06-12, and 2009-06-13 show diffuse brighter and darker east-west lineation changing from day to day. The latter probably correspond to latitudinal structures in the cloud layer (*e.g.* Taylor et al., 1997b). No prominent bright spots which could be expected as corresponding to ongoing volcanic eruptions are seen in any of the 12 images.

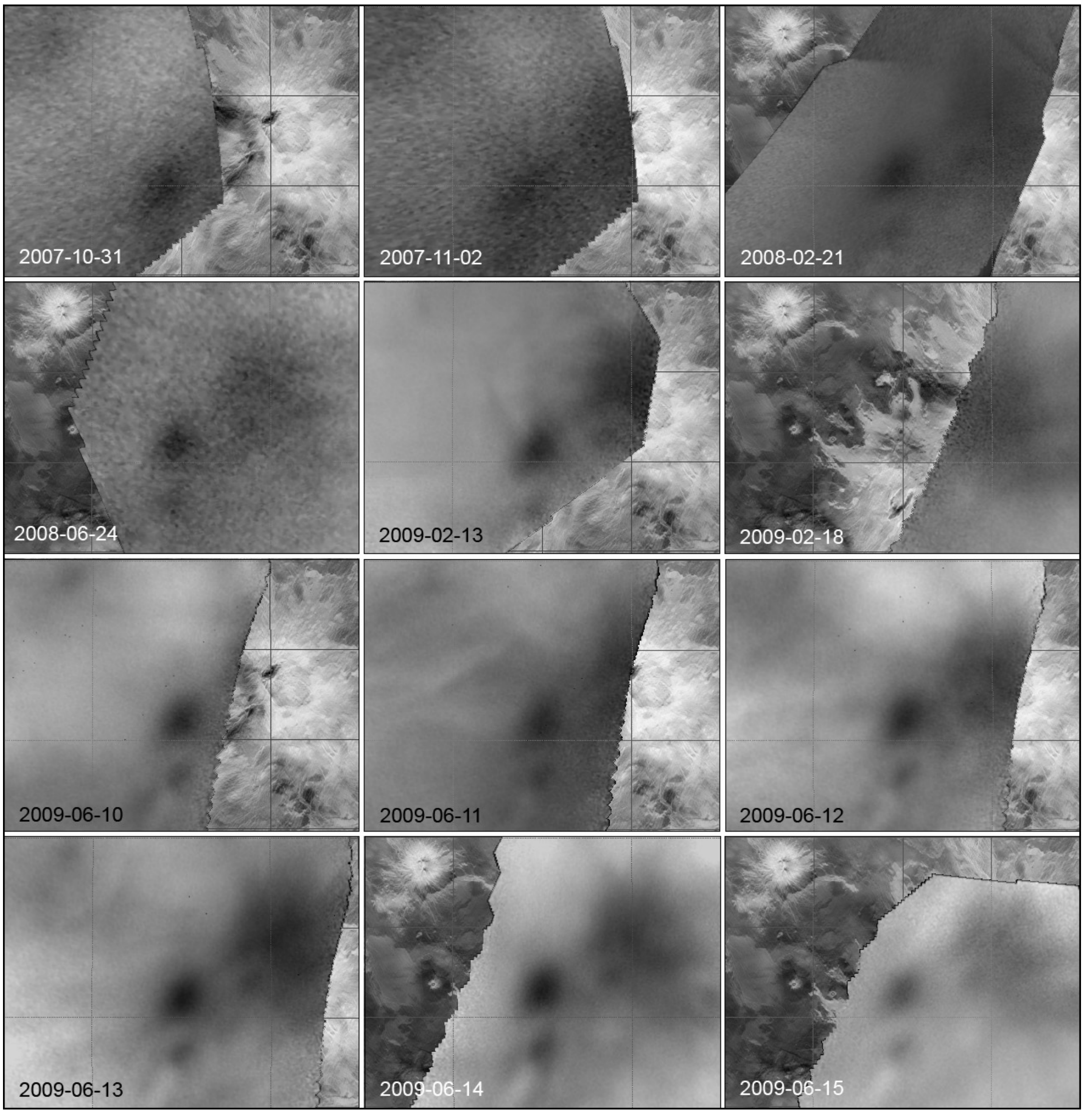

Figure 5.2: Fragments of VMC orbit-wise mosaics covering the study area on the background of SAR image. Dates when the given image was taken are shown in the lower left corner of each panel.

5.4 Comparisons with Mauna Loa volcano, Hawaii

Due to great density of Venus lower atmosphere, the thermal exchange between hot lava surface and the atmosphere is very effective, the lavas' surfaces cool fast, during one day (Head and Wilson, 1986; Hashimoto and Imamura, 2001), hence observation of hot lava would indicate eruption that occurred the same day. From observations of active terrestrial volcanoes we know that their activity is not permanent: periods of eruption are alternating with periods when volcano is dormant. Therefore observing Maat Mons volcano we could miss its activity even if in this "historic" period it is generally active but at the moment(s) of observations it was quiet. To analyse this possibility we consider a hypothetical situation that VMC observes the largest volcano of Earth, Mauna Loa, Hawaii in the way as it observed Maat Mons. Mauna Loa in its general morphology and morphology of its lava flows is similar to large volcanoes on Venus, so this comparison makes some geologic sense.

To analyse this situation we took a chronology of eruptions of Manoa Loa in 20th century, from 1900-01-01 to 1999-12-31 ((Lockwood and Lipman, 1987); these and updated data are available at http://hvo.wr.usgs.gov/maunaloa/history/main.html; http://www.volcano.si.edu/index.cfm). On total it is a 36 525 days long period during which there were 15 episodes of eruptions; duration of individual episodes varied from 1 to 145 days, altogether making 594 days of eruption. Thus, days with eruption make 1.6 % of the observation period. Assuming that observable thermal signature lasts for one day, the probability to observe eruption with a single observation is 1.6 %.

With these data we estimated the probability to encounter at least one day of eruption of Mauna Loa, if we had observed this volcano with the same timeline as VMC observed Maat Mons region. To do this we consider the actual time-line of eruptions and actual time-line of the observations (fig. 5.3), but consider the starting day of the observations to be random. For practical calculations we simply slided the VMC observation sequence along the Mauna Loa active/dormant sequence day by day and counted outcomes. The result is 8.3 %. Similarly, the probability to encounter more than one day of eruption is 4.8 %.

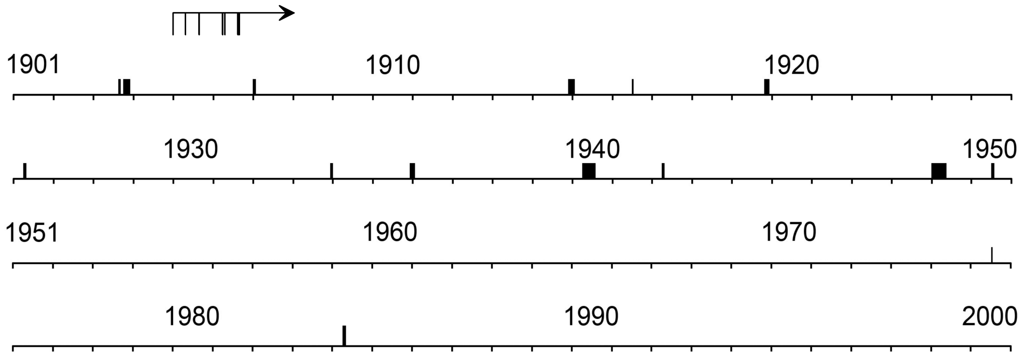

Figure 5.3: Mauna Loa eruption history with the VMC observations timeline of Maat Mons (plotted with arrow).

These estimates show that if for a moment we assume that any active eruption is detectable by VMC within one day, the chance to record the Mauna Loa type of volcanic activity is small, but far from negligible. Of course, Mauna Loa is one of the most active volcanoes of Earth and if we use as an analogue case eruptions of other terrestrial volcanoes, the probability estimates should decrease and through chronology of eruptions of those volcanoes one can estimate the degree of that decrease.

5.5 Visibility of lava eruptions on Venus from the orbit

Dense atmosphere and cloud layer of Venus are obstacles for the surface 1 micron emission to be recorded from the orbit. Simple estimations based on lava black body emission intensity and blurring due to clouds show that lava surfaces with temperature of 1500, 1100 and 900 K could be detected by VMC if they occupy 0.5 – 1, 20 – 30, and 500 km^2, respectively. A similar estimate has been obtained by Hashimoto and Imamura (2001). Here we try to visualize this effect (figs. 5.4 to 5.6 and 5.9). For that we produced synthetic "VMC" images of the study area and its vicinities showing intensity of the surface 1-micron emission being a function of only the surface temperature which in turn is a function of surface elevation known from the Magellan data set. Visually the synthetic images are very similar to real VMC images of the study area (compare fig. 5.4b with fig. 5.2). We have also made synthetic images with the same topography-dependent temperature field with superposed hypothetical lava flow of circular geometry having areas 1, 10 and 100 km^2 associated with the Maat, Ozza and Sapas volcanoes (fig. 5.4). In these simulations all synthetic lava fields have surface temperature 1000 K. Although erupting lava of basaltic composition typically has a temperatures about 1500 K (*e.g.* Kilburn, 2000), on the Earth the lava surface quickly gets covered with solid and cooler crust, and its effective temperature decreases and is rather close to 1000 K (*e.g.* Flynn and Mouginis-Mark, 1992); the same should certainly occur on Venus.

To obtain synthetic images, we needed to model surface emission and atmospheric effects. For the lava fields we assumed emissivity $\varepsilon = 0.8$. The emissivity of the real lava may vary, but for basaltic lavas it should be between 0.7 and 1.0. These variations give changes of the flux from the lava which are much smaller than changes due to temperature changes from ≈ 700 K to ≈ 1000 K. Thus assumption of constant lava emissivity is reasonable here.

The simulated maps of out-of-atmosphere brightness were visualized (converted into images) using linear stretch from the minimal to maximal values (*i.e.* the grey scale from black to white denote emission from the lowest to the highest).

As it can be seen from the fig. 5.4 the lava fields with surface temperature 1000 K and surface area of 1 km^2 are not seen in these simulations and probably can not be seen in VMC observations. Meanwhile the lava fields with the same surface temperature and surface area of 10 km^2 and larger are well seen in this simulation and probably would be well seen in VMC observations. It is seen in these simulations that presence in the field of view of relatively large shining lava field makes the background of the image to be rather dark. This is the effect of visualization (compare figs. 5.4c and 5.4d): setting contrast by maximal brightness decrease range of colours available for relatively dark pixels.

To further understand the issue of visibility we calculated what should be the area of the field of lava with surface temperature 1000 K to be seen in VMC observations and visualized these calculations (fig. 5.5). In particular, we were interested in contrast between lava field and surroundings (*i.e.* brightness ratio in image for region with hot lava and brightness of the surrounding area). The calculations were done for the circular lava fields having diameters of 1.2, 1.6 and 2 km (the areas are ≈ 1, 2 and 3 km^2, respectively). In this simulation the lava field

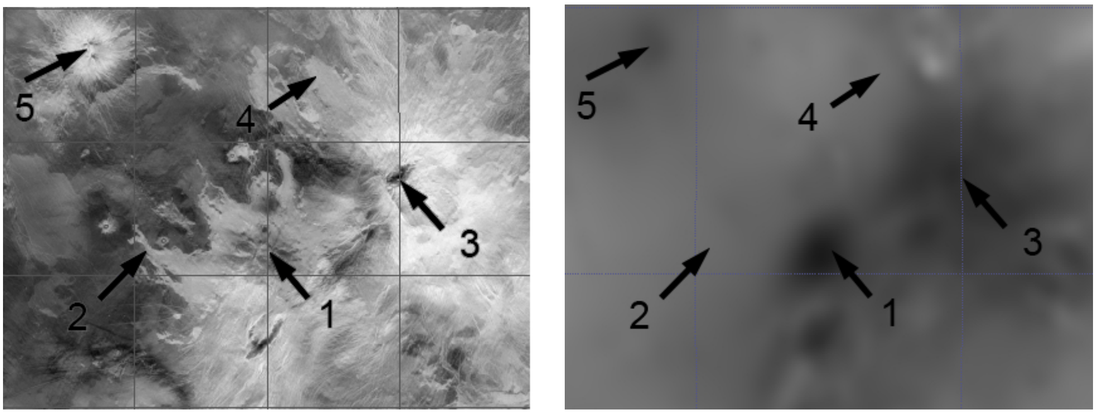

(a) Localities of hypothetical lava flow eruptions (all with 1000 K surface temperature) in the study area shown on the background of SAR image.

(b) The same localities on the background of synthetic “VMC” image of the area.

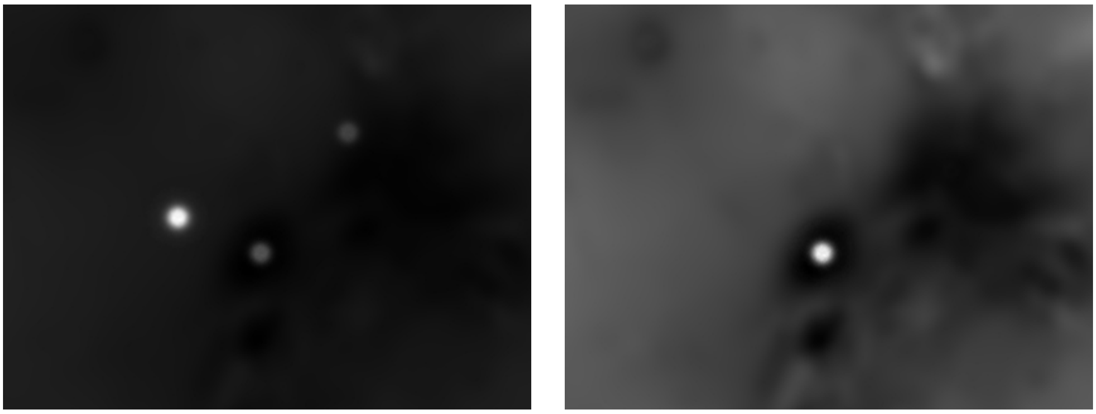

(c) Model simulation of visibility of the five mentioned hypothetical lava eruptions with lava surface areas from localities 1 through 5 to be 10, 100, 10, 1 and 1 km^2 correspondingly, only three eruptions (1, 2 and 3) are visible.

(d) Hypothetical eruption on the Maat Mons summit (also 10 km^2), it is better seen comparing with the case of five eruptions shown in the figure part (c) (see explanation in the text).

Figure 5.4: Model simulation of visibility of eruptions on tops and flanks of Maat Mons, Ozza Mons, and Sapas Mons. 1 — Maat Mons summit, 2 — Maat Mons flank, 3 — Ozza Mons summit, 4 — Ozza Mons flank, 5 — Sapas Mons summit.

locality is at the topographically low western flank of Maat Mons, approximately in the place where the 100 km^2 lava field was located in simulations presented in fig. 5.4 (arrow 2). This locality is at the level of only 1.5 km above the planet mean radius and thus in the synthetic VMC image this place looks rather bright.

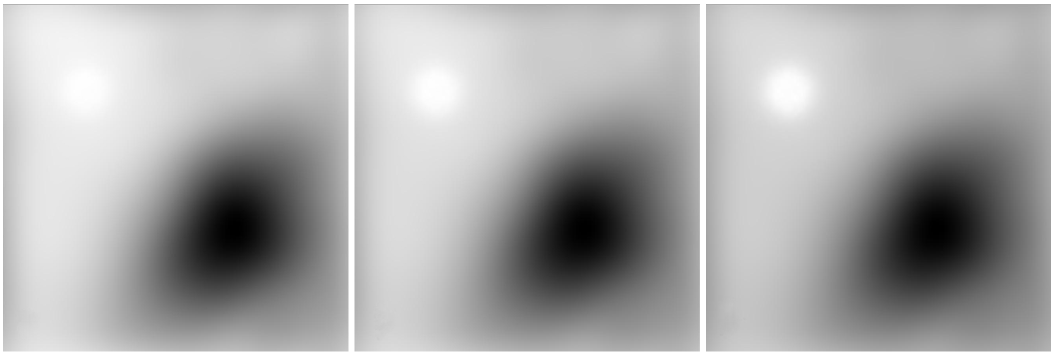

(a) ≈ 1 km^2.　(b) ≈ 2 km^2.　(c) ≈ 3 km^2.

Figure 5.5: Simulation of visibility of the lava field of different sizes at the lower flank of Maat Mons.

It is seen in the fig. 5.5 that the simulated lava field having area ≈ 1 km^2 (fig. 5.5a), is not reliably distinguishable from the surrounding terrain (calculated contrast is less then 1 %). With increase of the lava area to ≈ 2 km^2 (fig. 5.5b) and then to ≈ 3 km^2 (fig. 5.5c) the simulated lava spot begins to be marginally seen (calculated contrast 3 %) and then obviously seen (contrast 10 %).

We also calculated and visualized the visibility of lava flows located inside rift zones, where low topography makes the surface hotter, which causes the contrast in VMC images between the flow and its surroundings to be lower. Detection possibilities in a rift zone are worse than in a highland, but rifts are promising places to expect ongoing volcanism. We simulated VMC images with lava spots of different size in two areas north and south of Maat Mons (fig. 5.6). It is seen in fig. 5.6 that synthetic lava flows with surface temperature 1000 K in the rift zones started to be reliably seen when their areas are 4.5 km^2 and greater.

All of these simulations were made considering areas of planimetrically circular lava fields. However lava flows are typically elongated. To take into account this issue we have mapped lava flows of Tuulikki Mons volcano (fig. 5.7). We mapped only the youngest in each given case flows to avoid changing the planimetrical shape of the flows due to overlapping by the younger ones. For 62 mapped lava flows we measured area and length. From them we calculated “effective” width and length to width ratio. This statistic is showed in fig. 5.8.

With order of magnitude for typical aspect ratios equal 10, 1 km^2 lava field could be only a few hundreds of meters width (or even less). This will change visible contrast between lava and surface because blurring will work differently. To model visibility of a lava flows with irregular shape one needs to know atmospheric and surface properties on the scales of these irregularities (down to tens of meters), which is impossible at the moment. To assess the role of such effects we modelled rectangular lava fields with different length to width ratio using Gaussian fit of the burring function (fig. 5.9).

For typical length to width ratios of Tuulikki Mons lava fields of about 10 the decrease of contrast is not significant for relatively small (up to 10 km^2) lava fields, but becomes significant

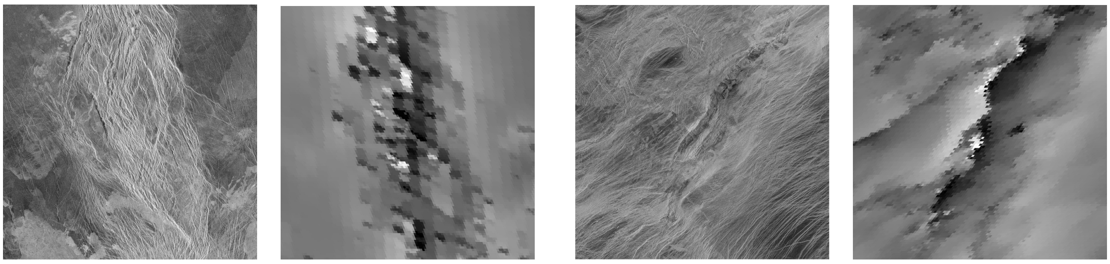

(a) MGN SAR image of the northern rift.

(b) MGN topo image.

(c) MGN SAR image of the southern rift.

(d) MGN topo image.

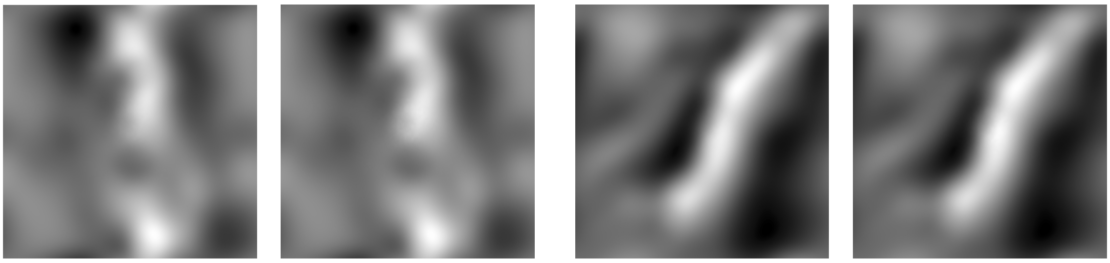

(e) ≈ 1 km^2 lava field.

(f) ≈ 2 km^2 lava field.

(g) ≈ 1 km^2 lava field.

(h) ≈ 2 km^2 lava field.

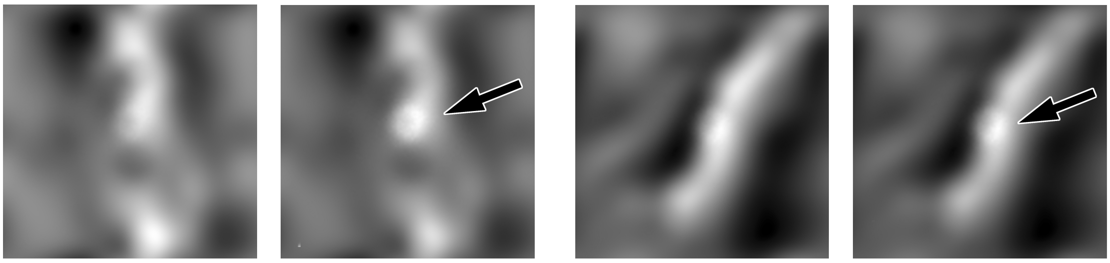

(i) ≈ 3 km^2 lava field.

(j) ≈ 4.5 km^2 lava field.

(k) ≈ 3 km^2 lava field.

(l) ≈ 4.5 km^2 lava field.

Figure 5.6: Simulation of visibility of the 1000 K lava field of different sizes in the rift zones north (left panels; 7.5°N – 12.5°N, 196°E – 201°E) and south (right panels; 10°S – 15°S, 187°E – 192°E) of Maat Mons with MGN SAR and topo images; arrows in panels (j) and (l) show position of the simulated lava field.

for extremely long fields with aspect ratio more than 1000. Decreasing of contrast becomes significant when longest of lava field dimensions approaches characteristic size of the blurring function.

Basing on these calculations, in fig. 5.7 we plotted several lines showing combinations of field area and length to width ratios which would produce given contrasts. In particular, we plotted line for contrast 1.1 (10 %) — detectable, 1.5 (50 %) — clearly visible, 2.0 and 10 — shining bright. One can see that majority of these lava fields would be detected by VMC if they would have temperature 1000 K and and all of them if the temperature would be 1500 K.

Thus, the results of simulations shown in figs. 5.4 to 5.6 and 5.9 show that in synthetic VMC images the lava fields with the surface temperature of 1000 K and having area ≈ 1 km^2, are not seen or marginally seen even if the simulated lava is on relatively dark background (Sapas Mons, arrow 5 in fig. 5.4). With increase of surface area to ≈ 2 km^2, the lava fields become visible of the plains level, and with increase of the area to 4 – 5 km^2, the lava field become visible even in rift zones where in VMC images surface looks rather bright.

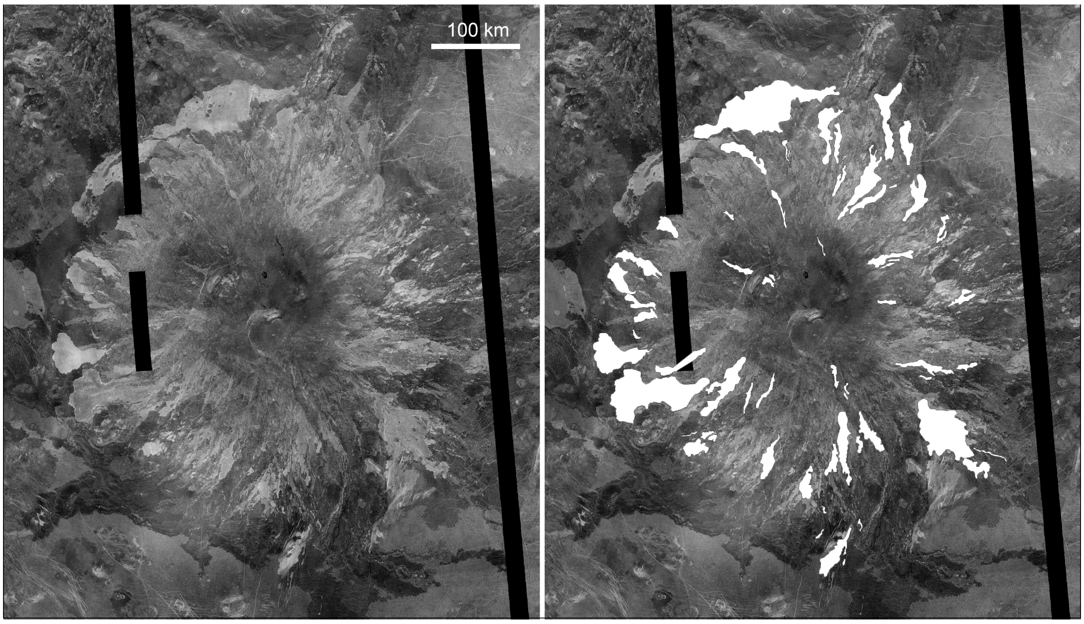

Figure 5.7: SAR image of Tuulikki Mons (10.3°N, 274.7°E) at the left and with lava flows selected at the right.

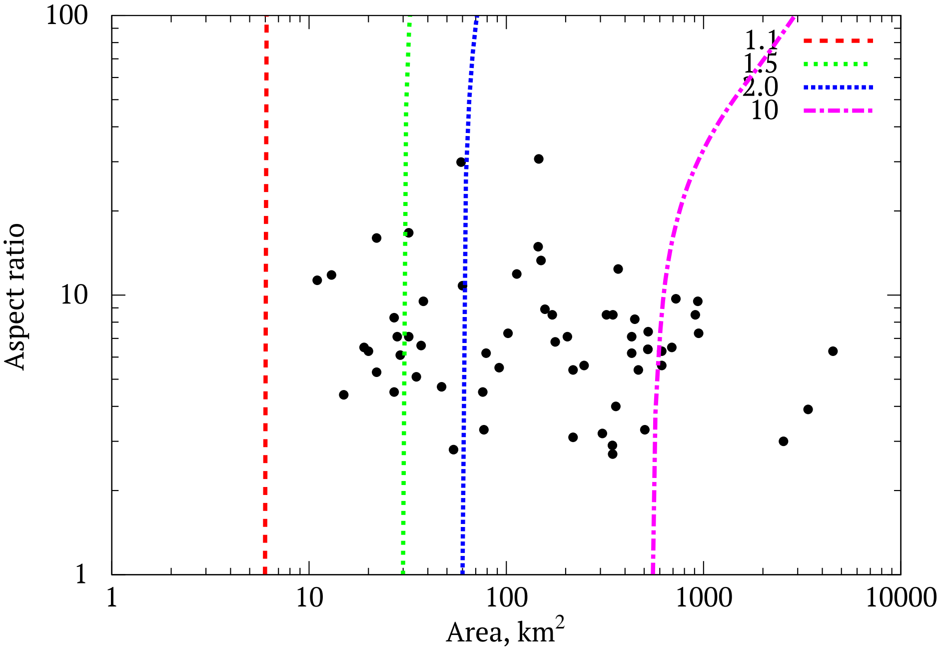

Figure 5.8: Distribution of surface area and aspect ratios of selected lava flows from Tuulikki-Mons. Lines mark levels of visibility that produce given contrast by lava fields with temperature 1000 K (see description in text and fig. 5.9).

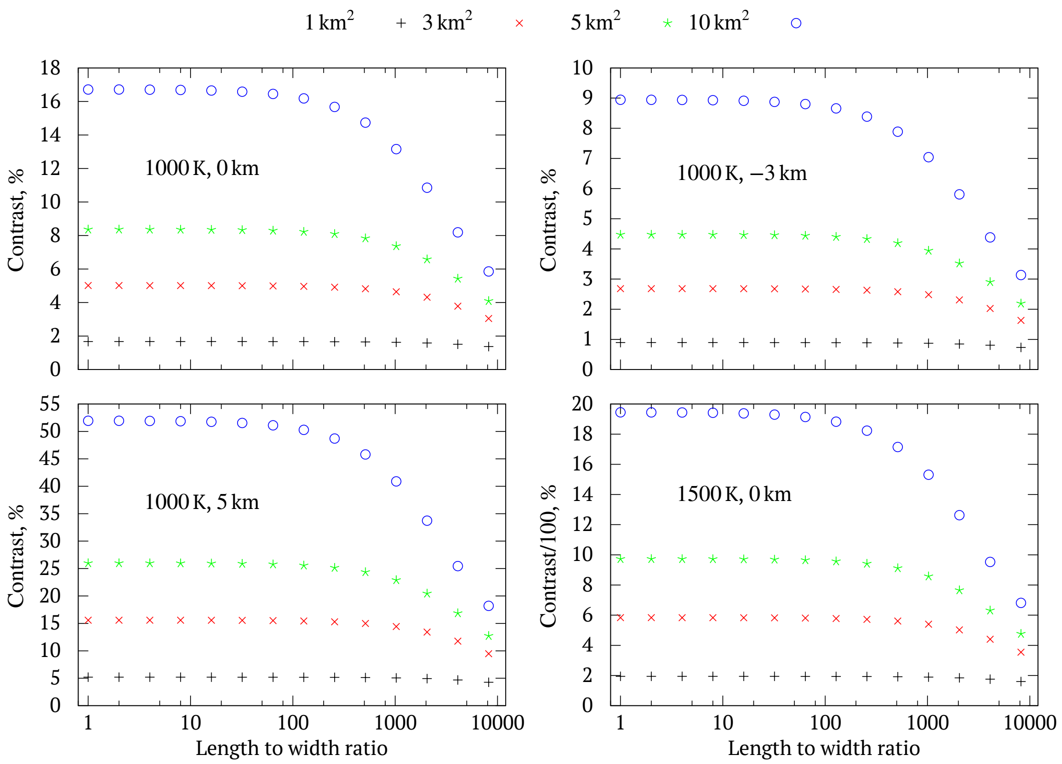

Figure 5.9: Visibility of lava fields with different length to width ratios at different altitudes.

Returning to analogy with the Mauna Loa eruptions, the lava flows formed by the 15 individual eruption episodes of the 20th century range in area from 1 km^2 to 112 km^2 with the median of 22 km^2 (Lockwood and Lipman, 1987). The majority of these lava fields are large enough to be observed by VMC, as long as they keep the 1000 K surface temperature. However, these lava fields have been accumulating during the weeks- and months-long eruption episodes, so that the instantaneous effective areas of hot enough parts of the lava fields were significantly smaller, and an unknown but probably significant part of them may loose their visibility.

The above considerations show that if Maat Mons volcano were presently active having the eruption timeline and lava flow characteristics similar to those of Mauna Loa in the 20th century, current VMC observations would be able to detect its ongoing volcanic eruption(s) with low but not negligible probability. Visual signature of the eruption would be a relatively small bright spot on the background of the surrounding terrain.

5.6 Published indications on ongoing/recent volcanism on Venus

Question about “modern” volcanic activity on Venus has long been a matter of great interest; see, for example an early discussion by Taylor and Cloutier (1986) and references therein. Speaking about “modern” or “recent” activity, we need to distinguish historically recent volcanism, that is detection of ongoing eruptions or their immediate aftermath, in other words, active eruptions during the last years, decades or centuries, and geologically recent volcanism, that is eruptions occurred in the past which is recent in comparison to the average age of the surface.

One of the published indications of historically recent volcanism is the ten-fold decline in the cloud top abundance of SO_2 correlated with the decline in polar haze observed by Pioneer Venus Orbiter in 1978 – 1986. This was considered by Esposito (1984) and Esposito et al. (1988) as a result of photochemical equilibration of SO_2 after massive injection of SO_2 caused by a powerful volcanic eruption. This possibility can not be ruled out, however, there has been published alternative explanations for this phenomenon. Clancy and Muhleman (1991) suggested that the observed SO_2 variations might be related to changes in the dynamics of Venus mesosphere, that seems to be supported by their microwave observations. Recent SPICAV observations by Marcq et al. (2011) also support the dynamical hypothesis. Finally, Krasnopolsky (2012) has shown that minor variations of the atmospheric dynamics at 50 – 60 km may induce variations of SO_2 and SO above 70 km by an order of magnitude. This may explain observations reported by Esposito, 1984 and Esposito et al., 1988 strong changes in SO_2 contents in the upper atmosphere of Venus.

Another potential indication of historically recent volcanism has been described by Bondarenko et al. (2010). They have reported suspected recent (tens to hundreds years old) large-scale volcanic eruptions in Bereghinia Planitia. Their work has been based on analysis of Magellan radiometer data, which showed excess of microwave (12 cm wavelength) thermal radiation suggesting tens of K temperature excess at a meter-scale depth. Although the evidence for increased subsurface temperature seems to be rather strong, the spurious effect of biased calibrations and other processing details are not completely excluded, as the authors admit.

With respect to geologically recent volcanism, we already mentioned (in the end of section 5.2) the work by Klose et al. (1992), who interpreted the absence of extremely low microwave emissivity at Maat Mons summit as indication of recently emplaced material that had not stayed at the surface for long enough to develop the materials responsible for low emissivity on other high terrains on Venus. Since the nature of the low-emissivity material is uncertain, it is very difficult to make any guess about the age constraints. In any case, we think about either alteration or deposition of at least several millimetres of material, probably, centimetres, and this hardly can be a historically quick process. Robinson and Wood (1993) found indications of similarly high emissivity at high elevations in a few other volcanoes. They also found that some small radar-bright stratigraphically young lava flows on low-elevation flanks of Maat Mons and a few other volcanoes have unusually low emissivity, lower than typical volcanic plains but still higher than typical mountaintops. They speculated that these flows can be geologically very young and emissivity could be lowered by the presence of pyrite, which would be stable only under the presence of residual volcanic gases in the pore space in shallow subsurface.

Smrekar et al. (2010) reported on another possible circumstantial evidence of geologically recent volcanism. They have analysed data acquired by the VIRTIS and found that lavas of four volcanoes of the Imdr-Themis-Dione Region showed NIR emissivities higher than those of the surrounding plains. This was interpreted as indication that these lavas are unweathered and thus very young. Determining area of these flows and assuming their thickness, the authors estimated the volume of these lava fields. Dividing this volume by the rate of volcanism taken from different literature sources they calculated the age of these lavas to be from 2.5 Ma to 25 ka.

None of the studies mentioned above provide simultaneously direct and unambiguous evidence for the ongoing or very recent volcanic activity on Venus but rather suggestions or indications. Direct search of such activity continues to be the timely task in the study of this planet. Observations from the circum-planet orbits, including the registration of the night thermal emission of the surface in the transparency windows continue to be a promising approach.

5.7 Suggestions for future near-infra-red observations from the circum-Venus orbit

Although several years of limited VMC observations of the night side surface of Venus did not result in discovery of the ongoing volcanism on this planet, this does not discredit our approach. As it was shown above, if Venus is still volcanically active, probability to register it with VMC observations is not negligible. The above-described simulation of propagation of the 1-μm emission through the dense atmosphere and clouds of Venus showed that thermal emission from the 1000 K hot surface of lava flow(s) having area greater than 3 – 5 km^2 is so distinct that it can be visible in the VMC images not only on the volcano tops, but at their low-elevation flanks and even within the rift valley lows. This expands the set of perspective targets for the search from separately standing volcanoes like Maat Mons or Sapas Mons, to all the extended system of young rift zones on Venus (Solomon et al., 1992; Taylor et al., 1997a; Basilevsky and Head, 2000; Ivanov and Head, 2011). VEX will be operational until 2015, and thus, we recommend to continue the search of ongoing volcanic activity on Venus with VMC camera.

The VMC attempts to search for the ongoing volcanism, however, are seriously limited by the necessity to do observations only within the solar-eclipsed part of the Venus Express orbit (to avoid the stray light in the camera) that in combination with rather large orbital period (24 hours) leads to observations which are limited both in area (a few thousands km^2 per orbit) and time (once per 24 hours). It would be interesting to consider, how in general NIR observations can be optimized for search for the thermal effect of active volcanism on Venus. Blurring by the atmosphere and clouds defines the optimal resolution: resolution elements (pixels) should be a few times smaller than the point spread due to blurring, that is about 20 km at the surface. With this pixel size, the whole night side of the planet or its significant part can fit into the frame of modern panoramic (array) detectors. Short (≈ one day) visibility of hot lavas dictates the necessity of frequent monitoring observations, which means that a significant part of the night side of the planet should be imaged once or twice daily, which can be done only from long distance. Earth-base observations are very complicated (Lecacheux et al., 1993) and limited to the certain part of the surface because of sunlight scattered in the Earth atmosphere (the night side is observable only on day or dusk or dawn sky). Astronomical observations with space telescopes are hardly possible, because such facilities are usually not schedulable for monitoring planetary observations, and also because usually they cannot observe targets at a small angular distance from the Sun (which is required to observe a significant part of the night side); in addition, due to Venus — Earth spin — orbit commensurability, Earth-orbiting telescopes can observe only one side of Venus at night, and this side is not rich in volcanoes and rifts. Thus, monitoring requires a Venus orbiter at a high orbit or strongly elliptical orbit with apoapsis at low latitudes. The stray light problem is inherent for night-side monitoring: the bright illuminated limb is always in or close to the filed of view and the Sun is always at a small angular distance from it. Because of this, a monitoring camera requires a special design to mitigate the stray light.

Finally, we compare NIR imaging of the surface with another method for detection of the thermal effects of active volcanism namely, microwave radiometry. For a longer-wavelength part of microwave section of electromagnetic spectrum, the Venus' atmosphere is not only translucent, like in the NIR transparency windows, but completely transparent, and no atmospheric blurring occurs. Due to this, the surface resolution of a radiometer is defined by antenna size and distance from the surface, and has no principal limitations. Thus, much smaller patches of hot material on the surface can be detected with this method, which potentially increase chances for detection. Another advantage of microwaves over IR light is that the microwave thermal radiation is formed in much thicker skin (centimetres to tens of meters, depending on wavelength and material), and hence, the detectable thermal signature of lavas lasts for much longer (weeks to decades), which again increases the chances. The problem of stray light is minor for this method. Microwaves, however, also have significant shortcomings. First, microwaves are on the long-wavelength shoulder of the Planck curve, and the contrast in emission intensity between hot lavas and regular surface is small ($\approx$ 30 %), while for 1 micron wavelength, which is on the short-wavelength shoulder, a 1000 K surface is brighter by a factor of $\sim$ 100. Due to this weakness of the microwave signature, it is inherently difficult to distinguish between emissivity anomaly and temperature anomaly (like in the case of Bondarenko et al. (2010)), unless an increase in emission is observed in repeating observations of the same site. Second, microwave radiometers require a large antenna, are heavier than cameras, and demand a low orbit to achieve the advantageous resolution keeping the antenna size reasonable. Third, panoramic detectors do not exist for microwaves; as a result, effective global monitoring actually requires almost continuous observations from low circular polar orbit, while contiguous coverage of small sites of interest (like Maat Mons) requires complicated program of observations and spacecraft operations. Because of these shortcomings, the microwave radiometric observations do not supersede IR observations completely, and the search for thermal signature of active volcanism in the near-IR transparency windows still makes much sense.

5.8 Conclusions

1. We consider different aspects of the search of the ongoing volcanic activity from observations taken by the Venus Monitoring Camera (VMC) 1 micron channel onboard of Venus Express. Here our emphasis is the areas of Maat Mons volcano and its vicinities which based on analysis of the MGN SAR images shows evidence of geologically very young volcanism.
2. Analysis of VMC images taken in 12 observation sessions during the time period from 31 Oct 2007 to 15 Jun 2009 did not reveal any suspicious high-emission spots which could be signatures of the ongoing volcanic eruptions.
3. We compared this time sequence of observations with the history of eruptions of volcano Mauna Loa, Hawaii, in the 20th century. This comparison shows that if Maat Mons volcano had the eruption history similar to that of Mauna Loa, the probability to observe an eruption in these VMC observation sequences would be about 8 %, meaning that the absence of detection does not mean that Maat is not active in the present epoch.

4. These estimates give probability to have lava field in the camera's field of view but do not consider the effect of absorption and blurring of the thermal radiation coming from Venus surface by the planet atmosphere and clouds, which decreases detectability of thermal signature of fresh lavas. To assess the role of this effect we simulated NIR images of the study area with artificially added lava flows having surface temperature 1000 K and different areas. These simulations showed that 1 km^2 lava flows should be marginally seen by VMC. Increase of the lava surface area to 2 – 3 km^2 makes them visible on the plains and increase of the area to 4 – 5 km^2 makes them visible even in deep rift zones. Elongation of lava fields in general increases these values. However, for typical length to width ratios of about 10 the decrease of contrast is not significant, but becomes significant for extremely long fields with aspect ratio more than 1000.
5. Typical individual lava flows on Mauna Loa are a few km^2 large, however, they often have been being formed during weeks to months and the instantaneous size of the hot flow surface was usually much smaller. Thus the detection probability is significantly lower than 8 %, but it is probably far from negligible.
6. Our consideration suggests that further search of Maat Mons and other areas including young rift zones with VMC, in particular, makes sense and should be continued.
7. More effective search could be done if observations simultaneously cover most part of the night side of Venus for relatively long (years) time of continuous observations.

6 Conclusions and outlook

This thesis is focused on investigation of the Venus surface emissivity variations and their correlation with geological units. This has been done via analysis of the images of surface thermal emission and numerical modelling.

Venus Monitoring Camera (VMC) images of the Venus night side, obtained in 1-µm channel, and results of Magellan Venus Radar Mapping Mission (MGN) experiment were used as observational data. After the discovery of transparency "windows" in the Venusian atmosphere, sounding of the surface have been performed a number of times from ground and from spacecraft (*e.g.* Meadows and Crisp, 1996; Hashimoto et al., 2008; Mueller et al., 2008; Arnold et al., 2008; Haus and Arnold, 2010). But it was never done before with a CCD camera on-board a spacecraft orbiting Venus. There were doubts (*e.g.* Moroz, 2002) that accuracy of such observations is enough to be sensitive to the surface emissivity.

The quantitative analysis was done via numerical modelling of surface thermal emission and radiative transfer (RT) in the atmosphere; and model results (synthetic images) were compared to the VMC images to deduce the surface emissivity. For RT modelling we used custom developed Monte-Carlo based code (section 3.2), calculations by Ignatiev et al. (2009) for gaseous absorption, and atmosphere structure model from Tomasko et al. (1985).

The thesis mainly focuses on the two following questions: i) is there mineralogical difference between tesserae terrain and plains terrain, and ii) is there any evidence of ongoing volcanic activity? Sounding in near infra-red (NIR) transparency "windows" seems to be the only way to retrieve the information about tesserae composition in foreseeable future. We approached the first task not globally, but locally, studying Chimon-Mana tessera and its vicinities. For the second target we a) analysed VMC images of Maat Mons region, which is rather promising target because there are relatively young lava flows; b) did numerical and semi-analytical modelling of lava fields visibilities of different temperatures, areas, and shapes; c) compared shapes of lava flows from Tuulikki volcano with results of modelling to assess significance of visibility decrease for elongated fields.

We can summarize our results as follows:

1. This work has shown that the night-side VMC images provide reliable information on spatial variations of the NIR thermal emission of the Venus surface, which potentially may be interpreted in terms of geological characteristics of the studied area, including possible compositional differences between the geologic units.
2. We developed and applied (section 2.1.2.1) observation strategy that gave possibility to estimate clouds optical thickness variations in observed area (chapter 3). This is important for the analysis of VMC observations, because having only one spectral channel, as the VMC does for surface observations, it is impossible to deduce optical thickness of the atmosphere simultaneously with determining surface properties. However, observ-

ing the same surface area from different positions at different times one can estimate changes in the clouds optical thickness.

3. Assuming that emissivity of plain terrain do not strongly (and systematically) vary with altitude, we used the fact that VMC has observed large plain area at various altitudes and determined the value of gaseous absorption coefficient (0.12 km^{-1}, section 3.1.1). Absorption by (mainly) CO_2 and H_2O in the dense lower atmosphere is strong enough to be significantly different for highlands and lowlands (Moroz, 2002), but, however, at present time it is impossible to either calculate theoretically or measure in laboratory absorption in far wing of CO_2 and H_2O lines (where, naturally, transparency "windows" are located) under such high pressure and temperature that are exits in the lower atmosphere. Therefore it has to be determined from observations.

4. We retrieved and analysed (chapter 4) emissivity maps for the region South-West of Beta Regio, which includes Chimon-Mana tessera, Tuulikki volcano and surrounding plains.
    (a) Our calculations showed that 1-μm emissivity of tessera surface material is lower than that of relatively fresh supposedly basaltic lavas of plains and volcanic edifices. This is consistent with the hypothesis that the tessera material is not basaltic and may be felsic. These results are in agreement with the results of Helbert et al. (2008), Mueller et al. (2008), Hashimoto et al. (2008), and Gilmore, Mueller, et al. (2011) and with early suggestions of Nikolaeva et al. (1992). If the felsic nature of Venusian tesserae is confirmed in further studies, this may have important implications for geochemical environments in early history of Venus, indirectly supporting a hypothesis of water-rich early Venus (*e.g.* Kasting et al., 1984; Kasting, 1988; Grinspoon and Bullock, 2003).
    (b) We have found that the surface materials of plains in the study area are very variegated in their 1-μm emissivity, which probably reflects variability of their local geologic histories, mostly the degree of chemical weathering with less weathered materials showing higher emissivities. Future studies in the areas of geologically more homogeneous plains would be helpful in proving this suggestion.
    (c) We have also found a possible decrease of the calculated emissivity at the top of Tuulikki Mons volcano which, may be due to different (more felsic?) composition of volcanic products on the volcano summit comparing to its slopes. This suggestion seems to be supported by the observation that at the volcano summit there is a steep-sided dome. More evolved lavas in the latest stages of evolution of basaltic magma chambers are rather typical for magmatism of Earth (*e.g.* McBirney, 2006).

5. We considered different aspects of the search of the ongoing volcanic activity (chapter 5). Here our emphasis is the areas of Maat Mons volcano and its vicinities which based on analysis of the MGN synthetic aperture radar (SAR) images shows evidence of geologically very young volcanism.
    (a) Analysis of VMC images taken in 12 observation sessions during the time period from 31 Oct 2007 to 15 Jun 2009 did not reveal any high-emission spots which could be interpreted as signatures of the ongoing volcanic eruptions.
    (b) We compared this time sequence of observations with the history of eruptions of volcano Mauna Loa, Hawaii, in the 20th century. This comparison shows that if Maat Mons volcano had the eruption history similar to that of Mauna Loa, the probability to observe an eruption in these VMC observation sequences would be

about 8 %, meaning that the absence of detection does not mean that Maat is not active in the present epoch.

(c) These estimates give probability to have lava field in the camera's field of view but do not consider the effect of absorption and blurring of the thermal radiation coming from Venus surface by the planet atmosphere and clouds, which decreases detectability of thermal signature of fresh lavas. To assess the role of this effect we simulated NIR images of the study area with artificially added lava flows having surface temperature 1000 K and different areas. These simulations showed that 1 km^2 lava flows should be marginally seen by VMC. Increase of the lava surface area to 2 – 3 km^2 makes them visible on the plains and increase of the area to 4 – 5 km^2 makes them visible even in deep rift zones. Elongation of lava fields in general increases these values. However, for typical length to width ratios of about 10 the decrease of contrast is not significant, but becomes significant for extremely long fields with aspect ratio more than 1000.

(d) Typical individual lava flows on Mauna Loa are a few km^2 large, however, they often have been being formed during weeks to months and the instantaneous size of the hot flow surface was usually much smaller. Thus the detection probability is significantly lower than 8 %, but it is probably far from negligible.

(e) Our consideration suggests that further search of Maat Mons and other areas including young rift zones makes sense and should be continued. More effective search could be done if observations simultaneously cover most part of the night side of Venus for relatively long (years) time of continuous observations.

In this work we used a part of VMC data and focused on investigation of differences between tessera and lowlands and search for current volcanism in vicinity of one of the most recently active volcanoes. Further analysis of the information collected by VMC surface observation campaigns might, for instance, be targeted at:

1. Look for a mineralogical difference between fresh material of impact craters' halos and surrounding areas. This might give us information about weathering rate on Venus surface.
2. Some of the rift zones looks too bright in VMC images comparing to the models based on MGN topography. It might mean that topography of these rift zones has changed since MGN survey, which would be a sign of tectonic activity. This task requires careful investigations.
3. Delicate 3-dimensional RT modelling can significantly improve emissivity retrievals for regions with complicated relief, like *e.g.* rifts.

A Misalignments in VMC surface NIR-2 images

A.1 Overview of pointing errors in VMC NIR-2 surface mosaics

VMC took several hundreds of orbit-wise mosaics of the Venus surface. For analysis of these images we compare them with model images of the surface emission. These model images were made from MGN topography data.

During the comparison we have discovered that VMC mosaics do not coincide with topography maps. There are large (up to ≈ 100 km) shifts of VMC NIR mosaics with respect to MGN topography maps. None of the mosaic are free from this problem. The amount and direction of shift with respect to MGN vary. Further investigation showed that VMC mosaic is not shifted as a whole but shifts are different for individual images from which mosaics are composed.

However, there are some systematics in the shifts:

1. In orbits, where images were taken *before* pericenter, VMC images are shifted to the *South* as compared to MGN.
2. In orbits, where images were taken *after* pericenter, VMC image are shifted to the *North* as compared to MGN.
3. Usually southern part of the mosaics is “bent” either to the West or East. In this case VMC mosaics show shift from MGN topography image in the direction that is opposite to the “bent”.

We found, that adding $\approx 15-30$ s to the image time as found in the header reduces these shifts by about a factor of ten. Thus, we tried to fix these errors by building new mosaics that are based on navigation information calculated for image time $t = t_{image} + \Delta$, where t_{image} is the value of *IMAGE_TIME* header field.

A.2 Examples of VMC NIR-2 surface mosaics with time corrections

To illustrate this behaviour let us look at some particular orbits. In figures below there are side-by-side images of VMC and model images created from MGN data with contour lines outlining particular features.

The model images were created in the following way:

1. MGN GTDR data corresponding to the area covered by VMC mosaic were extracted and transformed to the same projection as VMC mosaic.

2. Brightness of the surface was calculated assuming the base temperature at zero altitude level (735.3 K), adiabatic temperature gradient in atmosphere (−8.1 K/km) and absorption by CO_2 (it is minor factor) and black body emission of the surface.
3. Brightness map was transformed to account for atmospheric blurring and reflection from atmosphere to surface and reflection in backward direction.

A.2.1 Orbit 470

This is one of the best orbits in terms of image quality. The images were taken after the apocenter (*i.e.* spacecraft was moving from north to south). Original mosaic has a shift ≈ 70 km to the North-East (fig. A.1). The figure shows the discussed pointing problem.

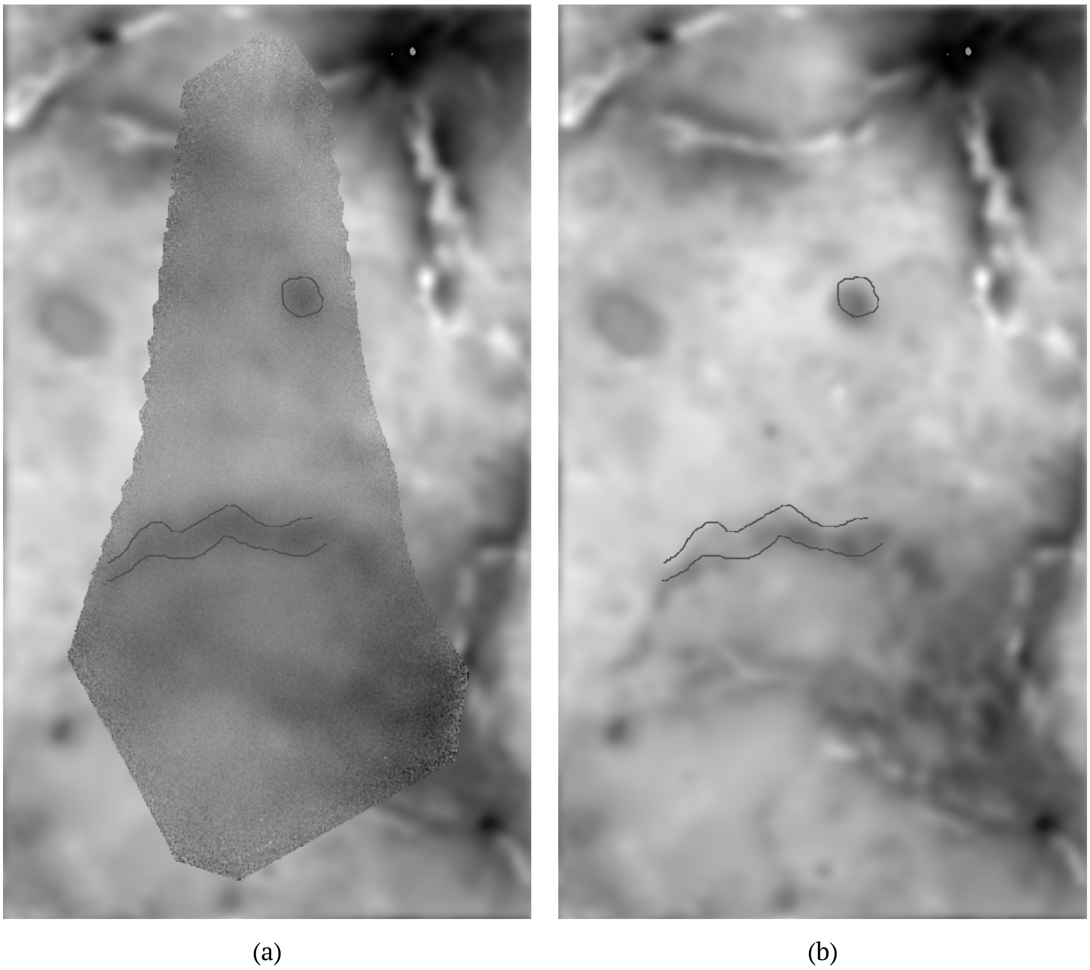
(a) (b)

Figure A.1: Orbit 0470 — original VMC mosaic on the background of model derived from MGN topography *(a)*, and the model image alone with the same features outlined *(b)*.

The next figure (A.2) shows mosaic that was made from the same images, but navigation information was calculated assuming image time is $t = t_{image} + 15$ s, (t_{image} is taken from the image header). Note that 15 s is the half of the exposure time. One can see that in this case situation is much better and misalignment became much smaller.

Let us look also at mosaics made using 20 and 30 s shifts (figs. A.3 and A.4). One can see that 30 s is too much of a correction but 20 might still be close to a good value.

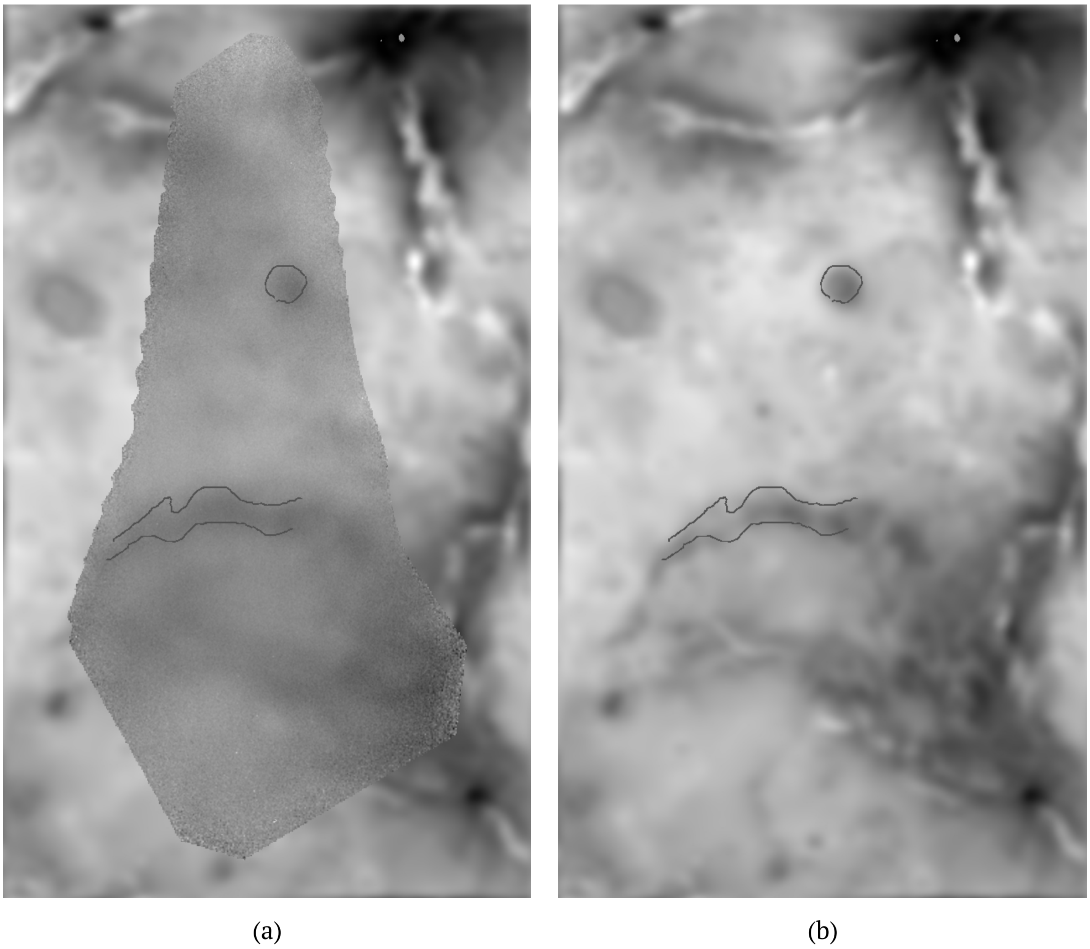
(a) (b)

Figure A.2: Orbit 0470 — VMC mosaic with images shifted in time by 15 s on the background of the model derived from MGN topography *(a)*, and the model image alone with the same features outlined *(b)*.

A.2.2 Orbit 564

The quality of this mosaic is not high, but this is one of the several mosaics that was taken before pericenter (thus spacecraft was moving from south to north). In fig. A.5 north part of the VMC mosaic is shifted to the south comparing to MGN image. After applying 15 s shift to image times (fig. A.6) north part of image looks much better. Figure A.7 shows comparison with 30 s time shift.

A.2.3 Orbit 590

This orbit covers region, close to the region mapped in orbit 470 and thus shows the same surface features (Chimon-mana tessera and Tuulikki Mons are features with most contrast). The quality of this mosaic is not high, but this is one of the several mosaics that was taken before pericenter (thus spacecraft was moving from south to north). This is opposite to orbit 470. In fig. A.8 north part of the VMC mosaic is shifted to the south comparing to MGN. After applying 15 s shift to image times (fig. A.9) image looks much better. Figure A.10 shows comparison with 30 s time shift.

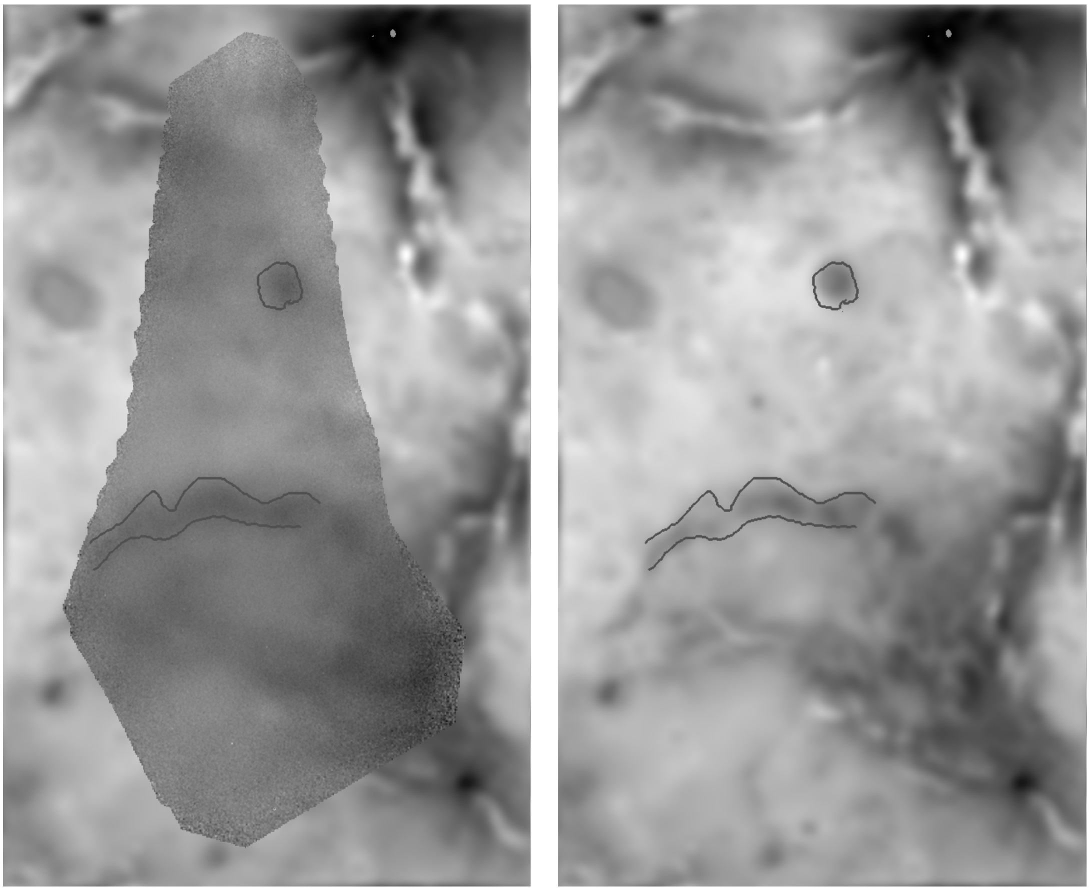
(a) (b)

Figure A.3: Orbit 0470 — VMC mosaic with images shifted in time by 20 s on the background of the model derived from MGN topography *(a)*, and the model image alone with the same features outlined *(b)*.

A.2.4 Orbit 1148

This orbit covers Maat Mons which is a clearly visible very dark spot and has a good image quality. Images were taken after the pericenter. This mosaic has a large “bent” of its southern part. Thus, one can clearly see misalignments in both North-South and West-East directions. Original image (fig. A.11) shows shift to the North-East. After applying 15 s (fig. A.12) and 30 s (fig. A.13) shifts. One can see that 30 s shift gives nearly perfect result.

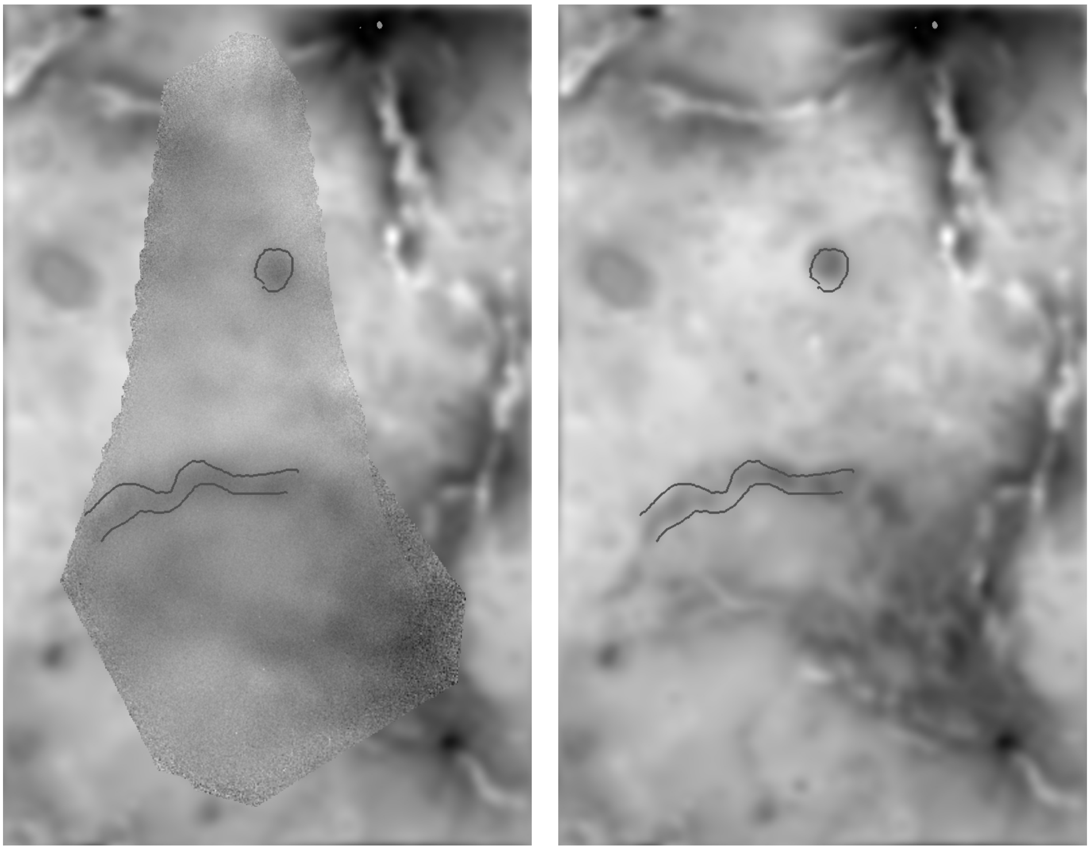
(a)
(b)

Figure A.4: Orbit 0470 — VMC mosaic with images shifted in time by 30 s on the background of the model derived from MGN topography *(a)*, and the model image alone with the same features outlined *(b)*.

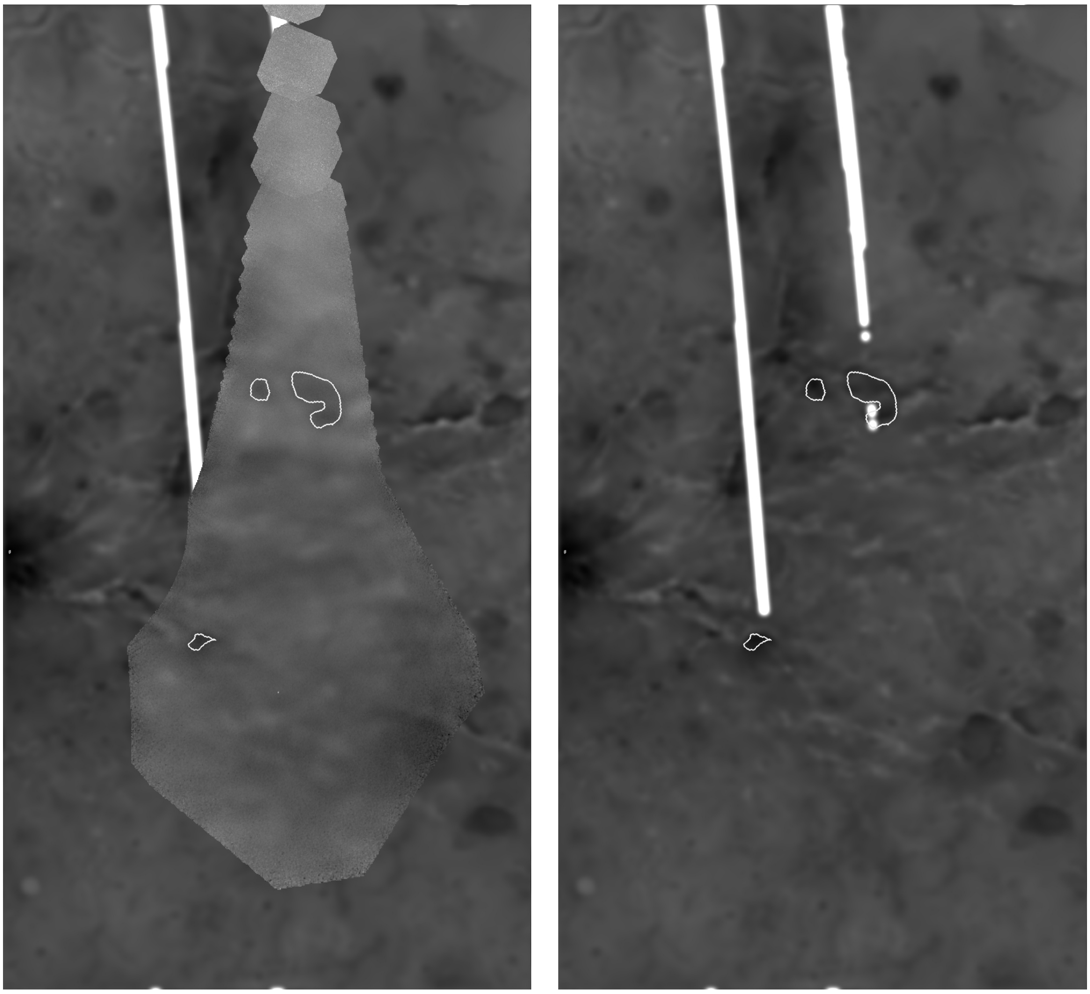
(a)

(b)

Figure A.5: Orbit 0564 — original VMC mosaic on the background of model derived from MGN topography *(a)*, and the model image alone with the same features outlined *(b)*.

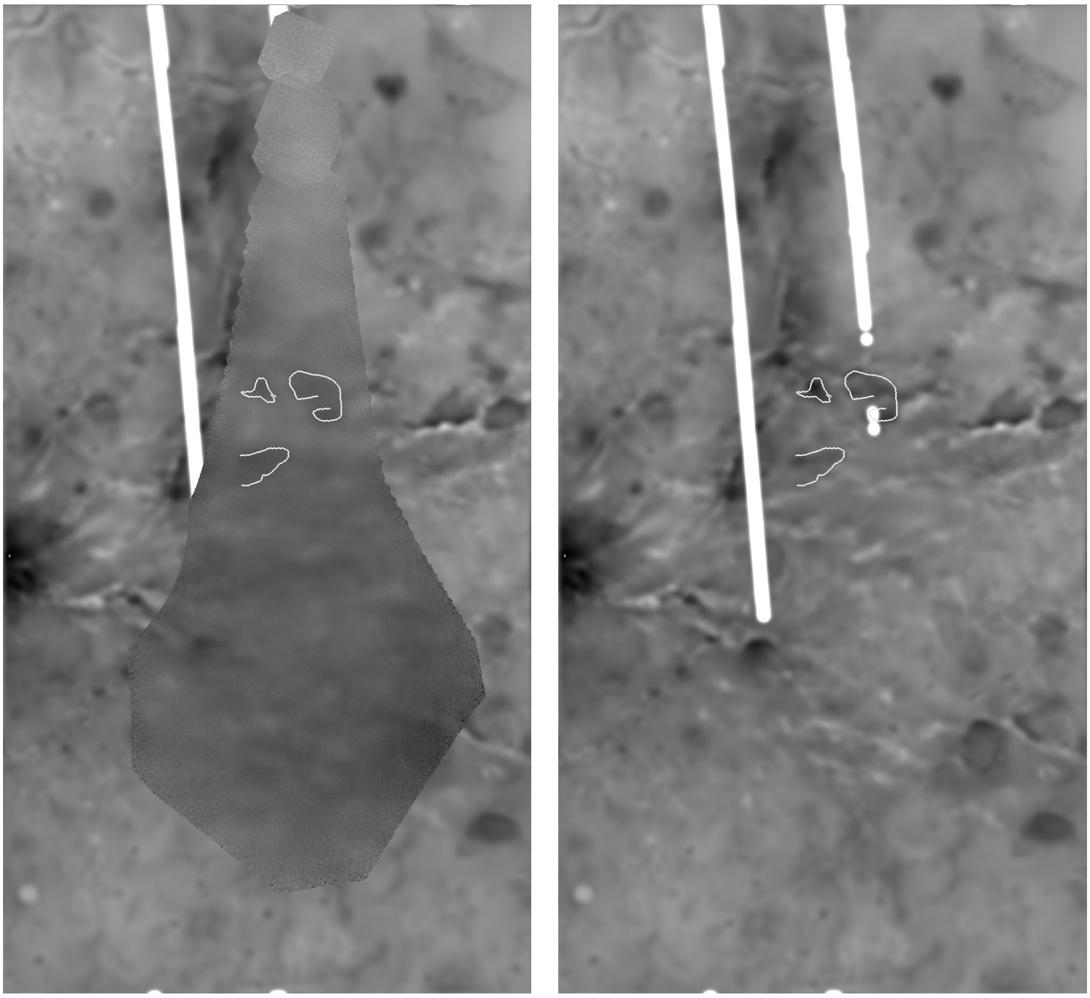

(a)

(b)

Figure A.6: Orbit 0564 — VMC mosaic with images shifted in time by 15 s on the background of the model derived from MGN topography *(a)*, and the model image alone with the same features outlined *(b)*.

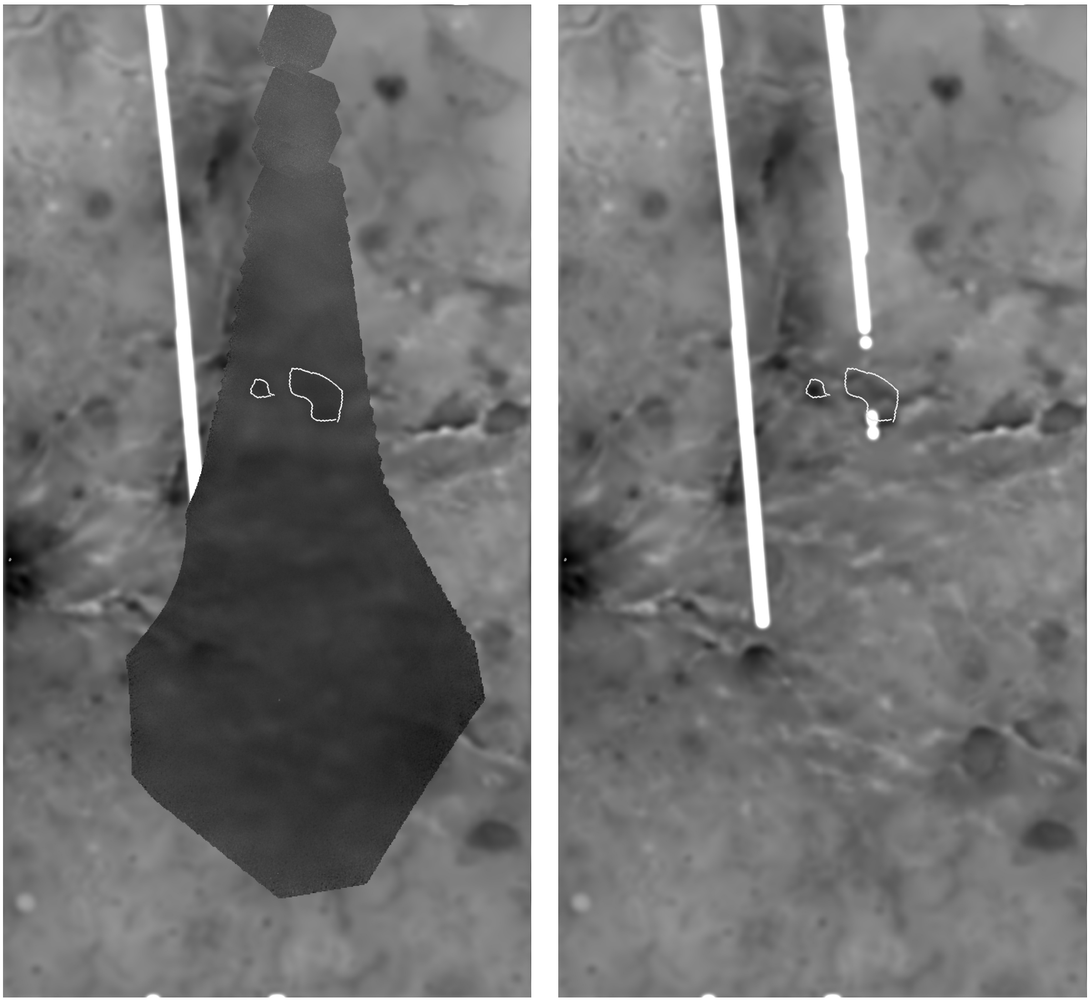

(a)

(b)

Figure A.7: Orbit 0564 — VMC mosaic with images shifted in time by 30 s on the background of the model derived from MGN topography *(a)*, and the model image alone with the same features outlined *(b)*.

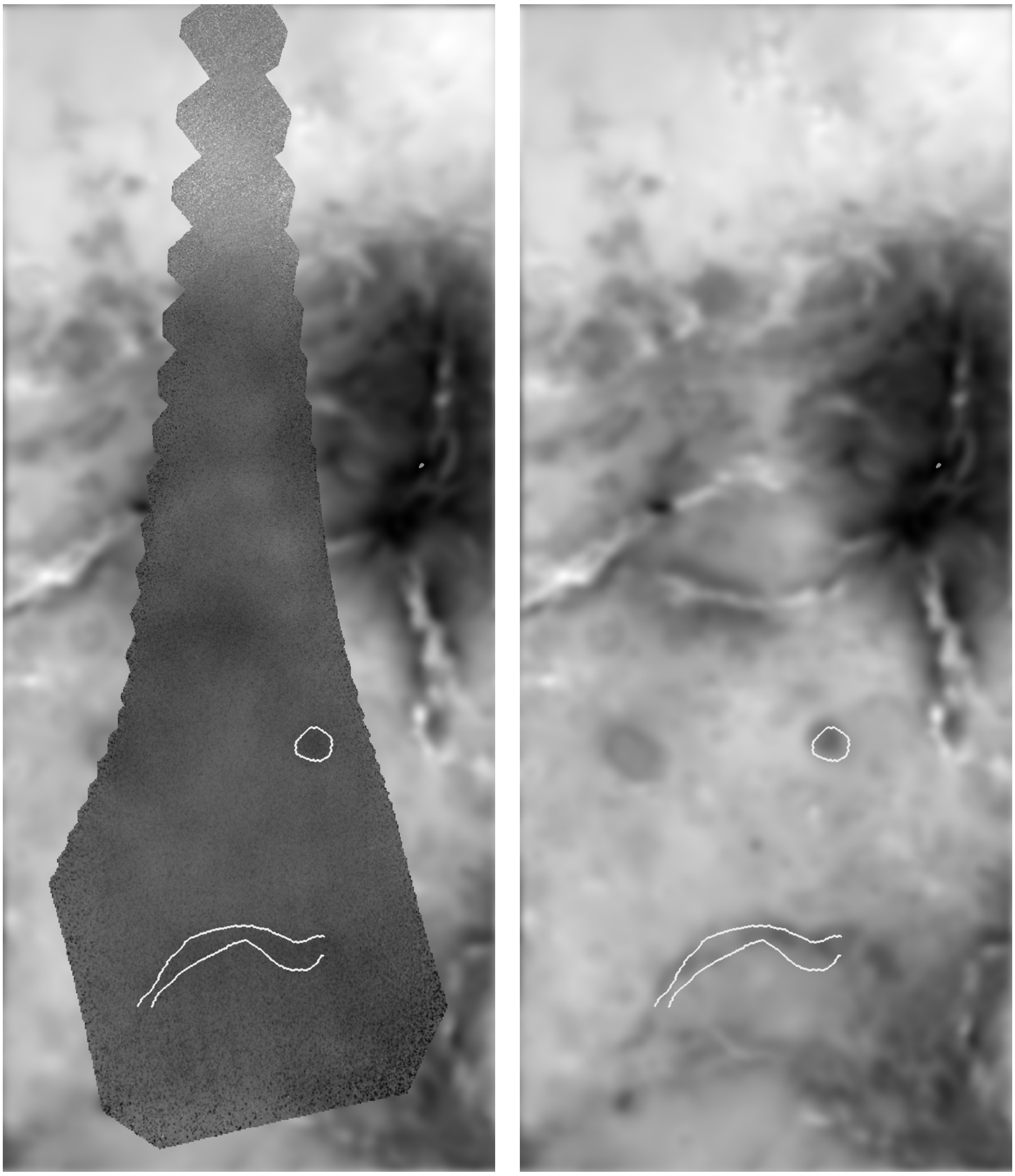

(a) (b)

Figure A.8: Orbit 0590 — original VMC mosaic on the background of model derived from MGN topography *(a)*, and the model image alone with the same features outlined *(b)*.

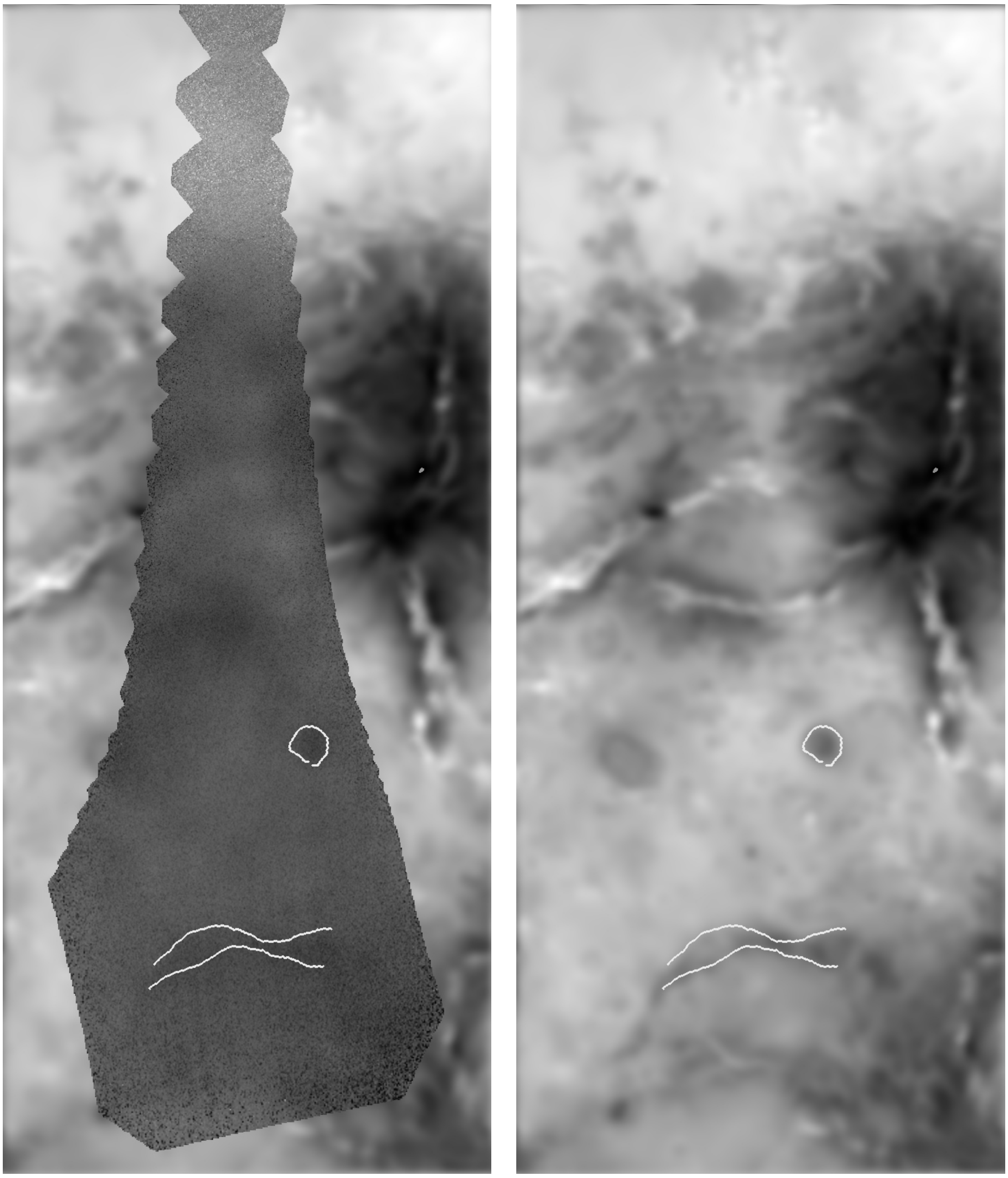

(a)

(b)

Figure A.9: Orbit 0590 — VMC mosaic with images shifted in time by 15 s on the background of the model derived from MGN topography *(a)*, and the model image alone with the same features outlined *(b)*.

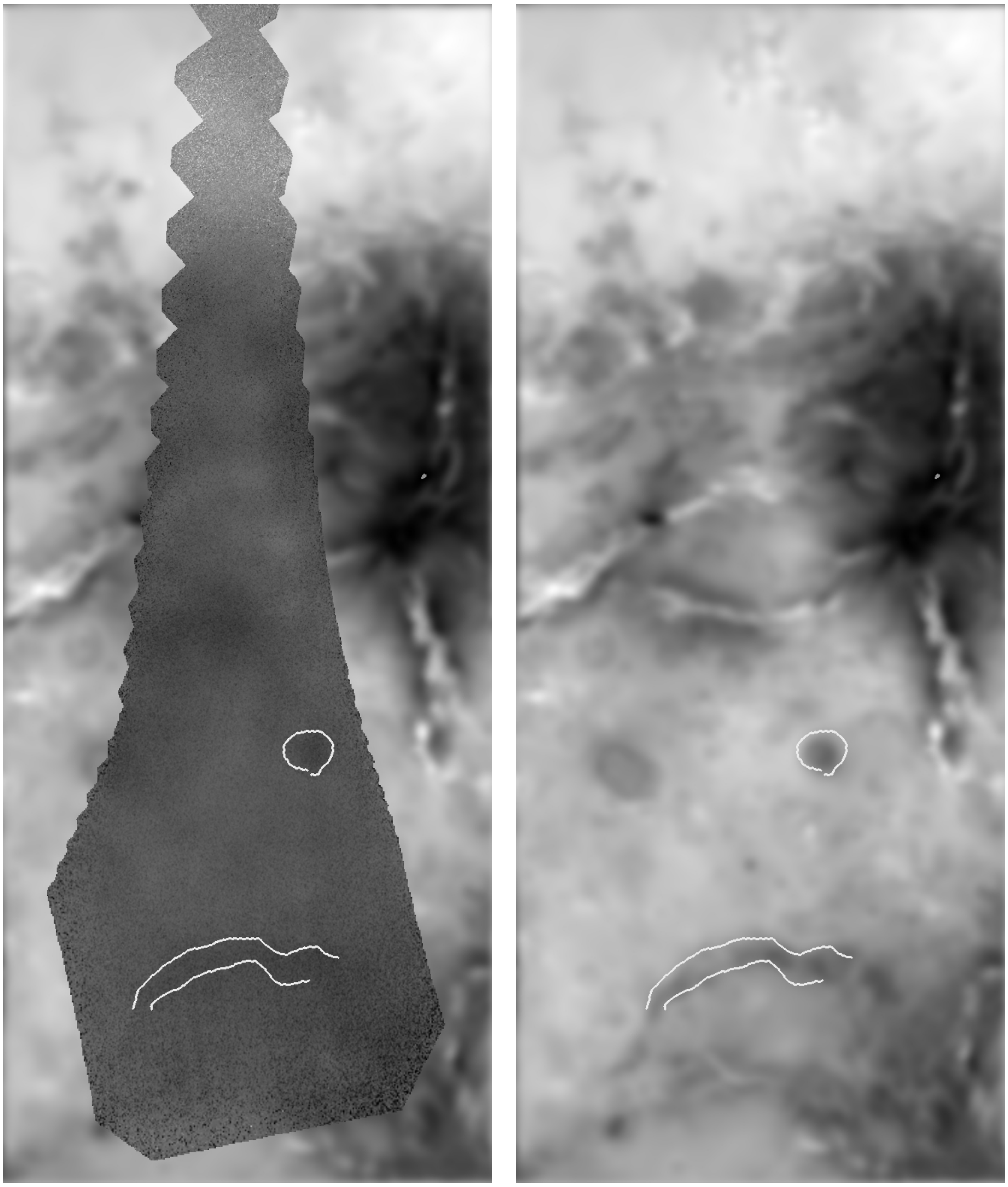

(a) (b)

Figure A.10: Orbit 0590 — VMC mosaic with images shifted in time by 30 s on the background of the model derived from MGN topography *(a)*, and the model image alone with the same features outlined *(b)*.

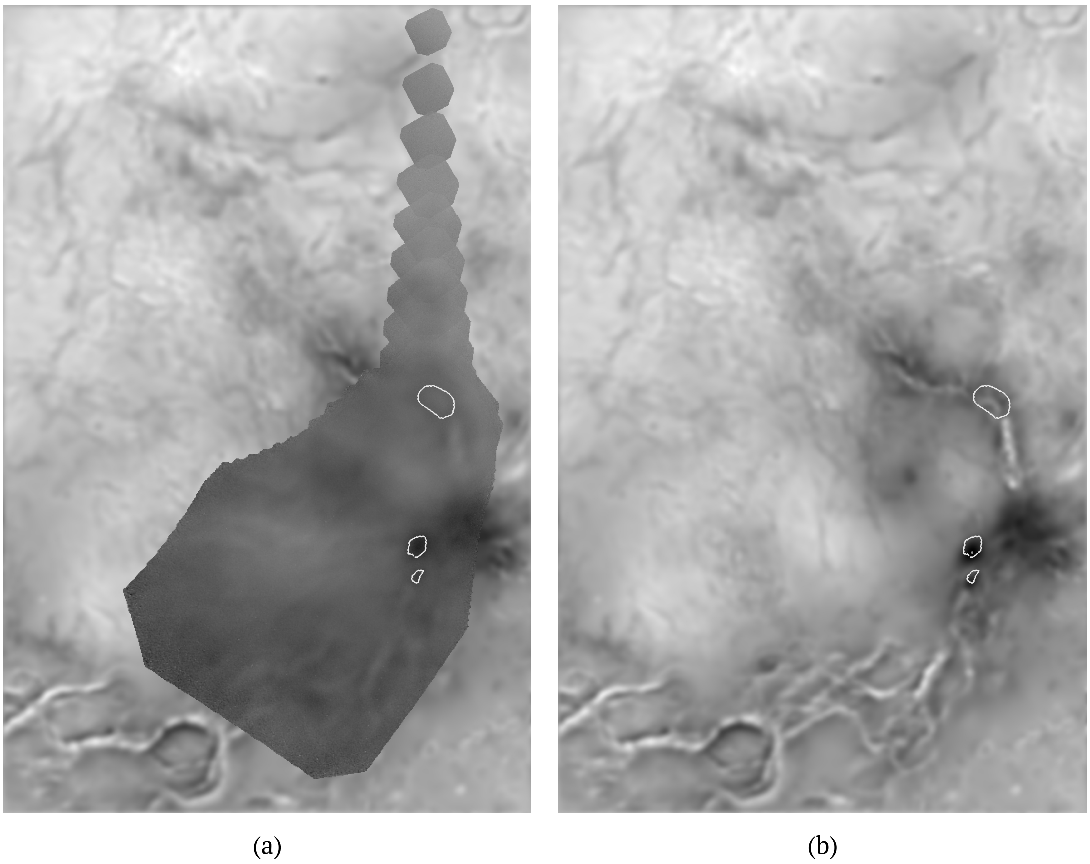

(a) (b)

Figure A.11: Orbit 1148 — original VMC mosaic on the background of model derived from MGN topography *(a)*, and the model image alone with the same features outlined *(b)*.

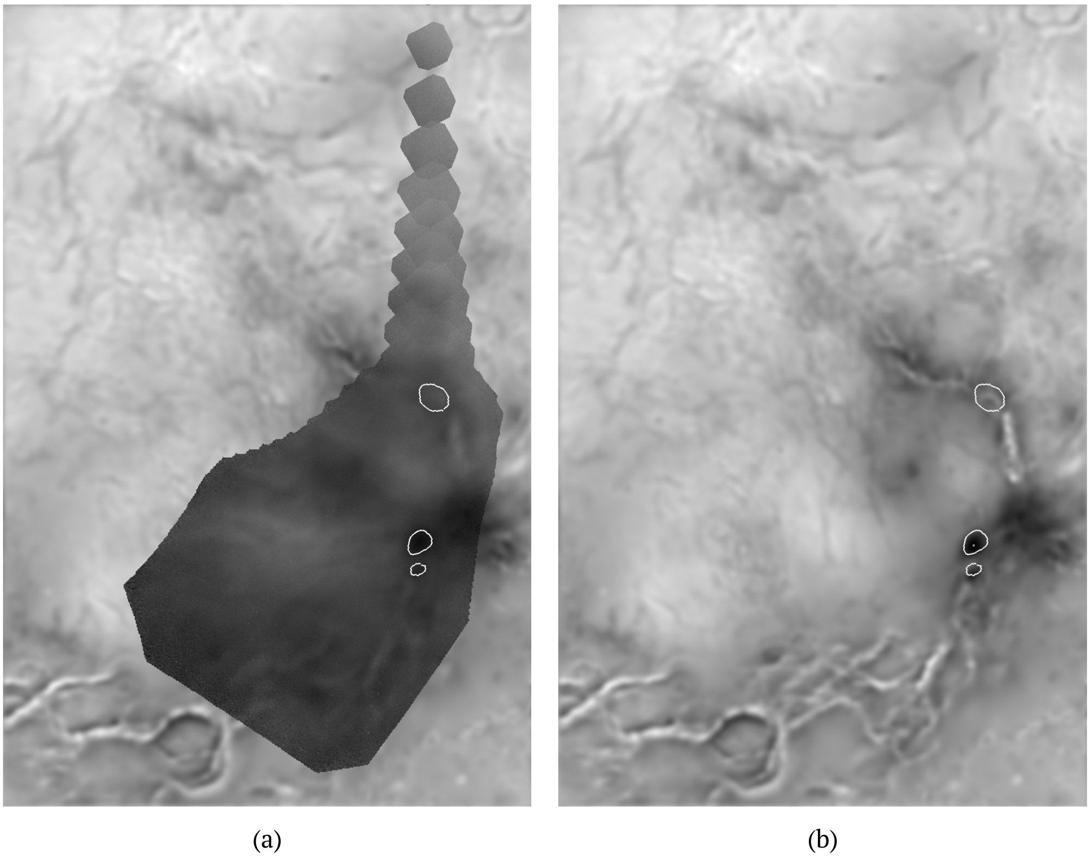
(a) (b)

Figure A.12: Orbit 1148 — VMC mosaic with images shifted in time by 15 s on the background of the model derived from MGN topography *(a)*, and the model image alone with the same features outlined *(b)*.

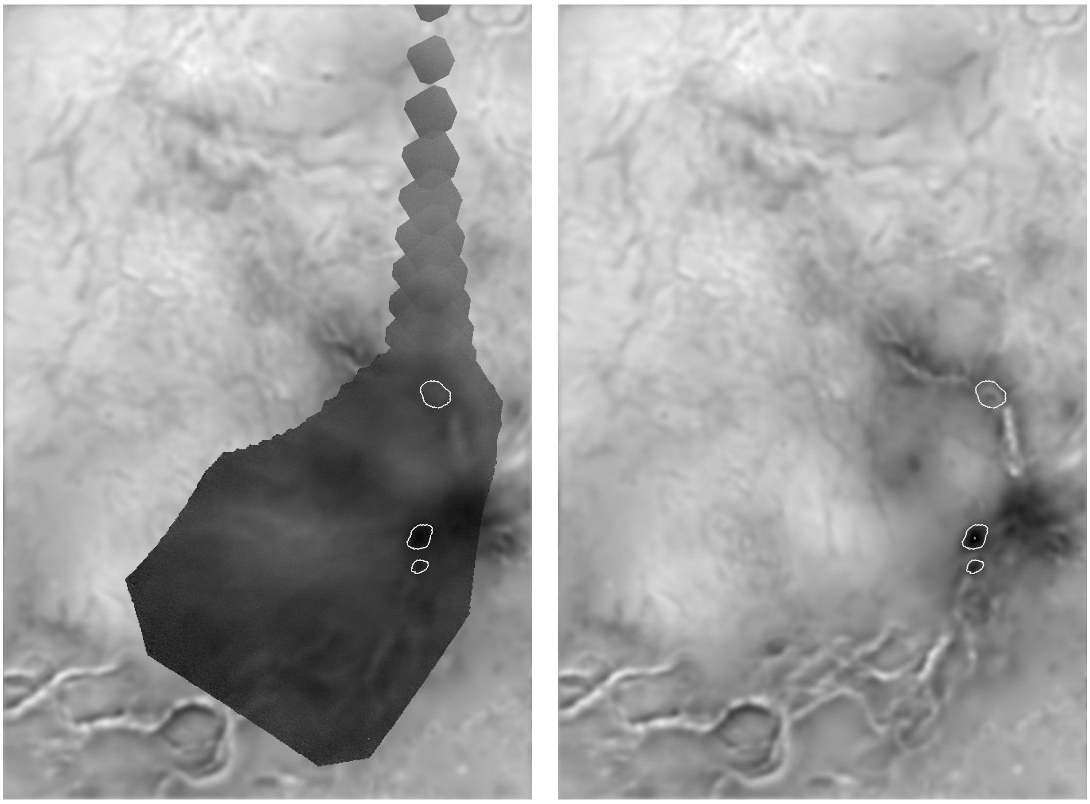

(a)

(b)

Figure A.13: Orbit 1148 — VMC mosaic with images shifted in time by 30 s on the background of the model derived from MGN topography *(a)*, and the model image alone with the same features outlined *(b)*.

A.3 Conclusions

1. VMC NIR surface mosaics show large misalignments of surface features with MGN data (tens of kilometres). Mosaics calculated for image times 15 – 30 s later than those given in the headers show significantly better agreement with models made using MGN topography.
2. Using VMC mosaics and blink comparator one can determine these time shifts with accuracy of ≈ 5 s. Obtained time shifts are usually 15 s, that is half of image exposure. But some times shift appears to be close to 30 s.
3. These changes of image times correct both North-South and West-East misalignments.

Bibliography

Abbey, W. J., M. Choukroun, A. H. Treiman, M. D. Dyar, et al. (2011). “Rock and mineral weathering experiments under model Venus conditions”. In: *Lunar and Planetary Science Conference*, p. 2165.

Abdrakhimov, A. M. (2001a). “Geologic mapping of Vega 1 landing site region”. In: *Lunar and Planetary Science Conference*. Vol. 32, p. 1700.

— (2001b). “Geologic mapping of Vega 2 landing site region”. In: *Lunar and Planetary Science Conference*. Vol. 32, p. 1719.

— (2001c). “Geologic mapping of Venera 10 landing site region”. In: *Lunar and Planetary Science Conference*. Vol. 32, p. 1632.

— (2001d). “Geologic mapping of Venera 13 landing site region”. In: *Lunar and Planetary Science Conference*. Vol. 32, p. 1653.

— (2001e). “Geologic mapping of Venera 14 landing site region”. In: *Lunar and Planetary Science Conference*. Vol. 32, p. 1670.

— (2001f). “Geologic mapping of Venera 9 landing site region”. In: *Lunar and Planetary Science Conference*. Vol. 32, p. 1601.

Adams, W. S. and T. Dunham Jr (1932). “Absorption bands in the infra-red spectrum of Venus”. In: *Publications of the Astronomical Society of the Pacific* 44, pp. 243–245.

Allen, D. A. and J. W. Crawford (1984). “Cloud structure on the dark side of Venus”. In: *Nature* 307, pp. 222–224.

Arnold, G., R. Haus, D. Kappel, P. Drossart, and G.Piccioni (Oct. 7, 2008). “Venus surface data extraction from VIRTIS/Venus Express measurements: Estimation of a quantitative approach”. In: *Journal of Geophysical Research* 113.E5, E00B10. DOI: 10.1029/2008JE003087.

Avduevskii, V. S., S. L. Vishnevetskii, I. A. Golov, I. Karpeiskii, et al. (1976). “Measurement of wind velocity on the surface of Venus during operation of the Venera 9 and Venera 10 space probes”. In: *Kosmicheskie Issledovaniia* 14, pp. 710–713.

Avduevsky, V. S., M. Y. Marov, and M. K. Rozhdestvensky (1970). “A Tentative Model of the Venus Atmosphere Based on the Measurements of Veneras 5 and 6.” In: *Journal of the Atmospheric Sciences* 27, pp. 561–568.

Baines, K. H., S. Atreya, R. W. Carlson, D. Crisp, et al. (2006). “To the depths of Venus: Exploring the deep atmosphere and surface of our sister world with Venus Express”. In: *Planetary and Space Science* 54.13-14, pp. 1263–1278.

Baldridge, A. M., S. J. Hook, C. I. Grove, and G. Rivera (2009). “The ASTER spectral library version 2.0”. In: *Remote Sensing of the Environment* 113.4, pp. 711–715. DOI: 10.1016/j.rse.2008.11.007.

Barabash, S., J. A. Sauvaud, H. Gunell, H. Andersson, et al. (2007). “The analyser of space plasmas and energetic atoms (ASPERA-4) for the Venus Express mission”. In: *Planetary and Space Science* 55.12, pp. 1772–1792.

Barsukov, V. L., A. T. Basilevsky, G. A. Burba, N. N. Bobinna, et al. (1986). “The geology and geomorphology of the Venus surface as revealed by the radar images obtained by Veneras 15 and 16”. In: *Journal of Geophysical Research* 91.B4, pp. D378–D398.

Barsukov, V. L., V. P. Volkov, and I. L. Khodakovskii (1980). “The mineral composition of Venus surface rocks - A preliminary prediction”. In: *Lunar and Planetary Science Conference*. Ed. by S. A. Bedini. Vol. 1. Lunar and Planetary Science Conference. New York: Pergamon Press, pp. 765–773.

— (1982). “The crust of Venus-Theoretical models of chemical and mineral composition”. In: *Lunar and Planetary Science Conference*. Vol. 13, p. 3.

Basilevsky, A. T. (1993). “Age of rifting and associated volcanism in Atla Regio, Venus”. In: *Geophysical Research Letters* 20.10, pp. 883–886.

Basilevsky, A. T. and J. W. Head (1998). “The geologic history of Venus- A stratigraphic view”. In: *Journal of Geophysical Research* 103.E4, pp. 8531–8544.

— (2000). “Geologic units on Venus: Evidence for their global correlation”. In: *Planetary and Space Science* 48.1, pp. 75–111.

— (2002a). “Venus: Analysis of the degree of impact crater deposit degradation and assessment of its use for dating geological units and features”. In: *Journal of Geophysical Research* 107.E8, p. 5061.

— (2002b). “Venus: Timing and rates of geologic activity”. In: *Geology* 30.11, pp. 1015–1018.

— (2007). “Beta Regio, Venus: Evidence for uplift, rifting, and volcanism due to a mantle plume”. In: *Icarus* 192.1, pp. 167–186.

Basilevsky, A. T., J. W. Head, and A. M. Abdrakhimov (2004). “Impact crater air fall deposits on the surface of Venus: Areal distribution, estimated thickness, recognition in surface panoramas, and implications for provenance of sampled surface materials”. In: *Journal of Geophysical Research* 109, E12003. DOI: 10.1029/2004JE002307.

Basilevsky, A. T., J. W. Head, and I. V. Setyaeva (Sept. 25, 2003). “Venus: Estimation of age of impact craters on the basis of degree of preservation of associated radar-dark deposits”. In: *Geophysical Research Letters* 30.18, p. 1950. DOI: 10.1029/2003GL017504.

Basilevsky, A. T., M. A. Ivanov, J. W. Head, M. Aittola, and J. Raitala (2007). “Landing on Venus: Past and future”. In: *Planetary and Space Science* 55.14, pp. 2097–2112.

Basilevsky, A. T., R. O. Kuzmin, O. V. Nikolaeva, A. A. Pronin, et al. (1985). “The surface of Venus as revealed by the Venera landings: Part II”. In: *Bulletin of the Geological Society of America* 96.1, pp. 137–144.

Basilevsky, A. T. and G. E. McGill (2007). “Surface Evolution of Venus”. In: *Geophysical monograph* 176, pp. 23–43.

Bertaux, J. L., D. Nevejans, O. Korablev, E. Villard, et al. (2007). “SPICAV on Venus Express: Three spectrometers to study the global structure and composition of the Venus atmosphere”. In: *Planetary and Space Science* 55.12, pp. 1673–1700.

Bondarenko, N. V. and J. W. Head (2009). “Crater-associated dark diffuse features on Venus: Properties of surficial deposits and their evolution”. In: *Journal of Geophysical Research* 114.E3, E03004.

Bondarenko, N. V., J. W. Head, and M. A. Ivanov (Dec. 8, 2010). “Present-Day Volcanism on Venus: Evidence from Microwave Radiometry”. In: *Geophysical Research Letters* 37.23, p. L23202. DOI: 10.1029/2010GL045233.

Bougher, S. W. et al., eds. (1997). *Venus II: Geology, Geophysics, Atmosphere, and Solar Wind Environment*. Vol. 1. Venus. Tucson: Univ. of Ariz. Press.

Bridges, N. T. (1995). “Submarine analogs to Venusian pancake domes”. In: *Geophysical Research Letters* 22.20, pp. 2781–2784.

Burns, R. G. (1970). “Crystal field spectra and evidence of cation ordering in olivine minerals”. In: *Am. Mineral* 55, pp. 1608–1632.

— (1993). “Origin of electronic spectra of minerals in the visible to near-infrared region”. In: *Remote Geochemical Analysis: Elemental and Mineralogical Composition*. Ed. by C. M. Pieters and P. A. J. Englert. Vol. 4. Cambridge Univ. Press, pp. 3–29.

Campbell, D. B., N. J. S. Stacy, W. I. Newman, R. E. Arvidson, et al. (1992). “Magellan observations of extended impact crater related features on the surface of Venus”. In: *Journal of Geophysical Research* 97.E10, pp. 16249–16277.

Clancy, R. T. and D. O. Muhleman (1991). “Long-term (1979–1990) changes in the thermal, dynamical, and compositional structure of the Venus Mesosphere as inferred from microwave spectral line observations of 12CO, 13CO, and C18O”. In: *Icarus* 89.1, pp. 129–146. DOI: 10.1016/0019-1035(91)90093-9.

Clark, B. G. and A. D. Kuz’min (July 1965). “The Measurement of the Polarization and Brightness Distribution of Venus at 10.6-cm Wavelength.” In: *Astrophysical Journal* 142, pp. 23–44. DOI: 10.1086/148261.

Coffeen, D. L. and T. Gehrels (1969). “Wavelength dependence of polarization. XV. Observations of Venus”. In: *Astronomical Journal* 74, pp. 433–445.

Crumpler, L. S., J. C. Aubele, D. A. Senske, S. T. Keddie, K. P. Magee, and J. W. Head (1997). “Volcanoes and centers of volcanism on Venus”. In: *Venus II: Geology, Geophysics, Atmosphere, and Solar Wind Environment*. Ed. by S. W. Bougher et al. Vol. 1. Venus. Tucson: Univ. of Ariz. Press, pp. 697–756.

Dollfus, A. and D. L. Coffeen (1970). “Polarization of Venus. I. Disk Observations”. In: *Astronomy and Astrophysics* 8, p. 251.

Drossart, P., G. Piccioni, A. Adriani, F. Angrilli, et al. (2007). “Scientific goals for the observation of Venus by VIRTIS on ESA/Venus Express mission”. In: *Planetary and Space Science* 55.12, pp. 1653–1672.

Ekonomov, A. P., Y. M. Golovin, and B. E. Moshkin (1980). “Visible radiation observed near the surface of Venus: Results and their interpretation”. In: *Icarus* 41.1, pp. 65–75.

Esposito, L. W. (1984). “Sulfur Dioxide: Episodic Injection Shows Evidence for Active Venus Volcanism”. In: *Science* 223.4640, pp. 1072–1074. DOI: 10.1126/science.223.4640.1072. eprint: http://www.sciencemag.org/content/223/4640/1072.full.pdf.

Esposito, L. W., M. Copley, R. Eckert, L. Gates, A. I. F. Stewart, and H. Worden (1988). “Sulfur Dioxide at the Venus Cloud Tops, 1978–1986”. In: *Journal of Geophysical Research* 93.D5, pp. 5267–5276. DOI: 10.1029/JD093iD05p05267.

Fegley Jr., B. (2003). “Venus”. In: *Treatise on Geochemistry*. Ed. by H. D. Holland and K. K. Turekian. Oxford: Pergamon, pp. 487–507. DOI: 10.1016/B0-08-043751-6/01150-6.

Fegley, B., G. Klingelhofer, R. A. Brackett, N. Izenberg, D. T. Kremser, and K. Lodders (1995). “Basalt Oxidation and the Formation of Hematite on the Surface of Venus”. In: *Icarus* 118.2, pp. 373–383. DOI: 10.1006/icar.1995.1197.

Fegley, B., K. Lodders, A. H. Treiman, and G. Klingelhöfer (1995). “The Rate of Pyrite Decomposition on the Surface of Venus”. In: *Icarus* 115.1, pp. 159–180. DOI: 10.1006/icar.1995.1086.

Fegley, B. and R. G. Prinn (1989). “Estimation of the rate of volcanism on Venus from reaction rate measurements”. In: *Nature* 337.6202, pp. 55–58.

Fink, J. H. and R. W. Griffiths (1998). “Morphology, eruption rates, and rheology of lava domes: Insights from laboratory models”. In: *Journal of Geophysical Research* 103.B1, pp. 527–545.

Florensky, C. P., L. B. Ronca, and A. T. Basilevsky (1977). “Geomorphic degradations on the surface of Venus: an analysis of Venera 9 and Venera 10 data”. In: *Science* 196.4292, pp. 869–871.

Flynn, L. P. and P. J. Mouginis-Mark (1992). “Cooling rate of an active Hawaiian lava flow from nighttime spectroradiometer measurements”. In: *Geophysical Research Letters* 19.17, pp. 1783–1786. DOI: 10.1029/92GL01577.

Ford, P. G. and G. H. Pettengill (1992). “Venus topography and kilometer-scale slopes”. In: *Journal of Geophysical Research* 97.E8, pp. 13103–13114.

Formisano, V., F. Angrilli, G. Arnold, S. Atreya, et al. (2006). “The planetary fourier spectrometer (PFS) onboard the European Venus Express mission”. In: *Planetary and Space Science* 54.13, pp. 1298–1314.

Gilmore, M. S., N. Mueller, and J. Helbert (2011). “VIRTIS emissivity of Alpha Regio tessera”. In: *Lunar and Planetary Science Conference*. Vol. 42, p. 1498.

Gilmore, M. S., P. G. Resor, R. Ghent, D. A. Senske, and R. R. Herrick (2011). “Constraints on tessera composition from modeling of Tellus Regio”. In: *Lunar and Planetary Science Conference*. Vol. 42, p. 2053.

Goldstein, R., R. Stevens, and W. K. Victor (1965). “Radar Exploration of Venus: Goldstone Observatory Report Oct.-Dec. 1962”. In:

Greeley, R., K. C. Bender, R. S. Saunders, G. Schubert, and R. A. Simpson (1997). “Aeolian processes and features on Venus”. In: *Venus II: Geology, Geophysics, Atmosphere, and Solar Wind Environment*. Ed. by S. W. Bougher et al. Vol. 1. Venus. Tucson: Univ. of Ariz. Press, pp. 547–589.

Grinspoon, D. H. and M. A. Bullock (2003). “Did Venus Experience One Great Transition or Two?” In: *American Astronomical Society, DPS meeting #35, #44.03; Bulletin of the American Astronomical Society*. Vol. 35, p. 1007.

Hansen, J. E. and J. W. Hovenier (May 1974). “Interpretation of the polarization of Venus.” In: *Journal of the Atmospheric Sciences* 31, pp. 1137–1160. DOI: 10.1175/1520-0469(1974)031<1137:IOTPOV>2.0.CO;2.

Hashimoto, G. L. and T. Imamura (2001). “Elucidating the rate of volcanism on Venus: Detection of lava eruptions using near-infrared observations”. In: *Icarus* 154.2, pp. 239–243.

Hashimoto, G. L., M. Roos-Serote, S. Sugita, M. S. Gilmore, et al. (Dec. 31, 2008). “Felsic highland crust on Venus suggested by Galileo Near-Infrared Mapping Spectrometer data”. In: *Journal of Geophysical Research* 113.E5, E00B24. DOI: 10.1029/2008JE003134.

Haus, R. and G. Arnold (2010). “Radiative transfer in the atmosphere of Venus and application to surface emissivity retrieval from VIRTIS/VEX measurements”. In: *Planetary and Space Science* 58.12, pp. 1578–1598. DOI: 10.1016/j.pss.2010.08.001.

Häusler, B., M. Pätzold, G. L. Tyler, R. A. Simpson, et al. (2006). “Radio science investigations by VeRa onboard the Venus Express spacecraft”. In: *Planetary and Space Science* 54.13–14, pp. 1315–1335. DOI: 10.1016/j.pss.2006.04.032.

Head III, J. W. and L. Wilson (1986). “Volcanic processes and landforms on Venus: Theory, predictions, and observations”. In: *Journal of Geophysical Research* 91.B9, pp. 9407–9446.

Head, J. W., L. S. Crumpler, J. C. Aubele, J. E. Guest, and R. S. Saunders (1992). “Venus volcanism: Classification of volcanic features and structures, associations, and global distribution from Magellan data”. In: *Journal of Geophysical Research* 97.E8, pp. 13153–13197.

Helbert, J., L. V. Moroz, A. Maturilli, A. Bischoff, et al. (2007). “A set of laboratory analogue materials for the MERTIS instrument on the ESA BepiColombo mission to Mercury”. In: *Advances in Space Research* 40.2, pp. 272–279.

Helbert, J., N. Müller, P. Kostama, L. Marinangeli, G. Piccioni, and P. Drossart (2008). “Surface brightness variations seen by VIRTIS on Venus Express and implications for the evolution of the Lada Terra region, Venus”. In: *Geophysical Research Letters* 35.11, p. L11201.

Herrick, R. R. and M. H. Price (n.d.). *It's a Dry Heat: The Geology of Venus from Magellan*. Lunar and Planetary Institute. URL: http://www.lpi.usra.edu/publications/slidesets/venus/index.shtml.

Hinrichs, J. L. and P. G. Lucey (2002). “Temperature-dependent near-infrared spectral properties of minerals, meteorites, and lunar soil”. In: *Icarus* 155.1, pp. 169–180.

Hunten, D. M. et al., eds. (1983). *Venus*. Vol. 1. Tucson: Univ. of Arizona Press.

Ignatiev, N. I., D. V. Titov, G. Piccioni, P. Drossart, et al. (2009). “Altimetry of the Venus cloud tops from the Venus Express observations”. In: *Journal of Geophysical Research* 114.E9, E00B43.

Ignatiev, N. I. (2008). *VMC in-flight calibration report*. Tech. rep. MPS.

— (Nov. 2012). *VMC in-flight calibration report*. Tech. rep. MPS.

Irvine, W. M. (1968). “Monochromatic phase curves and albedos for Venus (Monochromatic phase curves and albedos from photoelectric observations of Venus)”. In: *Journal of the Atmospheric Sciences* 25, pp. 610–616.

Ivanov, B. A., I. V. Nemchinov, V. A. Svetsov, A. A. Provalov, V. M. Khazins, and R. J. Phillips (1992). “Impact cratering on Venus: Physical and mechanical models”. In: *Journal of Geophysical Research* 97.E10, pp. 16167–16181.

Ivanov, M. A. (2001). “Morphology of the tessera terrain on Venus: implications for the composition of tessera material”. In: *Solar System Research* 35.1, pp. 1–17.

— (2008). “Global geological map of Venus: preliminary results”. In: *Lunar and Planetary Science Conference*. Vol. 39, p. 1017.

Ivanov, M. A. and A. T. Basilevsky (1993). “Density and morphology of impact craters on tessera terrain, Venus”. In: *Geophysical Research Letters* 20.23, pp. 2579–2582.

Ivanov, M. A. and J. W. Head (1996). “Tessera terrain on Venus: A survey of the global distribution, characteristics, and relation to surrounding units from Magellan data”. In: *Journal of Geophysical Research* 101.E6, pp. 14861–14908.

Ivanov, M. A. and J. W. Head (2011). “Global geological map of Venus”. In: *Planetary and Space Science* 59.13, pp. 1559–1600. DOI: 10.1016/j.pss.2011.07.008.

Johnson, N. M., B. Fegley, et al. (2003). “Longevity of fluorine-bearing tremolite on Venus”. In: *Icarus* 165.2, pp. 340–348.

Kasting, J. F. (1988). “Runaway and moist greenhouse atmospheres and the evolution of Earth and Venus”. In: *Icarus* 74.3, pp. 472–494.

Kasting, J. F., J. B. Pollack, and T. P. Ackerman (1984). “Response of Earth’s atmosphere to increases in solar flux and implications for loss of water from Venus”. In: *Icarus* 57.3, pp. 335–355.

Kawabata, K., D. L. Coffeen, J. E. Hansen, W. A. Lane, M. Sato, and L. D. Travis (1980). “Cloud and haze properties from Pioneer Venus polarimetry”. In: *Journal of Geophysical Research* 85.A13, pp. 8129–8140.

Kawabata, K. and J. E. Hansen (June 1975). “Interpretation of the variation of polarization over the disk of Venus”. In: *Journal of the Atmospheric Sciences* 32, pp. 1133–1139. DOI: 10.1175/1520-0469(1975)032<1133:IOTVOP>2.0.CO;2.

Kemurdzhian, A. L., P. N. Brodskii, V. V. Gromov, V. P. Grushin, et al. (1983). “Preliminary results of determining the physical and mechanical properties of the soil of Venus by the Soviet automatic stations Venera 13 and Venera 14”. In: *Kosm. Issled* 21, pp. 323–330.

Kerzhanovich, V. V. and M. I. Marov (1983). “The atmospheric dynamics of Venus according to Doppler measurements by the Venera entry probes”. In: *Venus*. Ed. by D. M. Hunten et al. Vol. 1. Tucson: Univ. of Arizona Press, pp. 766–778.

Kerzhanovich, V. V., M. Y. Marov, and V. I. Moroz (1983). “Proposals for VIRA (Venus International Reference Atmosphere): Dynamics and structure below 100 KM”. In: *NASA STI/Recon Technical Report N* 84, p. 21475.

Kilburn, C. R. J. (2000). “Encyclopedia of Volcanism”. In: ed. by H. Sigurdsson et al. Academic Press. Chap. Lava flows and flow fields, pp. 291–308.

Kliore, A., V. I. Moroz, and G. M. Keating (1986). *The Venus international reference atmosphere*. Vol. 5. Pergamon.

Klose, K. B., J. A. Wood, and A. Hashimoto (1992). “Mineral equilibria and the high radar reflectivity of Venus mountaintops”. In: *Journal of Geophysical Research* 97.E10, pp. 16353–16369.

Knollenberg, R. G. and D. M. Hunten (1979). “Clouds of Venus: particle size distribution measurements.” In: *Science* 203.4382, pp. 792–795.

— (1980). “The microphysics of the clouds of Venus: Results of the Pioneer Venus particle size spectrometer experiment”. In: *Journal of Geophysical Research* 85.A13, pp. 8039–8058.

Kotel’nikov, V. A., Y. N. Aleksandrov, L. V. Apraksin, V. M. Dubrovin, et al. (Jan. 1966). “Radar Observations of Venus in the Soviet Union in 1964”. In: *Soviet Physics Doklady* 10, p. 578.

Krasnopolsky, V. A. (2012). “A photochemical model for the Venus atmosphere at 47–112 km”. In: *Icarus* 218.1, pp. 230–246. DOI: 10.1016/j.icarus.2011.11.012.

Ksanfomality, L., N. V. Goroschkova, and V. Khondryev (1983). “Wind Velocity near the surface of Venus from Acoustic Measurements”. In: *Cosmic Research* 21, pp. 161–167.

Kucinskas, A. B., D. L. Turcotte, and J. Arkani-Hamed (1996). “Isostatic compensation of Ishtar Terra, Venus”. In: *Journal of Geophysical Research* 101.E2, pp. 4725–4736.

Kuz’min, A. D. and M. Y. Marov (Dec. 1974). *Physics of the planet Venus*. Russian. Ed. by V. A. Bronshten. Moscow: Nauka. 408 pp.

Kuz’min, A. D. and A. E. Salomonovich (1961). “Radio Observations of Venus in 1961”. In: *Astronomicheskii Zhurnal* 38, p. 1115.

Lecacheux, J., P. Drossart, P. Laques, F. Deladerriére, and F. Colas (1993). “Detection of the surface of Venus at 1.0µm from ground-based observations”. In: *Planetary and Space Science* 41.7. <ce:title>Special Issue: The Galileo Venus Encounter: NIMS Results</ce:title>, pp. 543–549. DOI: 10.1016/0032-0633(93)90035-Z.

Leeder, M. R. (2007). “New criterion for sediment suspension and wind-speed proxy in planetary atmospheres”. In: *Geophysical Research Letters* 34.1, p. L01201.

Lockwood, J. P. and P. W. Lipman (1987). “Volcanism in Hawaii: U.S. Geological Survey Professional Paper 1350”. In: ed. by R. W. Decker, T. L. Wright, and P. H. Stauffer. Chap. Holocene eruptive history of Mauna Loa Volcano.

Lyot, B. (1929). *Recherches sur la polarisation de la lumiére des planétes et de quelques substances terrestres*. Vol. 8. available in English as NASA TT. F-187 1964, p. 161.

Magee, K. P. and J. W. Head (2001). “Large flow fields on Venus: Implications for plumes, rift associations, and resurfacing”. In: *Mantle Plumes: Their Identification Through Time*, pp. 81–101.

Marcq, E., D. Belyaev, F. Montmessin, A. Fedorova, et al. (2011). “An investigation of the SO2 content of the venusian mesosphere using SPICAV-UV in nadir mode”. In: *Icarus* 211.1, pp. 58–69. DOI: 10.1016/j.icarus.2010.08.021.

Markiewicz, W. J., D. V. Titov, B. Fiethe, T. Behnke, et al. (2008). “Venus Monitoring Camera for Venus Express”. In: *ESA SP-1295*. Noordwijk, The Netherlands.

Markiewicz, W. J., D. V. Titov, N. I. Ignatiev, H. Keller, et al. (2007). “Venus monitoring camera for Venus Express”. In: *Planetary and Space Science* 55.12, pp. 1701–1711.

Marov, M. Y., V. S. Avduevsky, N. F. Borodin, A. P. Ekonomov, et al. (1973). “Preliminary results on the Venus atmosphere from the Venera 8 descent module”. In: *Icarus* 20.4, pp. 407–421.

Mayer, C. H., T. P. McCullough, and R. M. Sloanaker (Jan. 1958). “Observations of Venus at 3.15-CM Wave Length.” In: *Astrophysical Journal* 127, p. 1. DOI: 10.1086/146433.

McBirney, A. (2006). *Igneous Petrology*. 3rd. Jones and Bartlett Learning, p. 508.

McKinnon, W. B., K. J. Zahnle, B. A. Ivanov, and H. J. Melosh (1997). “Cratering on Venus: Models and observations”. In: *Venus II: Geology, Geophysics, Atmosphere, and Solar Wind Environment*. Ed. by S. W. Bougher et al. Vol. 1. Venus. Tucson: Univ. of Ariz. Press, pp. 969–1014.

Meadows, V. S. and D. Crisp (1996). “Ground-based near-infrared observations of the Venus nightside: The thermal structure and water abundance near the surface”. In: *Journal of Geophysical Research* 101.E2, pp. 4595–4622.

Metropolis, N. and S. Ulam (Sept. 1949). “The Monte Carlo Method”. In: *Journal of the American Statistical Association* 44.247, pp. 335–341.

Moroz, L. V., A. Maturilli, J. Helbert, S. Sasaki, A. Bischoff, and E. K. Jessberger (2007). “Mercury Analogue Materials: Spectral Reflectance, Its Comparison with TIR Spectral Emission, and a Space Weathering Simulation Experiment”. In: *Lunar and Planetary Science Conference*. Vol. 38, p. 1741.

Moroz, L., U. Schade, and R. Wäsch (2000). “Reflectance spectra of olivine-orthopyroxene-bearing assemblages at decreased temperatures: Implications for remote sensing of asteroids”. In: *Icarus* 147.1, pp. 79–93.

Moroz, V. I. (1981). “The atmosphere of Venus”. In: *Space Science Review* 29.1, pp. 3–127.

— (2002). “Estimates of visibility of the surface of Venus from descent probes and balloons”. In: *Planetary and Space Science* 50.3, pp. 287–297.

Moroz, V. and L. Zasova (1997). “VIRA-2: A review of inputs for updating The Venus International Reference Atmosphere”. In: *Advances in Space Research* 19.8, pp. 1191–1201. DOI: 10.1016/S0273-1177(97)00270-6.

Morris, R. V., H. V. Lauer Jr, C. A. Lawson, E. K. Gibson Jr, G. A. Nace, and C. Stewart (1985). “Spectral and other physicochemical properties of submicron powders of hematite (α-Fe_2O_3), maghemite (γ-Fe_2O_3), magnetite (Fe_3O_4), goethite (α-FeOOH), and lepidocrocite (γ-FeOOH)”. In: *Journal of Geophysical Research* 90.B4, pp. 3126–3144.

Mueller, N., J. Helbert, G. L. Hashimoto, C. C. C. Tsang, et al. (2008). “Venus surface thermal emission at 1 μm in VIRTIS imaging observations: Evidence for variation of crust and mantle differentiation conditions”. In: *Journal of Geophysical Research* 113.E5, E00B17.

Nikolaeva, O. V., M. A. Ivanov, and V. K. Borozdin (1992). “Evidence on the crustal dichotomy(of Venus)”. In: *Venus geology, geochemistry, and geophysics- Research* *results from the USSR(A 92-39726 16-91). Tucson, AZ, University of Arizona Press, 1992,* pp. 129–139.

Noll, R. B. and M. B. McElroy (1972). *Models of Venus atmosphere (1972): Prepared for NASA under the cognizance of the NASA Goddard Space Flight Center*. Vol. 8011. National Aeronautics and Space Administration.

Pavri, B., J. W. Head III, K. B. Klose, and L. Wilson (1992). "Steep-sided domes on Venus: Characteristics, geologic setting, and eruption conditions from Magellan data". In: *Journal of Geophysical Research* 97.E8, pp. 13445–13478.

Pettengill, G. H., B. A. Campbell, D. B. Campbell, and R. A. Simpson (1997). "Surface scattering and dielectric properties". In: *Venus II: Geology, Geophysics, Atmosphere, and Solar Wind Environment*. Ed. by S. W. Bougher et al. Vol. 1. Venus. Tucson: Univ. of Ariz. Press, pp. 527–546.

Pettengill, G. H., P. G. Ford, and R. J. Wilt (1992). "Venus surface radiothermal emission as observed by Magellan". In: *Journal of Geophysical Research: Planets* 97.E8, pp. 13091–13102. DOI: 10.1029/92JE01356.

Pieters, C. M., J. W. Head, S. Pratt, W. Patterson, et al. (1986). "The color of the surface of Venus". In: *Science* 234.4782, pp. 1379–1383.

Price, M. and J. Suppe (1994). "Young volcanism and rifting on Venus". In: *Nature* 372, pp. 756–759.

Robinson, C. A. and J. A. Wood (1993). "Recent volcanic activity on Venus: Evidence from radiothermal emissivity measurements". In: *Icarus* 102.1, pp. 26–39.

Roush, T. L. and R. B. Singer (1986). "Gaussian analysis of temperature effects on the reflectance spectra of mafic minerals in the 1-μm region". In: *Journal of Geophysical Research* 91.B10, pp. 10301–10308.

Sagan, C. (1962–1963). "Structure of the lower atmosphere of Venus". In: *Icarus* 1.1–6, pp. 151–169. DOI: 10.1016/0019-1035(62)90015-5.

Saunders, R. S., G. H. Pettengill, R. E. Arvidson, W. L. Sjogren, W. T. K. Johnson, and L. Pieri (1990). "The Magellan Venus radar mapping mission". In: *Journal of Geophysical Research* 95.B6, pp. 8339–8355.

Schaber, G. G. (1982). "Venus: Limited extension and volcanism along zones of lithospheric weakness". In: *Geophysical Research Letters* 9.5, pp. 499–502.

Schofield, J. T. and F. W. Taylor (1983). "The solar and thermal radiation balance of the middle atmosphere". In: *VIRA workshop of the International Union of Geophysics and Geodesy, Hamburg*. Vol. 192.

Schubert, G., C. Covey, A. D. Genio, L. S. Elson, et al. (1980). "Structure and circulation of the Venus atmosphere". In: *Journal of Geophysical Research* 85.A13, pp. 8007–8025.

Schultz, P. H. (1992). "Atmospheric effects on ejecta emplacement". In: *Journal of Geophysical Research* 97.E7, pp. 11623–11662. DOI: 10.1029/92JE00613.

Seiff, A. (1983a). "Models of the Lower and Middle Atmosphere of Venus, from the Surface to 100 Kilometers". In: *Report for the Venus International Reference Atmosphere Workshop, Hamburg*.

— (1983b). "Thermal structure of the atmosphere of Venus". In: *Venus*. Ed. by D. M. Hunten et al. Vol. 1. Tucson: Univ. of Arizona Press, pp. 215–279.

Seiff, A., J. T. Schofield, A. J. Kliore, F. W. Taylor, et al. (1985). "Models of the structure of the atmosphere of Venus from the surface to 100 kilometers altitude". In: *Advances in Space*

Research 5.11. Ed. by G. K. A.J. Kilore V.I. Moroz, pp. 3–58. DOI: 10.1016/0273-1177(85)90197-8.

Selivanov, A. S., Y. M. Gektin, M. K. Naraeva, A. S. Panfilov, and A. B. Fokin (1983). "On dynamical phenomena recorded on Venus surface panoramas transmitted by Venera 13, 14." In: *Kosmicheskie Issledovaniia* 21, pp. 200–204.

Shepard, M. K., R. E. Arvidson, R. A. Brackett, and B. Fegley Jr (1994). "A ferroelectric model for the low emissivity highlands on Venus". In: *Geophysical Research Letters* 21.6, pp. 469–472.

Singer, R. B. and T. L. Roush (1985). "Effects of temperature on remotely sensed mineral absorption features". In: *Journal of Geophysical Research* 90.B14, pp. 12434–12444.

Smrekar, S. E., E. R. Stofan, N. Mueller, A. Treiman, et al. (2010). "Recent hotspot volcanism on Venus from VIRTIS emissivity data". In: *Science* 328.5978, pp. 605–608.

Solomon, S. C., S. E. Smrekar, D. L. Bindschadler, R. E. Grimm, et al. (1992). "Venus Tectonics: An Overview of Magellan Observations". In: *Journal of Geophysical Research* 97.E8, pp. 13199–13255.

Stamnes, K., S. C. Tsay, K. Jayaweera, and W. Wiscombe (1988). "Numerically stable algorithm for discrete-ordinate-method radiative transfer in multiple scattering and emitting layered media". In: *Applied Optics* 27.12, pp. 2502–2509.

Starukhina, L. V. and M. A. Kreslavsky (2002). "Radiophysical Properties of Venusian Highlands: Possible Role of Magnetic Effects". In: *Lunar and Planetary Science Conference*. Vol. 33, p. 1559.

Surkov, Y. A. (1997). *Exploration of Terrestrial Planets from Spacecraft: Instrumentation, Investigation, Interpretation*. 2nd revised. Hoboken, N. J.: John Wiley & Sons Inc., p. 446.

Svedhem, H., D. V. Titov, D. McCoy, J.-P. Lebreton, et al. (2007). "Venus Express — The first European mission to Venus". In: *Planetary and Space Science* 55.12. The Planet Venus and the Venus Express Mission, Part 2, pp. 1636–1652. DOI: 10.1016/j.pss.2007.01.013.

Tanaka, K. L., D. A. Senske, M. Price, and R. L. Kirk (1997). "Physiography, geomorphic/geologic mapping and stratigraphy of Venus". In: *Venus II: Geology, Geophysics, Atmosphere, and Solar Wind Environment*. Ed. by S. W. Bougher et al. Vol. 1. Venus. Tucson: Univ. of Ariz. Press, pp. 667–694.

Taylor, F. W. (2006). "Venus before Venus Express". In: *Planetary and Space Science* 54.13, pp. 1249–1262.

Taylor, F. W., D. Crisp, and B. Be'zard (1997a). In: *Venus II: Geology, Geophysics, Atmosphere, and Solar Wind Environment*. Ed. by S. W. Bougher et al. Vol. 1. Venus. Tucson: Univ. of Ariz. Press. Chap. Tectonic overview and synthesis, pp. 797–844.

— (1997b). "Near-infrared sounding of the lower atmosphere of Venus". In: *Venus II: Geology, Geophysics, Atmosphere, and Solar Wind Environment*. Ed. by S. W. Bougher et al. Vol. 1. Venus. Tucson: Univ. of Ariz. Press, pp. 325–351.

Taylor, H. A. and P. A. Cloutier (1986). "Venus: Dead or Alive?" In: *Science* 234.4780, pp. 1087–1093. DOI: 10.1126/science.234.4780.1087. eprint: http://www.sciencemag.org/content/234/4780/1087.full.pdf.

Titov, D. V., W. J. Markiewicz, N. I. Ignatiev, L. Song, et al. (2012). "Morphology of the cloud tops as observed by the Venus Express Monitoring Camera". In: *Icarus* 217.2, pp. 682–701. DOI: 10.1016/j.icarus.2011.06.020.

Tomasko, M. G., L. R. Doose, and P. H. Smith (1985). "The absorption of solar energy and the heating rate in the atmosphere of Venus". In: *Advances in Space Research* 5.9, pp. 71–79.

Tomasko, M. G., L. R. Doose, P. H. Smith, and A. P. Odell (1980). “Measurements of the Flux of Sunlight in the Atmosphere of Venus”. In: *Journal of Geophysical Research* 85.A13, pp. 8167–8186. DOI: 10.1029/JA085iA13p08167.

van de Hulst, H. C. (1981). *Light Scattering by Small Particles*. Dover Pubn Inc.

Vervack, R. J. and H. J. Melosh (1992). “Wind interaction with falling ejecta: Origin of the parabolic features on Venus”. In: *Geophysical Research Letters* 19.6, pp. 525–528.

Veverka, J. (1971). “A polarimetric search for a Venus halo during the 1969 inferior conjunction”. In: *Icarus* 14.2, pp. 282–283.

VMC calibration report (Aug. 4, 2008). Tech. rep. Version 1/2. VMC-MPAE-RP-SS011-001. MPS.

Welch, B. L. (Jan. 1947). “The Generalization of ‘Student’s’ Problem when Several Different Population Variances are Involved”. In: *Biometrika* 34.1/2, pp. 28–35.

Wood, J. A. (1997). “Rock weathering on the surface of Venus”. In: *Venus II: Geology, Geophysics, Atmosphere, and Solar Wind Environment*. Ed. by S. W. Bougher et al. Vol. 1. Venus. Tucson: Univ. of Ariz. Press, pp. 637–664.

Zhang, T. L., W. Baumjohann, M. Delva, H. U. Auster, et al. (2006). “Magnetic field investigation of the Venus plasma environment: Expected new results from Venus Express”. In: *Planetary and Space Science* 54.13, pp. 1336–1343.

Zolotov, M. Y. (1996). “A model for the thermal equilibrium of the surface venusian atmosphere”. In: *Geochemistry International* 33.10, pp. 80–100.

— (2007). “Solid Planet-Atmosphere Interactions”. In: *Treatise on Geophysics*. Ed. by G. Schubert. Amsterdam: Elsevier, pp. 349–369. DOI: 10.1016/B978-044452748-6.00181-4.

Acknowledgements

I'm very thankful to my supervisor, Dmitri Titov, who proposed me such an interesting and challenging problem to work on; for his suggestions in the work during my PhD and even years before; for reading and editing the manuscript; for support that he and his wife Alena were giving to me and my family.

I'm exceptionally thankful to Alexander Basilevsky, whose participation in this work can not be overstated. He guided the work via assigning tasks and leading the geological analysis of the retrieved numbers. I grateful to him not only for notably fruitful scientific lessons, but also for his amazing personality, which is so pleasurable to interact with. I would like to acknowledge his lectures, papers, and just stories about planetary and Earth geology.

I acknowledge Wojciech J. Markiewicz for his help and support, related and not related to this work, for answering my questions and participating in discussions. Especially I want to thank for all the work with Venus Monitoring Camera observations planning.

I would like to acknowledge the IMPRS program in general, and International Max Planck Research School on Physical Processes in the Solar System and Beyond providing me this precious opportunity. I'm thankful to Dieter Schmitt, the school coordinator. I sincerely thank Petra Fahlbusch for her help in administrative work.

My PhD course was possible thanks to Jürgen Blum, and I appreciate accepting me as PhD student at Technische Universität Braunschweig, thanks for the help in organization of the defence and seminar.

Nikolai Ignatiev has shared some results of his computations of gaseous absorption in Venus atmosphere and I appreciate this.

This work would not be possible without general support from all people who perform routine support of the Venus Monitoring Camera experiment: teams at IDA in Braunschweig, DLR in Berlin. Special thanks to Miguel Almeda, who was doing sometimes very tricky job to make requested observations possible.

I would like to acknowledge Michail Kreslavsky for his help, especially at the beginning of this work, that saved me from many mistakes. I'm thankful to Sanjay Limaye for expanding my understanding of Venus nature in general. I'm thankful to my colleagues from Kharkiv, Viktor Korokhin and Yuri Velikodsky, whose experience learned by me before and during this work has been widely used.

I want to thank my family. My mother who did a lot for me and was helping me whenever I need, who planned and arranged my education when I was unable to see that far in the future. Mummy, thanks for travelling to Lindau whenever I requested, this helped me a lot to stay in touch with you, and get inspired mood for work on PhD and for life in general. I'm grateful to my wife Oksana and not only as a happy husband. Being my colleague she was a patient listener and a partner in countless discussions, and the first editor of the manuscript.

I express thanks to my friends, who helped me a lot to make my life in Germany and work

on thesis more fun, especially to Megha Bhatt — my office mate — the smile and kind nature of whom formed brilliant atmosphere in the office; to Sergiy and Tais for great help with arrangement of my family in Germany and nice time spent together. I thankful to many people I met at the institute. Thanks Elena Kronberg, Elena Petrova, Larissa, Li, Lucia, Neda, Yeon Joo, Boris, Jeff, Klaus, Nikolay for the parties and get-togethers, for the pleasant communication.

I'm also thankful to one more member of our family, cat Maximiliano Sanchez Gonzales, for his never ending aptitude to keep everybody in a good mood, and because during the time of thesis writing he didn't wake me up on sunrise, as usual, but only after 7 o'clock.

And, at last, this thesis would have not be so fun and would have not reach even this level of art without free and open source software I use and enjoy. I'm thankful to the communities behind GNU project (especially to the GCC), Linux, Boost, LaTeX, freedesktop.org, KDE, Git and Kile. Special thanks to the Qt project for the nice library.

Curriculum Vitae

Persönliche Daten

Name: Eugene Shalygin
Geburtsdatum: 19. Mai 1981
Geburtsort: Kharkiv, Ukraine
Staatsangehörigkeit: ukrainisch

Studium

2002	B.S. in Physik, Kharkiv National University, Kharkiv, Ukraine
2003	M.S. in Astronomie und Physik, Kharkiv National University, Kharkiv, Ukraine
2009 – 2012	Doktorand am Max-Planck-Institut für Sonnensystemforschung, Katlenburg-Lindau und an der Technischen Universität Braunschweig

Berufserfahrung

2003 – 2007	Wissenschaftlicher Mitarbeiter, Institute of Astronomy, Kharkiv National University, Kharkiv, Ukraine
2008 – 2009	Senior Software Developer, Envion software, Kharkiv, Ukraine